CFD SIMULATIONS OF EROSION OF A STRATIFIED LAYER BY A BUOYANT JET IN A LARGE VESSEL

A Thesis

by

FATIH SINAN SARIKURT

Submitted to the Office of Graduate and Professional Studies of
Texas A&M University
in partial fulfillment of the requirements for the degree of

MASTER OF SCIENCE

Chair of Committee,	Yassin A. Hassan
Committee Members,	William H. Marlow
	Maria King
Head of Department,	Yassin A. Hassan

May 2015

Major Subject: Nuclear Engineering

ABSTRACT

One of the most important parameters in the analysis of containment safety of the light water reactors during a loss of coolant accident (LOCA) is the prediction of the hydrogen concentration. To ensure proper design of the containment to mitigate the fire/explosive risk created by the flammable hydrogen gas, this concentration build up must be analyzed. Lumped parameter (LP) codes are the main tools used in containment thermal-hydraulic analysis. However, they are limited when it comes to scenarios which require higher fidelity analysis of local phenomena. While the use of computational fluid dynamics (CFD) allows for higher fidelity analyses, CFD requires a comprehensive validation study due to turbulence and condensation modeling.

During a LOCA accident, the leaked hydrogen from the primary circuit can form a stable stratified layer at the top of the containment building. The formation and erosion of a stratified layer is a challenging numerical problem due to the interaction mechanism of the jet flow with the stratified layer. The OECD-NEA conducted an experiment at the Paul Scherrer Institute (PSI) as a part of the third International Benchmark Study (IBE-3) to investigate the erosion of the stratified layer by a vertical air-helium jet from the bottom of the large vessel. During the experiment, CFD grade experimental data was generated that could be used for comparative studies.

In the present study, the experiment is simulated by using the STAR-CCM+ CFD code with various turbulence models including Reynolds-Averaged Navier-Stokes (RANS) models and Large Eddy Simulation (LES). The Realizable k-ε and k-ω SST showed good agreement with the experimental when predicting the erosion of the stratified layer and global mixing of the gas components. The LES model also showed good agreement for velocity and faster erosion with experimental data, while the cost of the LES simulation was much higher than RANS simulations. The current validation study contributes to the sensitivity analysis of the turbulence models for erosion behavior in the stratified layer. In addition to that, the results of this study will provide a foundation to discuss the feasibility of the CFD code usage in containment level thermal hydraulic analysis.

ACKNOWLEDGEMENTS

The author would like to acknowledge the support of author's committee: Dr. Hassan, Dr. King, and Dr. Marlow. The author would like to thank the committee chair, Yassin A. Hasan, for his continual support, patience and guidance through the research described here.

Further thanks to are extended to PSI for the valuable experimental data and Texas A&M Supercomputer Center for their computational resource support. Thanks also go to my lab colleagues for making my time at Texas A&M University a great experience and thanks to Hristo Goumnerov for his proofreading of this thesis.

TABLE OF CONTENTS

LIST OF FIGURES

Page

LIST OF TABLES

Page

CHAPTER I

INTRODUCTION

The demand of electricity is increasing exponentially due to the growth of the global population and the development of industry. According to the World Bank, 17% of the world population did not have access to electricity by the end of 2011. This is in spite of the fact that electrical power is reaching more household an increasing growth rate. The key challenge is choosing a sustainable source to generate electricity. The sustainability factor is unrealistic for the fossil fuel based power generation due to its reserve limitations and environmental impacts. Global warming is one of the significant problems of using fossil fuels due to the release of greenhouse gases. On the other hand, this renewable sources cannot meet the electricity demand. The global warming concerns with an increasing demand of electricity creates stronger need for the energy policies to create more clean and reliable sources. Nuclear energy is an option that has lower greenhouse emission than renewable sources and can also meet the electricity demand. However, the public perception for nuclear energy has become a problem after accidents which resulted in radioactive material leakage into the environment. As a result, the safety features of the nuclear power reactors have been improved based on the lessons and findings from the accidents. The Fukushima accident in Japan demonstrates that further safety improvements are needed.

The Fukushima accident was caused by an earthquake following tsunami waves. The reactors were in full operation before the earthquake and they were shutdown automatically by safety systems during the earthquake. Moreover, the auxiliary generator systems were supplying power to the cooling systems to reject the radioactive decay heat from the reactor cores. Unfortunately, the tsunami destroyed the auxiliary generator systems. The resulting loss of cooling capability initiated the chain accident cases including partial core meltdown and hydrogen explosions. The current study aims to contribute to the safety analysis for hydrogen distribution in the reactor containment building during accidents. Specifically, the study focuses on the computational analysis of hydrogen distribution in large vessel by using PANDA experimental data to validate the CFD tool.

The importance of hydrogen distribution is due to its explosive characteristic at certain concentration level. Specifically, during severe accident conditions in light water cooled nuclear reactor, explosive hydrogen gas may be formed due to an oxidation reaction of high temperature zirconium cladding and steam.

If hydrogen gas is released into the containment building, it is then possible that a build up in concentration of the gas may lead to formation of explosive hydrogen and air mixture, which could potentially lead to a hydrogen explosion. Such a scenario may cause serious collateral result in loss of reactor safety systems. At normal operating conditions, the containment building is at atmospheric pressure, while the reactor pressure is between 70 and 150 times higher depending on the reactor under consideration. As a result of this significant pressure differential, any breach in the separating interface will result in a very rapid, high-energy flow of primary coolant into the containment building. Consequently, significant amount of steam and hydrogen can spread into the containment in very short time period.

The importance of hydrogen leakage was discovered after the Three Mile Island accident in 1979, which is a loss of coolant accident (LOCA). During the LOCA accident, the pressure of the primary coolant circuit decreased suddenly, which resulted in loss of cooling capability. Although, power reactors are designed to stop the fission chain reaction. The nuclear fuel continues to generate significant amount of heat due to radioactive decay. As a result of the decay heat, the temperature of the fuel and its cladding increased. Higher temperature and lower pressure caused boiling, which produced high temperature steam. The interaction of high temperature steam with fuel cladding material produced hydrogen gas. The resulting hydrogen leaked from the pressure vessel into the containment. According to the IAEA report (Henrie and Postma, 1982), it was estimated that 45% of zirconium cladding had undergone the oxidation reaction ($Zr + 2H_2O \rightarrow ZrO_2 + 2H_2$) and generated 460 kg of hydrogen gas. This amount of hydrogen gas occupied the 7.9 vol. % of the containment building, and consequently combusted. During the accident maximum pressure was measured about 3 bar without any major damage of the containment structure. The Three Mile Island accident showed that safety systems were designed well to protect the reactor and environment against radiation leakage. The lessons from the accident helped to improve the safety characteristics of the light water reactors.

The recent accident in Fukushima-2011 proved that hydrogen mitigation is key factor for nuclear reactor safety. In this scenario, the hydrogen explosion caused deterioration of the containment building integrity, which is one of the crucial barriers to prevent radioactive material leakage to the environment. It also shows that hydrogen discharge systems have to be analyzed in more details for the sake of safety. To mitigate hydrogen concentration in the containment building, passive catalytic recombiners are placed at the predicted locations of the containment building. Recombiners use a catalyst material that helps to convert hydrogen to water by reacting with oxygen. Although recombiners mitigation systems can prevent critical concentration level for ignition. The locations of the recombiners and the post-accident conditions must be analyzed with higher fidelity. Due to the fact that there may be temporary regions, which includes flammable gas clouds at certain post-accident conditions. Since hydrogen recombiners are passive devices, the gas flow inside the devices is relatively slow. The hydrogen concentration in the containment should be investigated extensively due to the combustion risk of the hydrogen in the containment building. The validated high fidelity data will allow better prediction of the hydrogen gas distribution, and then the predicted data can be used to place the recombiners more precisely to mitigate the risk of combustion during post-accident conditions.

Over the past three decades, significant knowledge has been gained with intensive research both on a national and international level. Several experimental facilities around the world have been built to investigate the hydrogen distribution such as PANDA, MISTRA, TOSQAN, THAI, PHEBUS, HDR, BMC, HYJET, etc.(Liang et al., 2014). The result of these experiments were used as a reference for numerical code developments and validation purposes. Generally, two numerical thermal hydraulic methods are used for the analysis of hydrogen distribution in the containment vessel; the Lumped Parameter (LP) and the Computational Fluid Dynamics (CFD) code. LP codes are extensively validated, while CFD codes still need more validation.

Lumped parameter codes are widely used in the nuclear industry for design and safety purposes. They are firmly validated for design level calculations. The most significant advantage of LP codes is the simple approach for the discretization of large scale geometries. The simplicity of modeling results in significantly less computation time with correspondingly less accurate results. The main disadvantages of them are the lack of ability to predict local gas mixing, the requirement of the predefined models for stratified flow and the lack of turbulent diffusion modeling (Liang et al., 2014).

While the LP codes need predefined models for complex flows, the CFD codes solve the Navier-Stokes equations with higher resolution than lumped parameter codes. As a result of higher resolution, detailed mixing of the hydrogen - air mixture can be modeled by using multi-component approach. However the use of the CFD codes requires more control volumes to simulate complex flow behavior and it needs high computational power due to the long transient time requirement for the containment safety analysis. In addition to that, the turbulence models are empirical models. As a result, the CFD codes need further validation before they can be used with confidence for nuclear safety analysis.

Special CFD codes were developed for the containment analyses. The GOTHIC is one of the special purpose containment analysis code. It was developed by Electrical Power Research Institute (EPRI). It can be used for lumped-parameter calculations and with higher resolution multi-dimensional analysis (Andreani et al., 2010). However the meshing approach of GOTHIC results in relatively coarser mesh than general purpose CFD tools. The coarse grid may not be sufficient to analyze higher details of the flow for a containment wide analysis. According to Andreani's study, usage of the coarse mesh with GOTHIC is able to predict mixing of the gases in the containment building with good agreement except some regions of the domain. However, it is reported that the finer mesh can give better results to predict flow characteristic of the jet and its interaction with stratified layer. Therefore, the usage of the general purpose CFD tools for the containment analysis are becoming more popular due to grid generation flexibility.

In another study, the realistic containment analysis has been conducted by using FLUENT and CFX for the VVER-440/213 reactor (Heitsch et al., 2010) and the study pointed out the requirements of the further validation. While the usage of the CFD for containment safety analysis are becoming more popular, the requirements for validation are increased as well.

The most challenging computational phenomena for the containment analysis is the formation of the stable stratified layer as a result of the hydrogen gas leakage from the primary circuit ($Zr + 2H_2O \rightarrow ZrO_2 + 2H_2$). The density of hydrogen gas is lower than air. As a result of that, buoyancy force causes the motion of hydrogen gas toward the upper side of the containment building, which results in stable stratified layer as shown in Figure 1. During a LOCA accident, accumulated gas in the reactor containment building can form a stable stratified layer as shown in Figure 2.

The stratified layer due to different density of the gases may challenge computational models to treat sharp density gradient and fluctuations of the velocity. For instance, the negative buoyancy effect causes deceleration on the jet flow. As a result, the erosion process (mixing of the less dense layer) occurs slowly due to negative buoyancy. Furthermore, mixing of the gas occurs with turbulence diffusion and molecular diffusion. Turbulent diffusion is calculated by turbulent models and most of the standard turbulent models are based on the specific assumptions that are violated with interaction of the jet and stratified layer. The details of this assumptions will be discussed in Chapter V.

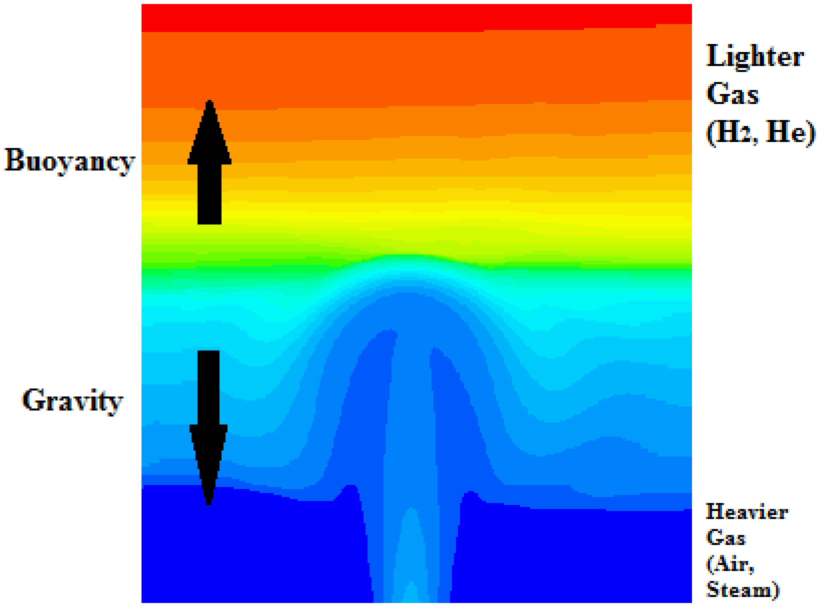

Figure 1: Buoyancy and Gravity Forces on the Stratified Layer

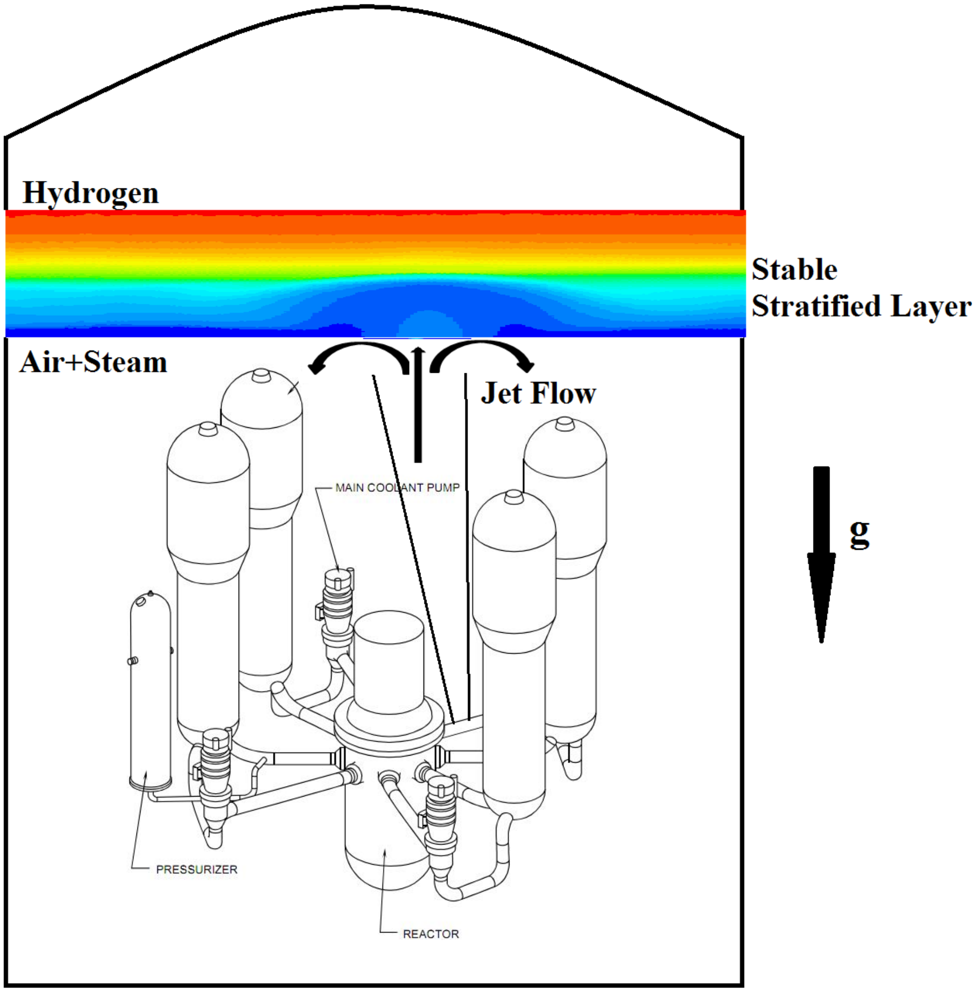

Figure 2: Stable Stratified Layer in Containment Building

In the literature, several analyses of hydrogen mixing have been conducted by using CFD codes studies including validation of the codes by using experimental data. However, mostly generic turbulent models were used for most of them with limited number of computational volume elements. The CFD benchmark study (Andreani et al., 2008) used the data of the PANDA experiment that has low momentum horizontal steam injection. The simulations turbulence models were the variations of the $k - \omega$ and $k - \epsilon$ models and number of the mesh cells ranged from 45,000 to 1.1 million. The study showed that grid sensitivity study improved the accuracy of the results significantly. Visser et al. conducted a CFD validation study (Visser et al., 2012) by using THAI (HM2) experimental data. They tried to answer the spatial and temporal discretization sensitivity for the breaking of a stable helium layer by a low momentum air injection as well as the effect of the buoyancy term in the turbulent transport equations. Their results showed overall good agreement with experimental data when the buoyancy term is included in the turbulent transport equations. The study also showed that wall function usage for near wall region does not affect the results due to the fact that mixing of the gases occurs in the core region of the fluid domain.

The erosion characteristic of the stratified layer can be related with dimensionless Froude number, which is the function of the velocity U and the diameter L of the jet in the impingement region and the characteristic pulsation of the stratification N defined as (Jirka, 2004):

$$N = \sqrt{2g \frac{(\rho_{air} - \rho_s)}{(\rho_{air} + \rho_s) H_s}}$$

$$Fr = \frac{U}{NL}$$

Froude number is the ratio of inertial to buoyancy forces. If it is less than unity, the stratified layer is dominated by buoyancy, then erosion process occurs slowly and without penetration of the injected jet flow. If it is much greater than unity, the flow is dominated by the inertial forces and the injected jet penetrated to the stratified layer.

Previous studies used a limited number of control volumes mostly with generic two equations turbulent models. In addition to that, turbulent model sensitivity analyses were not part of their study. The current study aims to address the detailed comparison of the turbulent models including Large Eddy Simulation (LES) by using STAR-CCM+ 9.04. A higher number of control volumes was used to analyze the effect of the grid resolution. The experimental data from OECD-PSI International Benchmark Exercises 3 (IBE-3)(Andreani et al., 2014) was used to compare the numerical results.

CHAPTER II

SPECIFICATIONS OF EXPERIMENT

II. 1 Geometry

OECD/NEA conducted the third International Benchmark Exercise (IBE-3) as an international effort to validate simulations of the hydrogen distribution in a containment building. IBE-3 is based on a comparison of CFD simulations with experimental results. The main purpose of the experiment is investigating the erosion of a stratified layer by an off-axis buoyant jet, which is the possible post-accident scenario as explained in Chapter I. However the helium gas was used instead of hydrogen for the safety reason.

The experiment was conducted at the PANDA facility at Paul Scherrer Institut (PSI) in Switzerland. The experimental specifications distributed to the participants via special FTP access (OECD-NEA, 2013) and it is not published online. PANDA facility has four vessels as shown in Figure 3. One of the four was used as a part of this experiment.

Figure 3: Panda Facility at PSI in Switzerland (OECD-NEA, 2013)

Certain modifications were applied to the vessel by blocking inter-vessel connections and the vessel had been isolated from other ones. The height of vessel is 8 m and 4 m outer diameter and it is made from stainless steel (DIN 1.4571). In addition to the main vessel, a 980 mm diameter manhole is located at the top of the vessel with 464 mm internal height. A vertical injection line is located 3000 mm above the lowest point in the vessel to produce low momentum air/helium jet. In order to keep constant pressure in the vessel, the air/helium mixture is vented to the atmosphere via a funnel (red component in Figure 4). The funnel is located 160 mm above lowest point. The detailed geometry can be seen in Figure 4.

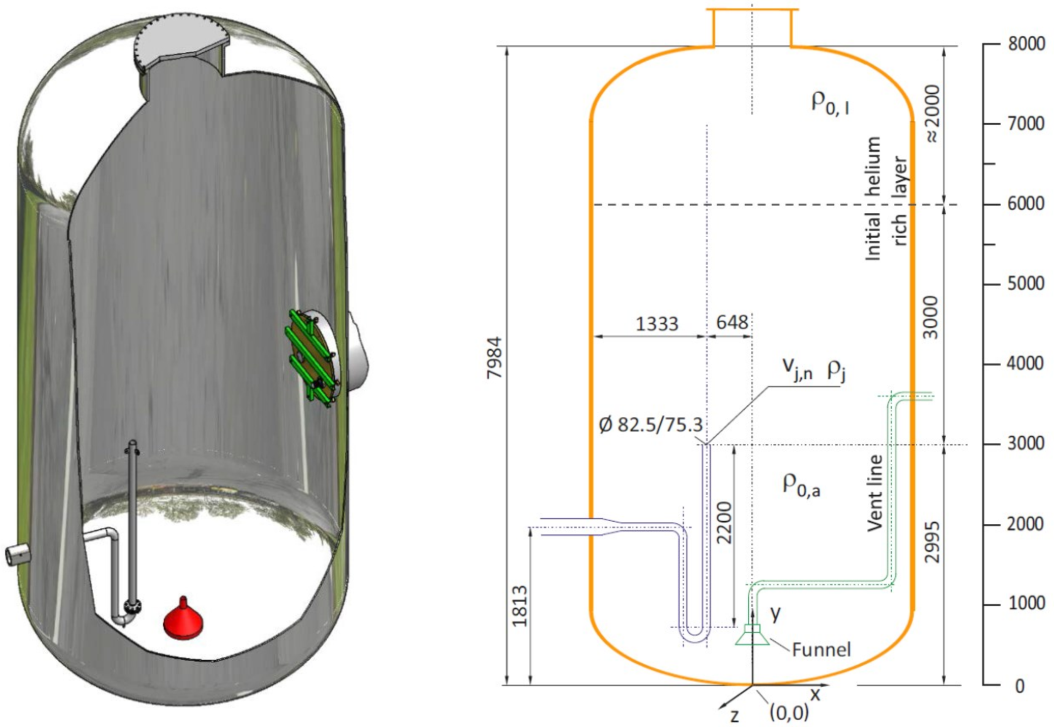

Figure 4: Vessel (left), details of vessel configuration (right) (OECD-NEA, 2013)

II. 2 Experimental Setup

The main purpose of the experiment was the analysis of erosion of the stratified layer by a vertical buoyant jet in a vessel as part of the validation study.

At the beginning of the experiment, helium was injected into the vessel to form a stable stratified layer. This process helped to create a helium-rich layer at the upper region of the vessel. The rest of the vessel is dominated by air. The stable layer means that distribution of the gases is in balance due to the balance of natural forces, which are the gravity and buoyancy forces. The stable layer formation is related with the dimensionless Richardson (Ri) number that expresses the ratio of the buoyancy term to the flow gradient term. If the Richardson number is less than unity, buoyancy can be neglected in the flow. If it is greater than unity, buoyancy is dominant in the flow with insufficient kinetic energy to mix or homogenize flow. When it is equal to the unity, the flow can be categorized as buoyancy-driven. The vertical layer formation and relationship with the Richardson number was explained in the former study of (Studer et al., 2012). When the Richardson number is greater than unity, the distribution of the gas mixture can be divided into three different category. If the inertia of the injecting gas mixture is small when the plume reaches the top of the vessel, a linear density gradient can be obtained from top to the bottom. If the inertia of the injecting gas is higher, the reversed flow at the top of the vessel forms a homogenized layer at the top with a linear density gradient below. The stratified layer in the current study has a homogenized layer at the top with a linear density gradient. Axial molar fractions of gas mixture were measured before the start of the experiment as an initial condition and it can be seen in Figure 5.

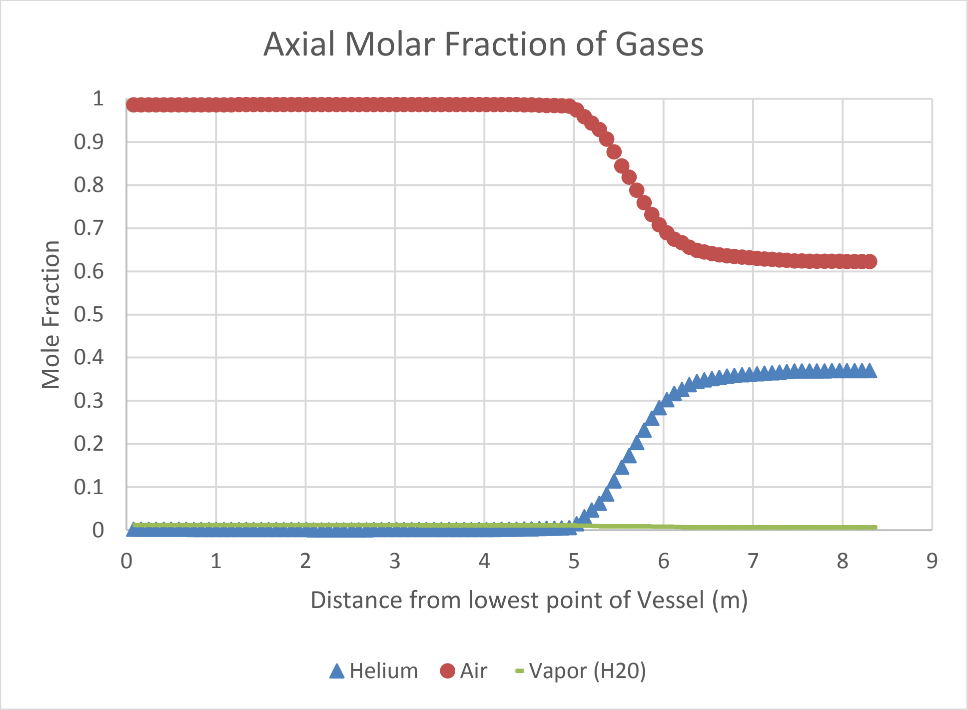

Figure 5: Molar Fraction of Gases vs. Axial elevation

The erosion of the stable stratified layer occurred by injection of the low momentum gas mixture into the vessel by using a circular pipe which has a 75.3 mm. inside diameter. The mass flow rate of helium-air mixture was measured as 21.94 g/s during the experiment and it was kept constant. On the other hand, injected gas mixture included negligible amount of the vapor due to fact that air was not dried before injection. The mole fraction of injection gas mixture was measured 36 mm above the exit of injection pipe for precise inlet condition. Helium, air and vapor mole fractions were measured as 0.134, 0.862 and 0.004, respectively. While the molar concentration is constant, the temperature of gas mixture was increased from 20 °C to 29.3 °C during transient.

II. 3 Measurements

Time dependent measurements were taken at certain points to create CFD grade experimental data. Measurements include mole concentration, temperature, vertical component of velocity, and their locations.

Two types of mass spectroscopy (MS) instruments were used to measure mole fractions of gases at different points in the vessel. The first type MS has a smaller sampling period time which is 30 seconds. The first type MS's were located at the exit of the injection pipe and at the outlet of the ventilation pipe.

The second type of MS instrument has 226 seconds as its sampling period time and this type of MS devices were placed at different points to record data during the transient period as shown in Figure 6. The estimated uncertainty of concentration measurement and location of the devices were reported as 1% and ±5.0 mm respectively.

Figure 6: Location of Mass Spectroscopy Instruments

The thermocouples were placed in the PANDA vessel at strategic points mostly in the jet plume. Two of them were reported as given in Figure 7. TC's have a 0.5 Hz frequency response. The estimated uncertainty of temperature measurements and location of the TC's were reported as ± 0.7 K and ±5.0 mm respectively.

Figure 7: Thermocouple Locations

Velocities and velocity fluctuations were measured by using PIV from three different windows. The locations of the windows are shown in Figure 8. The measurements were taken all above and around the axis of the injection pipe and they were averaged over a time period of 204.6 s.

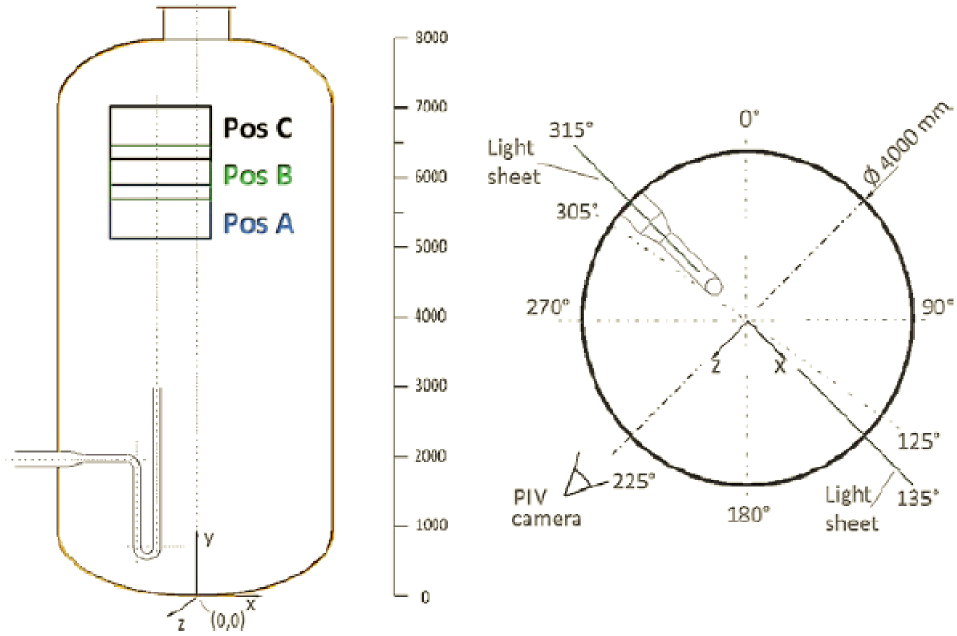

Figure 8: Position of the PIV field of views (OECD-NEA, 2013)

According to the test specification, the main interest of the benchmark study was to evaluate the capability of the codes to simulate the erosion process and mixing of the gases as well as velocity of the stratified layer under jet flow.

The erosion process is defined by drop of the helium molar concentration below a specified value which is the 20%. Ten different locations along the injection line were chosen to evaluate the erosion process as shown in Figure 9. This data can be used to evaluate the capability of the codes to simulate the interaction of the injection jet with stratified layer as well as the turbulent models capability to simulate the flow.

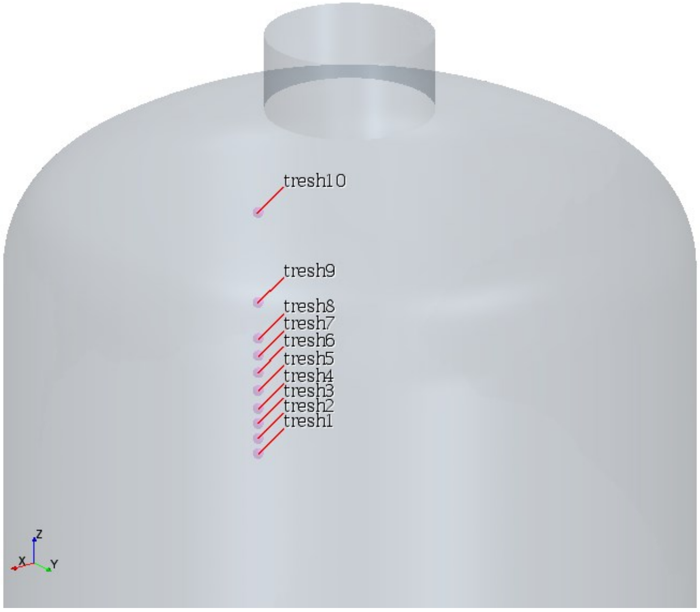

Figure 9: Concentration measurements for evaluating the stratification erosion

The velocity and turbulent kinetic energy data are averaged over a time period of 204.6 s. The solution time will refer to the time in the middle of this averaging period. Solution time for HVY-3, HVY-5, VVY-1 and TKE-2 are 1213, 1795, 111, 1213 seconds respectively. The monitor points are shown in Figure 10.

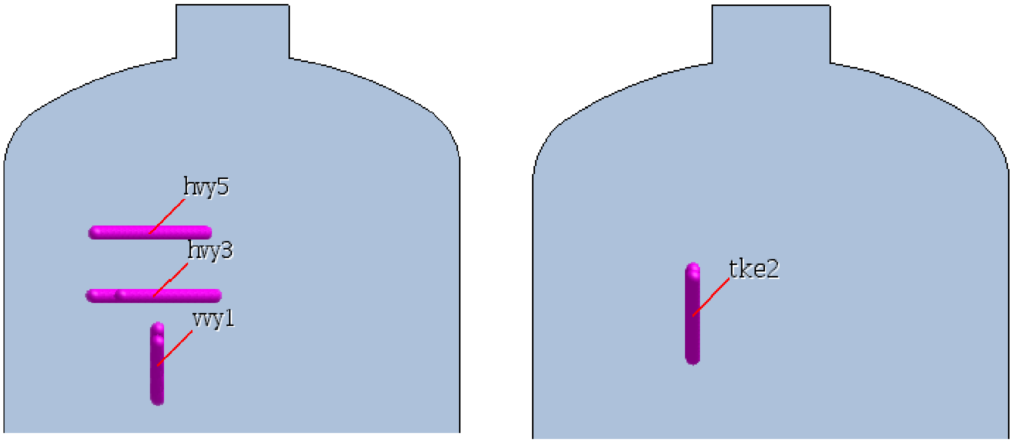

Figure 10: Positions of velocity and turbulent kinetic energy measurements

CHAPTER III

SIMULATED GEOMETRY AND MESH

III. 1 Geometry

The PANDA experimental system was built as a multi-compartment system for large-scale thermal-hydraulics experiments such as passive containment phenomena, natural circulation and condensation. It is located at the Paul Scherrer Institute (PSI), Switzerland. The design specifications of the PANDA allow for a containment wide analysis and code validation. In addition, it offers flexibility to modify the system by imposing different boundary conditions. Specifically, one compartment of the PANDA had been isolated from the others for IBE-3 study. The isolated test vessel has an inlet pipe which is used to inject the gas mixture as an inlet boundary condition. A funnel is placed at the bottom of the vessel to discharge the gas mixture and keep the pressure constant.

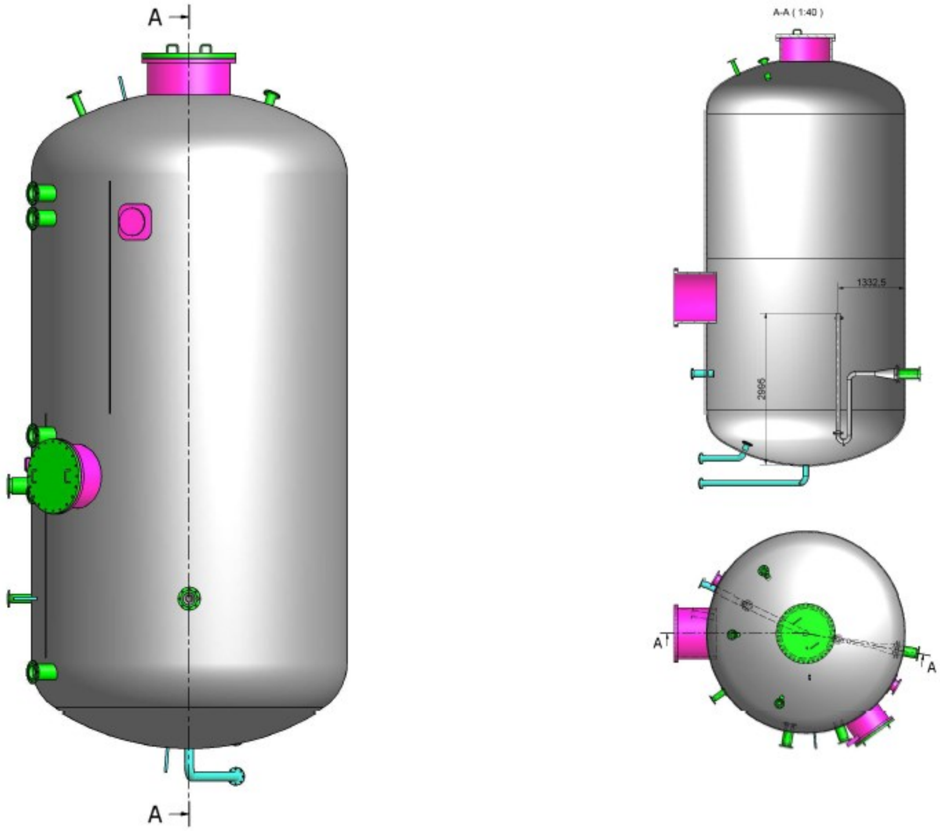

Figure 11: CAD drawing from PSI (OECD-NEA, 2013)

The geometry specifications of the PANDA vessel and its CAD drawing were supplied to all IBE-3 participants. The CAD model was build by using the *Autodesk Inventor* and distributed to each participant in ASCII format and STP file extension as shown in Figure 11. This CAD file can be read by the STAR-CCM+ meshing tool. However, the imported CAD file had several holes, which result in very low quality surface and volume mesh. The quality of the mesh is one the most important factors to prevent grid error or convergence problem. In order to remedy these problems, the CAD file was imported to SOLIDWORKS and then holes were closed and unnecessary details were removed as shown in Figure 12.

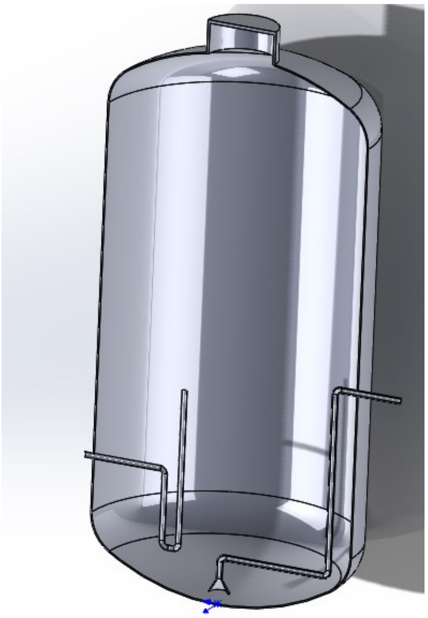

Figure 12: Modified CAD file

III. 2 Mesh

Mesh generation for complex geometry is still challenging. The quality or validity of the mesh directly affects the accuracy of the numerical results. There are two main factors to evaluate a created mesh. The validity and quality of the volume mesh should be diagnosed before starting the calculation.

Validity of the mesh can be ensured by checking unclosed cells, zero area face, and zero or negative volume cells. At the beginning of a simulation it is easy for the user to identify any problems related with validity, due to an indication from software.

However the quality of the mesh does not have same symptoms as validity. Low quality of the mesh can be initialized and it may not indicate any problem while the results are typically less accurate. As a result of that it should be diagnosed carefully by the user. Quality criteria of the mesh vary according to the CFD solver and type of the mesh.

In STAR-CCM+, the quality of the mesh is categorized based on the global and local factors. Global factors are the mesh density, mesh distribution and near wall layers. Mesh density indicates whether the resolution of the grid can capture flow features, while mesh distribution indicates any necessary refinement that the refinement for the required region such as high gradient areas. As a last factor, the near wall layer resolution depends on the flow type and effect of the wall on the flow feature. For instance, the near wall layer discretization has significant effect on the results for heat transfer, and pressure drop calculations. For current study, the near wall modeling has significant impact on the injection pipe modeling but not for the bulk region due to location of the mixing. The variation of discretization near the wall demonstrates different outlet velocity at the outlet of the jet. Different jet velocities result in a high variation in the helium-air mixing during transient. The jet outlet velocity is diagnosed for each simulation by using experimental PIV data. Overall, the global quality factors can be assessed by mesh independence study.

Local quality factors can be easily checked by using the mesh report of the STAR-CCM+. The most important factors are: skewness angle, face validity, cell quality and volume change. The skewness angle is defined as the angle between the face normal and the vector between two cell centroids as shown in Figure 13-A . The skewness angle is suggested to be kept below 85^0 by CFD experts to prevent numerical convergence issues. Face validity is the measure of the concavity of the surface mesh as shown in Figure 13-B. Cell quality is directly related with the quality of the surface mesh due to the fact that the volume mesh is constructed on the surface mesh. The quality diagnostic also can be performed by visualization of the volume mesh in particular areas. The highly skewed cells are assumed as bad cells as shown in Figure 13-C. The last criteria is the volumetric change that is the ratio of the volume of a cell to that of its largest neighbor cell as shown in Figure 13-D. In practice, the minimum value is recommended to be approximately 1e-05. For the current study, the volume changes are kept about minimum 1e-2 for all three meshes to prevent any instability in the solver.

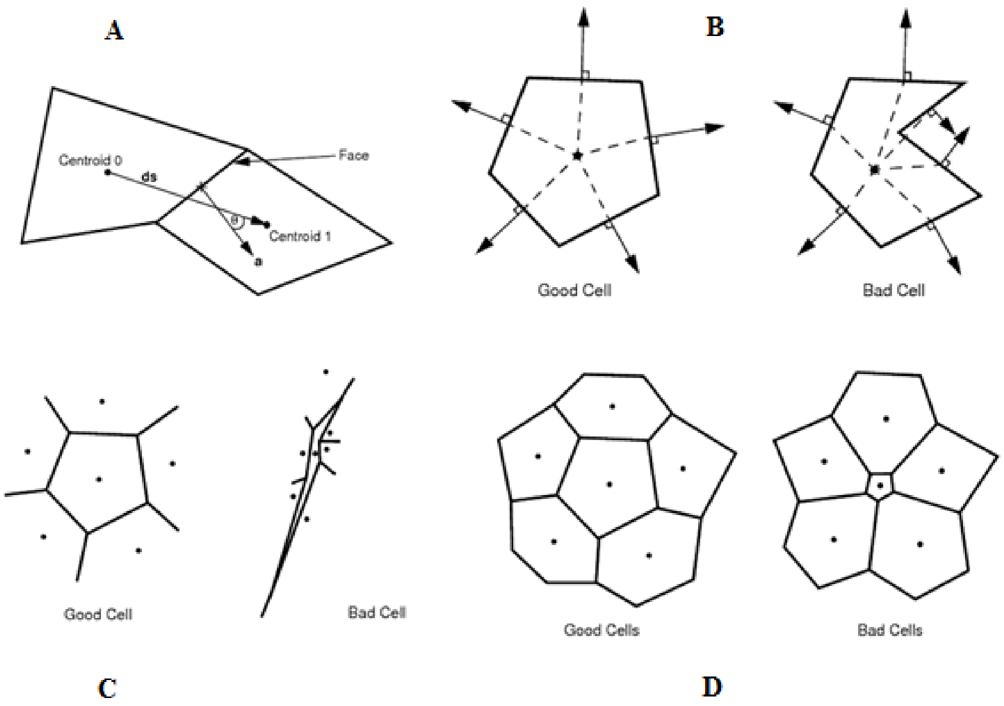

Figure 13: Cell quality metrics (STAR-CCM+, 2014)

The mesh statistics can be seen in Table I. The created coarse mesh is shown in Figure 14 and the fine mesh is shown in Figure 15.

Table I: Mesh details

	Coarse	Fine
Number of cells	4.960.166	19.052.011
Mesh type	Polyhedral	Polyhedral
Cell size	40 mm	30 mm
Mesh refinement	Injection Pipe 7.5 mm Mixing Region 24 mm	Injection Pipe 5.5 mm Mixing Region 12 mm
y^+	mostly ~ 0.1 max 30	mostly ~ 0.1 max 14
Max skewness angle	74	76

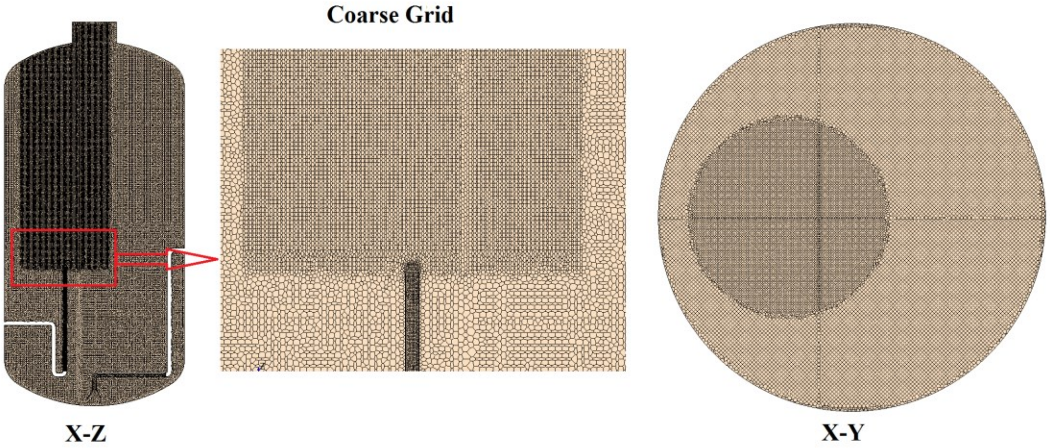

Figure 14: Coarse grid

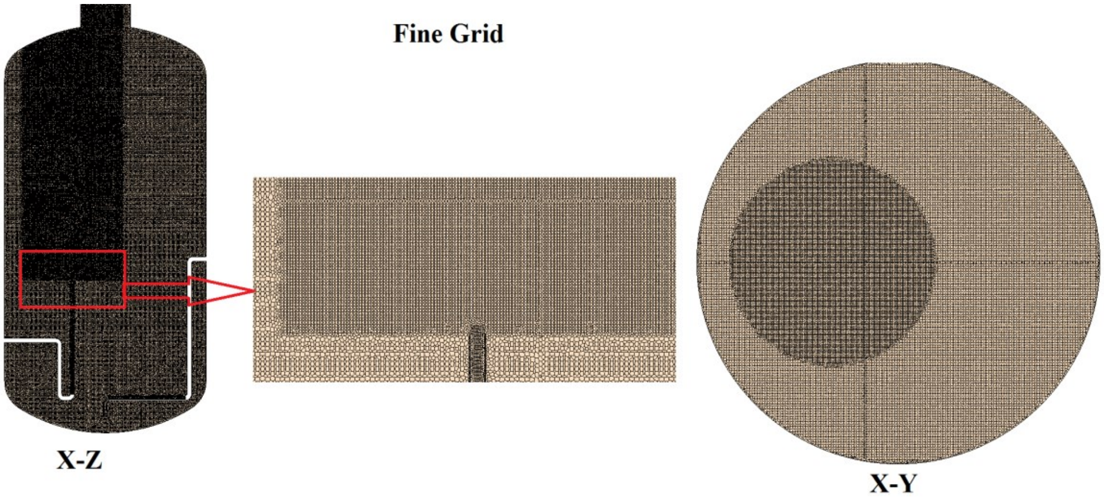

Figure 15: Fine Grid

CHAPTER IV

CFD MODELING

IV. 1 Computational Fluid Dynamics (CFD)

Computational Fluid Dynamics (CFD) is a computer based engineering tool to simulate fluid flows which are based on numerical methods and algorithms to solve and analyze problem. CFD is able to simulate a wide spectrum of current engineering problems. Moreover, applicability and feasibility of CFD is increasing by the expansion of computational power. Improvement on the computational power allows to simulate the fluid domain with more accurate representation by using more cell elements that discretize the fluid domain. In other words, one can create a higher resolution mesh that usually provides a higher level of accuracy. However, turbulent flow is still a challenging problem for most of the engineering and scientific problems due to its complex nature. Although, Direct Numerical Solution can simulate turbulent flow without any modeling requirement, it is still feasible only for fundamental scientific research applications due to excessive computational power requirement. The turbulence modeling are applied to CFD codes to compromise between computational power and accuracy. The turbulence modeling for CFD applications need comprehensive validation and verification studies. Specifically, validation and verification studies are crucial for the applicability of the CFD tools for nuclear reactor safety analysis.

IV. 2 The Mathematics of CFD

Since CFD is based upon mathematical relations, the algorithms require the solution of the mass, momentum, and energy equations. These equations were derived in the nineteenth century and are known as the Navier-Stokes equations. The Navier-Stokes equations have no known general analytical solution. However they can be discretized to be solved numerically that leads to CFD applications.

The energy equation can be neglected depending on the flow problem such as constant isothermal flows. However, in the current analysis Energy equation has to be solved due to the temperature variation at the inlet boundary condition and in the flow domain. Therefore it is necessary to solve energy equation to calculate temperature and density of the gas by using the Ideal Gas Law.

In addition to the energy equation, the species transport equation has to be solved to compute the diffusion of the gas mixture components, which are helium and air for this study. The mole fraction of the air-helium gas mixtures varies in the flow domain initially due to a stable stratified layer. Buoyancy must be accounted for in the current study due to the variable density.

IV.2.1 Conservation of Mass, Momentum and Energy

Equation 4.1 is the integral form of the continuity equation. The terms on the left-hand side are the transient term and convective term, while the right-hand side term is the mass source term. In present study source term is zero.

$$\frac{\partial}{\partial t}\int_{V} \rho \, dV + \oint_{A} \rho(\mathbf{v}) \cdot d\mathbf{a} = \int_{V} S_u \, dV \tag{4.1}$$

Equation 4.2 represents the integral form of the momentum equation. The terms on the left-hand side of Equation 4.2 are the transient term and convective flux. On the right-hand side are the pressure gradient term, viscous flux and buoyancy body force term, respectively.

$$\begin{gathered}\frac{\partial}{\partial t}\int_{V} \rho\mathbf{v} \, dV + \oint_{A} \rho\mathbf{v} \otimes (\mathbf{v}) \cdot d\mathbf{a} = \\ -\oint_{A} p\mathbf{I} \cdot d\mathbf{a} \oint_{A} \mathbf{T} \cdot d\mathbf{a} + \int_{V} (f_g) \, dV\end{gathered} \tag{4.2}$$

where buoyancy source term f_g equals to $(\rho - \rho_{ref})g$. The reference density is kept constant in the software. However due to variation of the density by the time, it is defined by a user specified function that computes the volume averaged density during transient.

The energy equation in integral form is given by Equation 4.3, where $\boldsymbol{H}$ is the total enthalpy, $\mathbf{q}''$ is the heat flux vector, $\mathbf{T}$ is the viscous stress tensor, $\mathbf{v}$ is the velocity vector, $\mathbf{f}$ is the body force vector representing the combined body forces and s_u is energy source term defined by user if desired.

$$\frac{\partial}{\partial \mathrm{t}}\int_{\mathrm{V}} \rho \boldsymbol{E}\, d\mathrm{V} + \oint_{\mathrm{A}} [\rho \boldsymbol{H}(\mathbf{v})] \cdot d\mathbf{a} =$$

$$- \oint_{\mathrm{A}} \mathbf{q}'' \cdot d\mathbf{a} \oint_{\mathrm{A}} \mathbf{T} \cdot \mathbf{v}\, d\mathbf{a} + \int_{\mathrm{V}} \mathbf{f} \cdot \mathbf{v}\, d\mathrm{V} + \int_{\mathrm{V}} \mathrm{s}_u\, d\mathrm{V} \tag{4.3}$$

Total energy, $\boldsymbol{E}$, is related to the total enthalpy $\boldsymbol{H}$ by Equation 4.4

$$\boldsymbol{E} = \boldsymbol{H} - \frac{p}{\rho} \tag{4.4}$$

Total enthalpy is defined as the summation of the enthalpy and kinetic energy of the fluid mass as given in Equation 4.5. If the fluid has zero velocity, it reduces to enthalpy. The relationship of the enthalpy with the temperature and specific heat is given by Equation 4.6.

$$\boldsymbol{H} = h + \frac{|\mathbf{v}|^2}{2} \tag{4.5}$$

$$h = C_p T \tag{4.6}$$

IV.2.2 Equation of State

In order to solve the continuity, momentum and energy equations, supplementary information is required. Therefore an equation of state model is used for calculation. The Equation of State model is used to compute the density with respect to flow parameters.

Available Equation of State models in STAR-CCM+ are Ideal Gas, Real Gas, Polynomial Density Gas, IAPWS-IF97, and Constant Density Model In the PANDA experiment, the gas mixture has temperature and pressure gradient due to variation of mole fraction distribution inside the vessel. Ideal gas law is chosen to calculate density as a function of temperature and pressure as given in Equation 4.7.

$$\rho = \frac{p_{static} + p_{ref}}{\frac{R_u}{M} T} \tag{4.7}$$

where R_u is the universal gas constant, M is the molecular weight, and T is temperature of gas.

In the experiment, buoyancy forces have a significant effect due to the mole distribution of air-helium which results in density difference. Gravity modeling is enabled in CFD calculation to account buoyancy effect. When gravity is activated the static pressure is related to working pressure, p, by equation 4.8.

$$p_{static} = p + \rho_{ref} g(x - x_0) \tag{4.8}$$

where x_0 is position vector, termed the operating altitude, ρ_{ref} is reference density and g is the gravitational vector.

The reference density is an important parameter for this analysis due to the additional uncertainty in the Equation of State due to static pressure and in the momentum equation due to buoyancy source term. On the other hand, the density difference between air and helium is relatively low. However due to variation of the density by the time, it is defined by a user specified function that computes the volume averaged density during transient.

IV.2.3 Species Transport Equation

The transport equation for the mass fraction Y_i of species i^{th} is solved as in Equation 4.9.

$$\frac{\partial}{\partial \mathrm{t}}\int_{\mathrm{V}} \rho\, Y_i\, d\mathrm{V} + \oint_{\mathrm{A}} \rho\, Y_i(\mathbf{v}) \cdot d\mathbf{a} = \oint_{\mathrm{A}} \left[\rho D_{i,m} \nabla Y_i + \frac{\mu_t}{\sigma_t} \nabla Y_i\right] \cdot d\mathbf{a} + \int_{\mathrm{V}} \mathrm{S}_{Y_i}\, d\mathrm{V} \tag{4.9}$$

where D_m is molecular diffusivity. The Turbulent Schmidt number σ_t is used as default value of 0.9 as in the buoyancy term except for sensitivity analysis of the Turbulent Schmidt Number.

The molecular diffusion coefficient was defined by using the Chapman-Enskog Equation 4,10. It defines the diffusion coefficient as a function of the molecular masses of air-helium mixture and as a function of temperature and pressure.

$$\mathrm{D}_{1,2} = \frac{1.858\mathrm{x}10^{-3} T^{3/2}}{p {\sigma^2}_{12} \Omega} \sqrt{\frac{1}{M_1} + \frac{1}{M_2}} \tag{4.10}$$

where M_1, M_2 are the molecular masses of the gas components, p is the pressure, T is the temperature, σ^2 is the average collision parameter and Ω is the temperature dependent collision integral. The diffusion coefficient for helium and air mixture is $7\text{x}10^{-5}\,\frac{m^2}{s}$ at T=298 K and p= 1 atm.

IV.3 Methodology of CFD

The general methodology of CFD is identical for all types of simulations. It has preprocessing, solving and post-processing steps.

In the preprocessing step, the geometry of the fluid system is created to define the physical bounds of fluid domain. While creating the geometry, some simplifications could be applied such as removing unnecessary details, which helps to compromise between accuracy and computation time. This step presumes a level of expertise by the user to predict the proper details/objectives. Once the geometry is completed, the next step is division of the bounded fluid domain into discrete cells (mesh or grid). The mesh may be uniform or non-uniform depending on the complexity of the geometry. Mesh generation is one of most important step of the simulation, as it directly affects the accuracy of the results and convergence performance. There are different mesh quality criteria to ensure that it is created properly. These criteria depend on the mesh type(s). General quality criteria for volume mesh are cell skewness angle, boundary skewness angle, face validity, volume change and negative volume cells due to concave cells. These criteria were discussed in detail in Chapter 3.

The boundary conditions are defined at the same step as the meshing process.

For a completely defined problem, proper boundary conditions must be identified on solution domain boundaries. Boundary conditions in CFD Have the same logic as the mathematical boundary value problem. The differential equation should be well posed. In other words, a given input to the problem should result in unique solution. Once boundary conditions are fully defined, the last step before the calculation is choosing fluid materials and appropriate models such as turbulence models, equation of state, gravity, multi or single phase, multi or single component, and etc.

The calculation step is the part in which equations are solving iteratively. In this step the most important task is monitoring convergence behavior of the problem. Residuals of continuity, momentum, energy equations and other implemented equations denote the convergence characteristic. However, the decrease of the residuals does not always mean real convergence. One can add engineering points in to the domain to observe certain flow parameters in critical locations to ensure convergence.

When convergence is an issue, modifications and quality improvements on the mesh can help convergence. In addition to that, the convergence behavior is affected by some other parameters such as under relaxation factors for segregated solver, courant number for coupled solver and time step for transient analysis. For instance, in transient analysis reducing of the time steps generally helps to ensure convergence, especially when strong transient is taking place at the initial time steps. The under-relaxation factor sustains numerical stability by decreasing part of value from previous iteration to dampen solution. Only drawback of lowering this factor is increasing number of iteration for convergence. The courant number for coupled solver is used in a similar manner as the under relaxation factor.

One other important factor for the accuracy of the results is the order of the discretization of the convection term. In CFD, the scalar values are stored at the center of the cells. However, the face values are required for the convection terms of the transport equations. The face values are calculated by interpolation of the cell center values. The interpolation is accomplished through an upwind scheme. Since, the first-order analysis resulted in unrealistic solutions due to false numerical diffusion, at least second-order discretization is desired for CFD applications. The details of the CFD model are given in Table II.

Table II: CFD modeling details

Solver	Segregated Pressure-based algorithm
Pressure correction scheme	SIMPLE
Spatial discretization	2nd order upwind (bounded central differencing scheme for LES)
Temporal discretization	2nd order implicit
Time step size	0.001-0.5 (depend on time and turbulent models)
Equation of state	Ideal Gas
Multi-Component Gas	2nd order convective
Convergence Criteria	Max 10^{-5}
Number of iterations per time step	10-20

IV.4 Boundary Conditions of PANDA Experiment

In the experiment, two boundary conditions are used. The inlet boundary condition that is used to inject air-helium gas mixture, and the outlet boundary condition that is used to discharge the gas from vessel to keep pressure is constant during full transient. In CFD modeling the inlet was modeled as mass flow inlet, outlet as pressure outlet and all other solid surfaces are modeled as walls. The location of the boundary conditions can be seen in Figure 16.

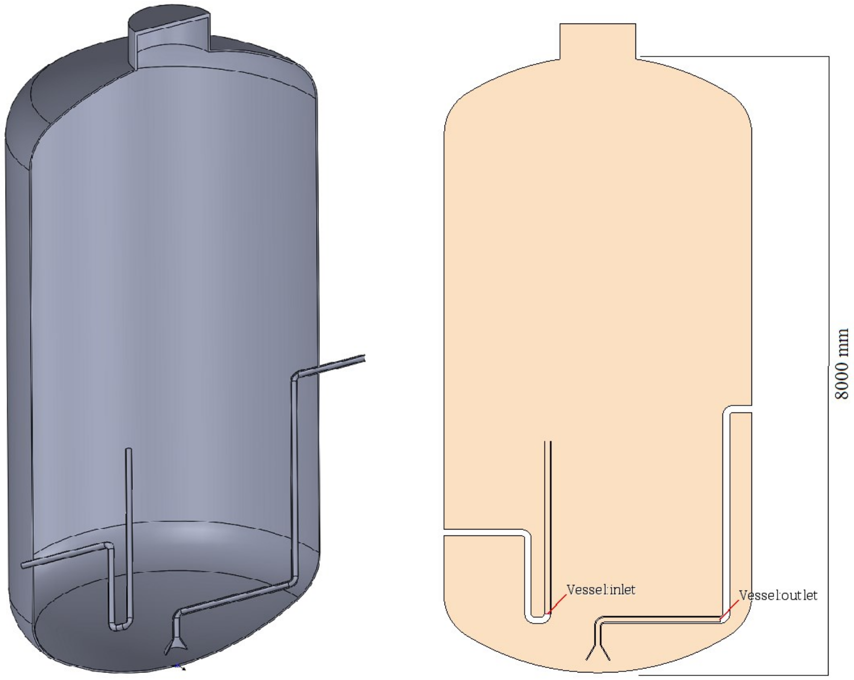

Figure 16: CAD drawing is in the left and Boundary conditions are on the right

IV.4.1 Inlet Boundary

At the inlet, mass flow inlet boundary condition is used. Because the mass flow is controlled in the experiment and the density is changing by due to temperature difference in the time. The velocity at the boundary cells is calculated by using Equation 4.11.

$$\mathrm{v} = \frac{m}{\rho . \mathrm{a}} \tag{4.11}$$

where v is velocity, m is mass flow rate, ρ is density and a is unit surface area.

The total mass flow rate was measured and reported as constant 21.94 g/s. The mass flow rate of air was 21.52 g/s and helium was 0.42 g/s. The injected air also included humidity. The water vapor mass flow rate was not measured. However, mass spectroscopy measurement at the outlet of the injection pipe was performed and it led to the deduction that a very small amount of vapor content was injected to the vessel. The mole fractions of air, helium and water vapor were 0.862, 0.134 and 0.004, respectively. In addition to the inlet mass flow rate data, experimental PIV measurements at the outlet of the injection pipe was used to set appropriate boundary condition at the inlet. Details of inlet boundary conditions are given in Table III.

Table III: Inlet Boundary Conditions

Air Mass Flow Rate	21.52 g/s
Helium Mass Flow Rate	0.42 g/s
Air Mole Fraction	0.862
Helium Mole Fraction	0.134
Water Vapor Mole Fraction	0.004
Injection Gas Temperature	20℃ to 29.3℃
Pressure	0.994 bar
Inlet Pipe Diameter (inner)	75.3 mm
Turbulence Intensity	7.4%
Turbulent Length Scale	75.3 mm

The temperature of gas mixture changes by the time as shown in Figure 17. It is imported to the STARCCM+ by using the field function option. Since, the density and velocity of the jet flow are related with the temperature, the variation of the temperature was considered in the boundary condition for higher fidelity.

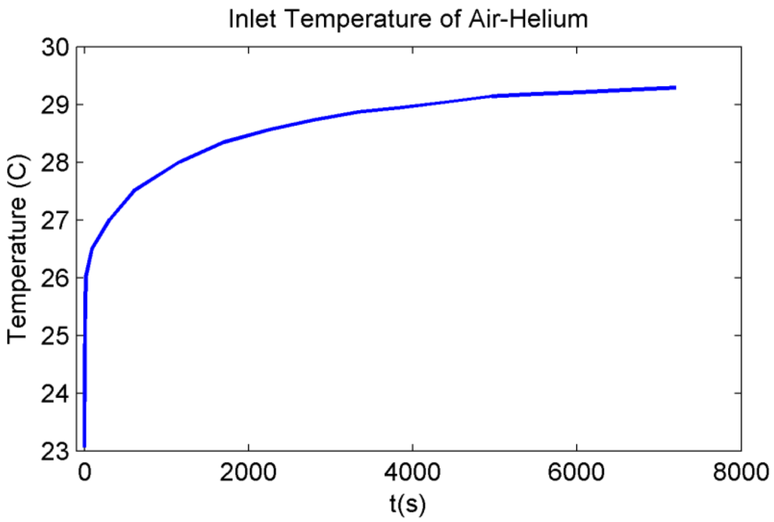

Figure 17: Temperature of the gas mixture

IV.4.2 Outlet Boundary

The effect of the outlet boundary condition on the overall flow behavior is negligible due to the location of the outlet boundary condition. It is confirmed during preliminary simulations by checking erosion process. In the experiment, the outlet boundary condition was used to keep constant pressure in the vessel.

In CFD, the pressure outlet boundary condition extrapolates the boundary face velocity from the neighbor interior node. Essentially, the temperature and the mole fractions of the gas components are computed as a result of the simulation. However the software needs these input for reversed flow condition. In case of the reverse flow, these values are used. Otherwise the values at the outlet are not affecting the flow.

IV.4.3 Wall Boundary

At the wall of vessel, injection pipe and discharge pipe, the wall boundary condition was applied. In other words, the no-slip boundary condition was specified. The velocity of the fluid at the wall boundary was specified as zero.

IV.5 Initial Conditions

Gas mixture of air-helium was produced before starting the experiment. The temperature and mole fraction of the gases were measured at the beginning of the experiment. Then they applied to the CFD model to match with experimental conditions. The velocity of the gas mixture was set to zero and turbulent kinetic energy was set to very close to zero as initial condition. The mole fraction measurement from experiment is given in Figure 18.

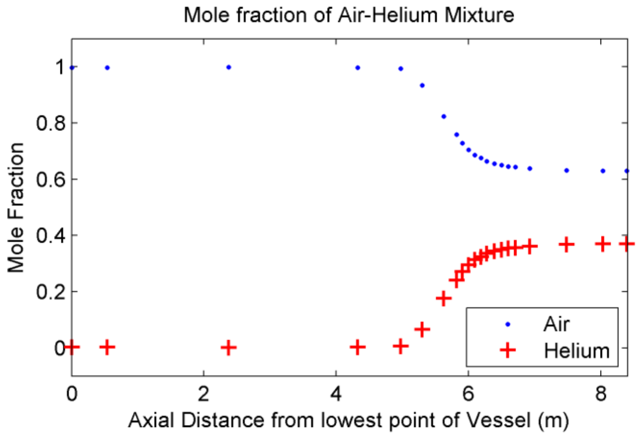

Figure 18: Initial mole fraction distribution

The imported mole fraction distribution is validated by visualization of the scalar mole fraction distribution and by using line-monitors. The scalar of the mole fractions can be seen in Figure 19.

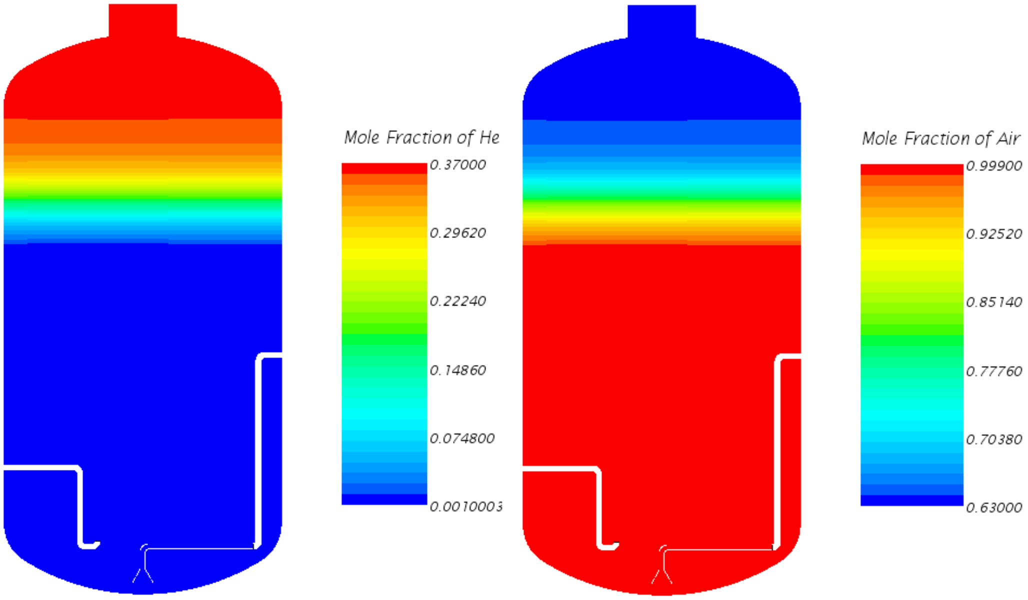

Figure 19: Scalar of the mole fraction distribution

The gas mixture temperature varies along the axial direction of the vessel as well. Measurement of temperature is given on the right side of Figure 20 and visualization of the scalar from CFD software can be seen on the left. The density of the gas mixture at the beginning of the simulation was computed based on the experimental inputs. High gradient of the density can be seen in Figure 21.

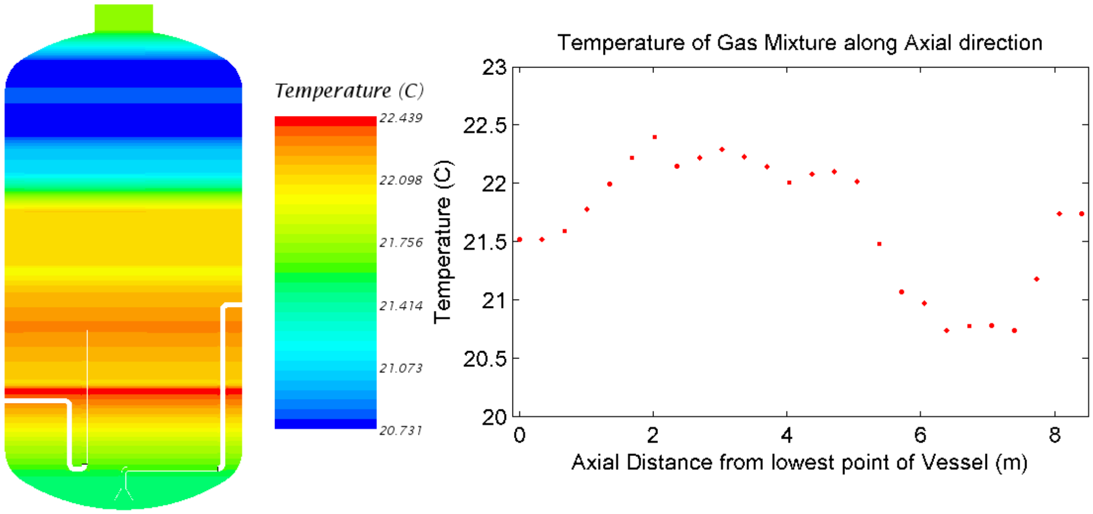

Figure 20: Initial temperature of the gas

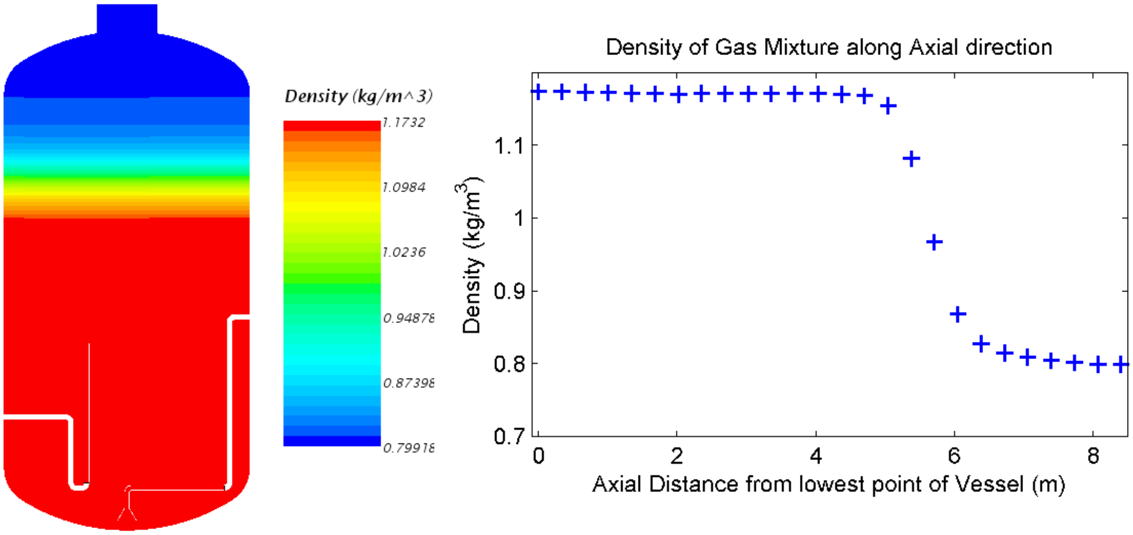

Figure 21 : Density of gas mixture

CHAPTER V

TURBULENCE MODELING

V.1 Turbulence

In general, the fluid flow has two major characteristic regimes that are laminar and turbulent. The characteristic of the flow regime can be identified by the dimensionless Reynolds number that is defined as the ratio of the inertial forces to the viscous forces. For laminar flow the general behavior of the flow is smooth and it has smooth streamlines. In laminar region, viscous forces dominate the inertial forces. Once inertial forces dominates over the viscous forces, the flow has more chaotic characteristic and streamlines. This regime is known as turbulence. In the turbulent flow, diffusion and mixing of the flow is much higher than laminar flow. Obviously this property enhances the mixing and heat transfer. Turbulent is a desirable regime for the most of the engineering applications. On the other hand, the chaotic behavior causes difficulty for identifying and predicting the flow characteristics. Due to its complex nature, turbulent is still a challenging problem for both computational and experimental studies.

Turbulent flow contains eddies of different length scales. Most of the kinetic energy is produced by large-scales. Decay of the energy cascades from larger to the smaller scales is caused by an inertial and viscous effects. This process creates smaller structures until eddies become small enough that molecular diffusion dominates the flow. Energy of the smaller eddies are released via viscous dissipation in the Kolmogorov length scale.

Turbulent length scales can be categorized as below;

- Integral length scales.
- Kolmogorov length scales.
- Taylor microscales.

Integral length scales is largest scales in the energy spectrum. Eddies in this scale contain most of the energy in the flow and it also has highest fluctuation of velocity and lowest frequency. Length scales of eddies are limited by the dimension of the flow geometry. This criteria helps to define the length scale as turbulent boundary condition for RANS models. Due to fact that eddies cannot be greater than the flow dimension.

Kolmogorov length scales is the smallest scales in the spectrum. This scale has higher frequency characteristic and it is locally isotropic. In addition to these properties, the viscos forces are dominant and turbulent kinetic energy is dissipated as heat energy. The locally isotropic behavior of this scale is an advantage to model this scale instead of resolve. Kolmogorov microscales are defined (Landahl and Mollo-Christensen, 1992) as:

Kolmogorov Length Scale:

$$\eta = \left(\frac{\nu^3}{\epsilon}\right)^{1/4} \tag{5.1}$$

Kolmogorov Time Scale:

$$\tau_\eta = \left(\frac{\nu}{\epsilon}\right)^{1/2} \tag{5.2}$$

Kolmogorov Velocity Scale:

$$u_\eta = (\nu\epsilon)^{1/4} \tag{5.3}$$

where ϵ is the average rate of dissipation of turbulence kinetic energy per unit mass, and ν is the kinematic viscosity.

The Taylor microscales are the intermediate length scale that fluid viscosity has significant impact on the eddy structures. The inertial forces dominates the flow for larger scales than Taylor microscales, while the viscous forces are dominant for smaller scales. (Landahl and Mollo-Christensen, 1992).

V.2 Turbulence and CFD

CFD applications have commonly been used for turbulent flow in last three decades. Although there are numerous available turbulent models including hybrid variations, the general purpose turbulence model has not been developed yet. Each model has its own specific advantages or disadvantages according to the flow structures.

Although, the turbulent flow can be resolved directly by solving the Navier-Stokes equations, which is called Direct Numerical Simulation, it is not feasible for current engineering problems due to its extensive computational cost. As a compromise between accuracy and computational cost, turbulent models have been developed.

There are three main methods to solve turbulent flow. Direct Numerical Simulation (DNS), Large Eddy Simulation (LES) and Reynolds-Averaged Navier-Stokes (RANS). In addition to these major classes, there is also a mixed approach such as using Detached Eddy Simulation (DES). It is a hybrid method of RANS and LES models and One-Equation turbulent models.

DNS has still a very limited applications area and it is mainly used for research purposes. The DNS method is solving the Navier-Stokes equations directly with very fine grid and time-steps to capture smallest scales of the turbulent flow. As a result of this requirement, the cell size must be at least same size as the smallest length scale of turbulence.

RANS turbulent models are the methods of the modeling of turbulence instead of solving it directly. In the RANS model, the Navier-Stokes equations for the instantaneous pressure and velocity are decomposed into a mean value. The terms of resulting equation are identical to original equations except the Reynolds Stress Tensor (RST), which appears in the momentum transport equation. For this term, there are two major approaches to model: turbulent viscosity models and Reynolds-stress models. They are explained in details in following part of this chapter.

RANS models have the advantage of the lower computational cost, while they have a disadvantage due to the isotropic Boussinesq approach to model the RST. Two equation turbulence models are developed on this assumption. In addition to that, the grid sensitivity of the RANS models are less significant than other models. Since the grid size and turbulent scales are not related with each other due to fact that all scales are modeled and solved with the transport equations instead of resolving them directly.

In the LES turbulence model, the larger eddies are resolved directly, while the smaller eddies are modeled. In fact, the smaller turbulent scales are mostly isotropic, and this helps to reduce the cost of modeling in the sub-grid scales. The characteristic of the larger scales is dependent on the flow geometry while the characteristic of the smaller scales is more global due to the isotropic features of the smaller scales. This feature helps to compromise between accuracy and computational power due to the natural characteristic of the Kolmogorov scale, the computational cost to resolve this scale is significantly higher than other scales. LES can be categorized between RANS models and DNS models. In the computational grid level, it resolves the flow like DNS solver and below the grid size level, it works like RANS solver by using sub-grid scale modeling.

V.3 Reynolds Averaging

In order to model the turbulence instead of solving it directly, Reynolds-Averaged Navier-Stokes are used. It is suggested by Osborne Reynolds that the variables in the Navier-Stokes equations could be decomposed into time averaged and turbulent-fluctuation terms.

$$U(x,t) = \overline{U}(x) + u'(x,t) \tag{5.4}$$

where the average velocity $\overline{U}$ is defined as

$$\overline{U} = \frac{1}{2T} \int_{-T}^{T} U \, dt \tag{5.5}$$

The time average of the fluctuating velocity u' is

$$\overline{u'} = \frac{1}{2T} \int_{-T}^{T} u' \, dt = \frac{1}{2T} \int_{-T}^{T} (U - \overline{U}) dt = 0 \tag{5.6}$$

The resulting averaged equations are identical to the original equations except an additional term now appears in the momentum transport equation. The additional term is known as the Reynolds stress, and can be defined as tensor:

$$\mathbf{T}_t \equiv -\rho\overline{\mathrm{v}'\mathrm{v}'} = -\rho \begin{bmatrix} \overline{u'u'} & \overline{u'v'} & \overline{u'w'} \\ \overline{u'v'} & \overline{v'v'} & \overline{v'w'} \\ \overline{u'w'} & \overline{v'w'} & \overline{w'w'} \end{bmatrix} \tag{5.7}$$

There are two main approaches to provide closure for Reynolds stress in STAR-CCM+ 9.04 (STAR-CCM+, 2014). Eddy viscosity models and Reynolds stress transport models. Eddy viscosity models are widely used for various flow applications. Spalart-Allmaras, $k - \epsilon$ and $k - \omega$ are available in STAR-CCM+ 9.04 as well as their variations.

V.4 Eddy Viscosity Models

Eddy viscosity models are based on the concept of a turbulent viscosity hypothesis to model the Reynold stresses, as obtained from Reynolds averaging of the Navier-Stokes equations. Reynold stresses is modeled by a linear constitutive relationship with the mean flow field,

$$\mathbf{T}_{\boldsymbol{t}} = -\rho\overline{\mathrm{v}'\mathrm{v}'} = 2\,\mu_t\,\mathbf{S} - \frac{2}{3}(\mu_t\boldsymbol{\nabla}.\mathbf{v} + \rho k)\mathbf{I} \tag{5.8}$$

where μ_t is the turbulent viscosity (or eddy viscosity) k is the turbulent kinetic energy, and **S** is the strain tensor :

$$\mathbf{S} = \frac{1}{2}(\boldsymbol{\nabla}\mathbf{v} + \boldsymbol{\nabla}\mathbf{v}^{\boldsymbol{T}}) \tag{5.9}$$

The linear relationship for Reynold stress is known as the Boussinesq hypothesis. Turbulent viscosity is calculated by the transport equation(s). These models are categorized according to the number of transport equations solved.

V.4.1 One-Equation Turbulence Model

The Spalart-Allmaras is one of the most common used one-equation turbulence models and it solves a single transport equation for the turbulent viscosity term, while earlier one-equation models solved the transport equation for the turbulent kinetic energy.

The Spalart-Allmaras model was developed for aero-space applications. The developer of the model presented reasonable results for mild separation (flow past a plane wing), mixing layer and radial jet flows. However, Wilcox (Wilcox, 1998) concluded that it is not suitable for flows involving complex recirculation, and body forces such as buoyancy. Wilcox concluded that two-equation models are more suited to flows involving body forces. It was not used as part of the turbulent model sensitivity analysis. The current study has strong buoyancy effect as well as recirculation around jet layer and at the top of the vessel.

V.4.2 Two-Equations Turbulence Models

Two equation turbulence models are most widely used for most types of engineering problems. $k-\varepsilon$ and $k-\omega$ are widely used as industry standard models. Two-equation models include two transport equations to compute turbulent flow behavior. In general, turbulent kinetic energy, k, is one of the transport variables and secondary transport variables vary according to the model. The most common second transport variables are the turbulent dissipation, ε, and the specific dissipation rate, ω. The second variable is used to determine the scale of the turbulence (spatial or temporal). The turbulence models and their variations have specific advantages and disadvantages depending on the flow types.

V.4.2.1 K-Epsilon Model

The K-Epsilon ($k - \epsilon$) turbulence model is one of the most widely used and modified two-equation turbulence model in which the turbulent kinetic energy is, $k,$ and its dissipation rate is, ε. Significant amount of research has been dedicated to improve the model for several decades. As a result of several attempts to improve the model, various forms of the $k - \epsilon$ are developed.

The original $k - \epsilon$ model was developed to use wall functions instead of resolving the viscous sublayer. However, later modifications allow to resolve the viscous sublayer by using Low-Reynolds and Two-layer models.

There are two main approaches to resolve viscous sublayer with the $k - \epsilon$ model, the low-Reynolds and two-layer approach. Low-Reynolds models are obtained by applying damping functions to the coefficients of the turbulence viscosity and dissipation rate as a function of the wall distance.

Two-layer approach is proposed by (Rodi, 1991). According to the approach, flow domain is divided into two layers as the layer next to the wall boundary (solid boundary) and the layer far from the wall boundary. In the wall boundary, the turbulent dissipation rate and turbulent viscosity are computed as a function of distance from the wall. While, the dissipation rate far from wall is blended with the dissipation rate that are computed by ε transport equation, the turbulent kinetic energy equation is solved for the entire flow domain without using any blending function. The current version of CFD tool has three different versions of the two-layer formulation, two for shear-driven-flows and one for buoyancy-driven flows. The main difference between the models are the near wall treatment. It is used in the Two-Layer Realizable $k - \epsilon$ analysis.

$$\begin{aligned}
&\frac{\mathrm{d}}{\mathrm{dt}}\int_{\mathrm{V}} \rho k \, d\mathrm{V} + \oint_{\mathrm{A}} \rho k\left(\mathbf{v} - \mathbf{v}_{\mathrm{g}}\right) \cdot d\mathbf{a} \\
&\qquad = \int_{\mathrm{V}} \left(\mu + \frac{\mu_t}{\sigma_k}\right) \nabla \mathrm{k} \,.\, d\boldsymbol{a} \\
&\qquad + \int_{\mathrm{V}} [f_c G_k + G_b - \rho((\varepsilon - \varepsilon_0) + \Upsilon_M) \ + \mathrm{S}_k] \, d\mathrm{V}
\end{aligned} \tag{5.10}$$

$$\begin{aligned}
&\frac{\mathrm{d}}{\mathrm{dt}}\int_{\mathrm{V}} \rho\epsilon \, d\mathrm{V} + \oint_{\mathrm{A}} \rho\epsilon\left(\mathbf{v} - \mathbf{v}_{\mathrm{g}}\right) \cdot d\mathbf{a} \\
&\qquad = \int_{\mathrm{V}} \left(\mu + \frac{\mu_t}{\sigma_\epsilon}\right) \nabla \epsilon \,.\, d\boldsymbol{a} \\
&\qquad + \int_{\mathrm{V}} [f_c C_{\epsilon 1} \mathrm{S}\epsilon + \frac{\epsilon}{k}(C_{\epsilon 1} \ C_{\epsilon 3} G_b) - \frac{\epsilon}{k + \sqrt{\mathrm{v}\epsilon}} C_{\epsilon 2} \rho(\varepsilon - \varepsilon_0) \\
&\qquad + \mathrm{S}_\epsilon] \, d\mathrm{V}
\end{aligned} \tag{5.11}$$

where: S_k and S_ϵ are the user-specified source terms. ϵ_0 is ambient turbulent value in the source terms that counteracts turbulence decay. f_c is the curvature correction factor. G_k is turbulence production term and G_b is the buoyancy term. Since stratification of the gas layer causes buoyancy effect on the jet flow. The buoyancy term is important term for the current study.

$$G_k = \mu_t S^2 - \frac{2}{3}\rho k \nabla.\mathbf{v} - \frac{2}{3}\mu_t(\nabla.\mathbf{v})^2 \tag{5.12}$$

The buoyancy term for ideal gas approximation is given:

$$G_b = -\frac{\mu_t}{\rho\sigma_t}\frac{\partial\rho}{\partial T}(\nabla T.\boldsymbol{g}) \tag{5.13}$$

where S is the modulus of the mean strain rate tensor:

$$\mathrm{S} \ = \ |\mathbf{S}| = \sqrt{2\mathbf{S}:\mathbf{S}} \tag{5.14}$$

where **S** is given below:

$$\mathbf{S} = \frac{1}{2}(\boldsymbol{\nabla}\mathbf{v} + \nabla\mathbf{v}^{\boldsymbol{T}}) \tag{5.15}$$

The turbulent viscosity is given as:

$$\mu_t = \rho C_\mu \frac{k^2}{\epsilon} \tag{5.16}$$

where C_μ is computed as:

$$C_\mu = \frac{1}{A_0 + A_s U^{(*)}\frac{k}{\epsilon}} \tag{5.17}$$

where $U^{(*)}$ is given below as a function of the strain rate tensor, **S**, and the rotation rate tensor, **W**.

$$U^{(*)} = \sqrt{\mathbf{S}:\mathbf{S} - \mathbf{W}:\mathbf{W}} \quad (5.18)$$

$$\mathbf{W} = \frac{1}{2}(\nabla\mathbf{v} - \nabla\mathbf{v}^{T}) \quad (5.19)$$

Table IV: Model Coefficients of Realizable $k - \epsilon$ Turbulence Model

$\boldsymbol{A_0}$	$\boldsymbol{A_s}$	$\boldsymbol{\Phi}$	$\boldsymbol{W}$
4.0	$\sqrt{6}\cos\phi$	$\frac{1}{3}\mathrm{acos}(\sqrt{6}W)$	$W = \frac{S_{ij}S_{jk}S_{ki}}{\sqrt{S_{ij}S_{ij}}^{3}}$
$\boldsymbol{C_{\epsilon 1}}$	$\boldsymbol{C_{\epsilon 2}}$	$\boldsymbol{\sigma_k}$	$\boldsymbol{\sigma_\epsilon}$
Max(0.43,$\frac{\eta}{5+\eta}$)	1.9	1.0	1.2

The model coefficients of the Realizable $k - \epsilon$ Turbulence Model are given in Table IV.

V.4.2.2 K-Omega SST Model

The K-Omega $(k - \omega)$ turbulence model is developed by D.C. Wilcox as an alternative to the $k - \epsilon$ model. Two transport equations are solved for the turbulent kinetic energy, k and for specific dissipation rate, ω, that is the dissipation rate per unit turbulence kinetic energy (ε/k). One reported advantage of the $k - \omega$ model over the $k - \epsilon$ is higher accuracy when there are adverse pressure gradients applied to the boundary layers (Wilcox, 1998). However the model has a significant drawback for internal flows because of the excessive sensitivity of ω in free stream that results in severe sensitivity at the inlet boundary condition specifically for internal flows.

The disadvantage of the $k-\omega$ model was examined by (Menter, 1994). The ε transport equation of standard $k-\epsilon$ model is converted to ω transport equation. The transformed equation includes an extra term that is non-conservative cross-diffusion. This transformation may give similar results to the $k-\epsilon$ model. However, the SST-model has a blending function that includes the cross diffusion term far from wall. As a result of this blending, the $k-\omega$ SST model switches to $k-\epsilon$ model at the core region of the flow and to $k-\omega$ model at the near wall region.

$$\begin{aligned}\frac{\mathrm{d}}{\mathrm{dt}}\int_{\mathrm{V}} \rho k\, d\mathrm{V} + \oint_{\mathrm{A}} \rho k\left(\mathbf{v}-\mathbf{v}_{\mathrm{g}}\right)\cdot d\mathbf{a} \\ = \int_{\mathrm{V}} (\mu+\sigma_k\mu_t)\nabla \mathrm{k}\,.\,d\boldsymbol{a} \\ + \int_{\mathrm{V}} [G_k - \gamma'\rho\beta^* f_{\beta^*}((\omega k - \omega_0 k_0)) \ + \mathrm{S}_k]\, d\mathrm{V}\end{aligned} \tag{5.20}$$

$$\begin{aligned}\frac{\mathrm{d}}{\mathrm{dt}}\int_{\mathrm{V}} \rho\omega\, d\mathrm{V} + \oint_{\mathrm{A}} \rho\omega\left(\mathbf{v}-\mathbf{v}_{\mathrm{g}}\right)\cdot d\mathbf{a} \\ = \int_{\mathrm{V}} (\mu+\sigma_\omega\mu_t)\nabla\omega\,.\,d\boldsymbol{a} \\ + \int_{\mathrm{V}} (G_\omega - \rho\beta f_\beta(\omega^2 - \omega_0^2) + D_\omega + \mathrm{S}_\omega)\, d\mathrm{V}\end{aligned} \tag{5.21}$$

where S_k and S_ω are the user-specified source terms. As it can be seen in transport equations for $k - \omega$ SST model, the buoyancy term is not implemented in STAR-CCM+ 9.04. The buoyancy term is implemented into the turbulence kinetic energy equation by using user-specified source term option as given below.

$$G_b = -\frac{\mu_t}{\rho\sigma_t}\frac{\partial\rho}{\partial z}\boldsymbol{g} \tag{5.22}$$

where turbulence production of ω is evaluated as:

$$G_\omega = \rho\gamma\left[\left(S^2 - \frac{2}{3}(\nabla.\mathbf{v})^2\right) - \frac{2}{3}\omega\nabla.\ \mathbf{v}\right] \tag{5.23}$$

where γ is a blended coefficient of the model and *S* is the modulus of the mean strain rate tensor. The model coefficients of the SST model are given in Table V.

Table V: Model Coefficients of $\boldsymbol{k - \omega}$ SST Turbulence Model

$\boldsymbol{\kappa}$	$\boldsymbol{\beta^*}$	$\boldsymbol{\beta_1}$	$\boldsymbol{\sigma_{k1}}$
0.41	0.09	0.075	0.85
$\boldsymbol{\sigma_{\omega 1}}$	$\boldsymbol{\beta_2}$	$\boldsymbol{\sigma_{k2}}$	$\boldsymbol{\sigma_{\omega 2}}$
0.5	0.0828	1.0	0.856

V.5 Reynolds-Stress Model

The Boussinesq eddy viscosity approach to model the Reynolds Stress tensor is extensively used for turbulence modeling. For instance, it is used for two equation models as explained in part 5.2. The approach is able to give accurate results, when the turbulence structure of the meant flow is isotropic due to the Boussinesq hypothesis. The erosion of the stratified layer by a buoyancy layer has a non-isotropic characteristic. It is violating the eddy viscosity approach for isotropic Reynolds Stress Tensor (RST). On the other hand, the Reynolds Stress model (Launder et al., 1975) is solving all components of the RST. This model accounts for the anisotropy due to sudden changes in the strain rate and secondary flows in ducts. However, non-isotropic stress tensors are considered only in the momentum equations. The turbulent mass flux term in the species equation is treated still as isotropic. The RSM model requires to solve seven equations in three dimensions that require higher computational time and memory than two-equation models. Six of the nine components of the RST must be solved due to symmetry. In addition to the six component of the RST, the turbulence dissipation term is treated as isotropic just as in the Standard $k - \epsilon$. The specific Reynolds stress tensor $\mathbf{R} = \overline{\mathbf{v'}_{\iota}\mathbf{v_{J}}'}$ is computed by the transport equation as given:

$$\frac{\mathrm{d}}{\mathrm{dt}}\int_{\mathrm{V}} \rho\mathbf{R}\, d\mathrm{V} + \oint_{\mathrm{A}} \rho\mathbf{R}\left(\mathbf{v} - \mathbf{v}_{\mathrm{g}}\right) \cdot d\mathbf{a}$$

$$= \int_{\mathrm{V}} \mathbf{D}\,.\,d\boldsymbol{a} + \int_{\mathrm{V}} \left[\mathrm{P} + \mathrm{G} - \frac{2}{3}\boldsymbol{\rho}\mathbf{I}\,(\epsilon + \gamma_{M}) + \Phi \quad \mathbf{S}_{\mathbf{R}}\right] d\mathrm{V} \tag{5.23}$$

where the terms are the diffusion, turbulent production, buoyancy production, turbulent dissipation, dilatation dissipation, pressure strain and user-specified source.

Reynolds Stress Diffusion: $\mathbf{D} = \left(\mu + \frac{\mu_t}{\sigma_k}\right) \nabla\mathbf{R}$

Turbulent production: $\mathbf{P} = -\rho(\mathbf{R}\,.\,\nabla\, \mathbf{v}^{\boldsymbol{T}} + \nabla.\,\mathbf{R}^{\boldsymbol{T}})$

Buoyancy Production (for varying density case): $\mathbf{G} = \frac{\mu_t}{\rho\sigma_t}(\mathbf{g} \otimes \nabla\rho + \nabla\,\rho \otimes \mathbf{g})$

Dilatation Dissipation Rate: $\gamma_M = C_M\, k\, \epsilon/c^2$ c is the speed of sound, $C_M = 2$

The pressure strain term modeling is the greatest problem for the RSM. There are three different approach in the CFD tools. Linear Pressure Strain, Linear Pressure Strain Two Layer, and Quadratic Pressure Strain. The Linear Pressure Strain Two Layer formulation was used for fair comparison as a part of the turbulence model sensitivity study due to blending wall layer approach. The model coefficients for Linear Pressure-Strain Two Layer are given in Table VI.

Table VI: Model Coefficients of RSM

$\boldsymbol{C_1}$	$\boldsymbol{C_2}$	$\boldsymbol{C_{1w}}$	$\boldsymbol{C_{2w}}$
1+2.58 $a\, a_2^{1/4}(1\text{-}exp[(-0.0067Re_t)^2]$	$0.75\sqrt{a}$	$-\frac{2}{3}C_1 + 1.67$	$max(\frac{4C_2 - 1}{6C_2}, 0)$
Re_t	$\boldsymbol{a}$	$\boldsymbol{a_2}$	$\boldsymbol{a_3}$
$\frac{k^2}{\epsilon \text{v}}$	$1 - \frac{9}{8}(a_2 - a_3)$	**A:A (A** is anisotropy tensor)	$A_{ik}A_{kj}A_{ji}$

V.6 Large Eddy Simulation

Large Eddy Simulation (LES) is a technique for direct simulation of the large eddies. It is based on Kolmogorov’s theory. According to the theory, large eddies are dependent on the dimension of the flow domain while the smaller scales of the turbulence are less dependent on the dimension of the flow domain. As a result, the smaller scale can be modeled while larger scales are solved directly. This assumption allows to compromise between accuracy and computational cost. The resolved enegy spectrum of the eddies is shown in Figure 22.

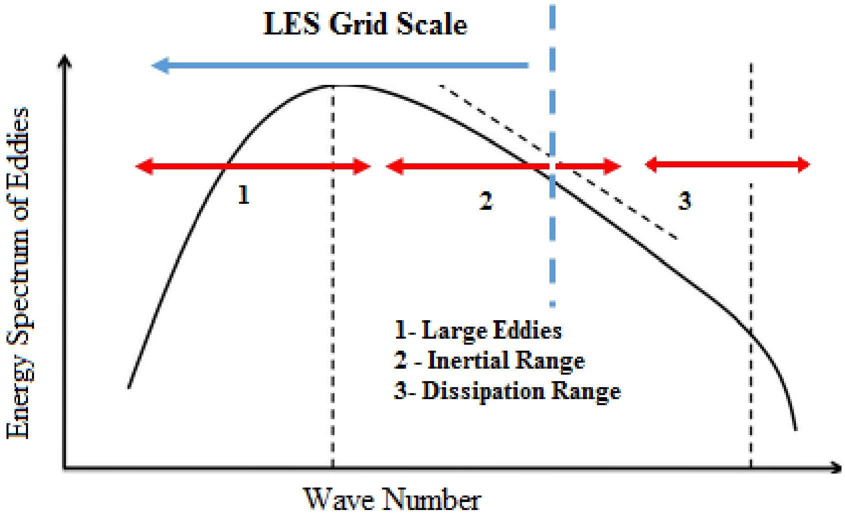

Figure 22: Energy spectrum of Eddies

Mathematically, the LES model uses a filter for the Navier-Stokes equations that separates scales smaller than grid size and larger than grid size. The larger scales are solved directly while the smaller scales are modeled with subgrid-scale (SGS) models. The general filtering operation is introduced by Leonard

$$\bar{\boldsymbol{U}}(x,t) = \int G(r,x)\, \boldsymbol{U}(x-r,t) d\boldsymbol{r} \tag{5.23}$$

where G is a kernel filter function that satisfy the normalization condition. If it is integrated over the entire flow domain, the result of integration is equal to unity .The velocity field has the decomposition and the variables represents the grid-scale and subgrid-scale part as:

$$\boldsymbol{U}(x,t) = \overline{\boldsymbol{U}}(x,t) + \boldsymbol{u}'(x,t) \tag{5.24}$$

Substitution of the decomposed velocity (and pressure) into the continuity and Navier-Stokes equations and applying a filter give the equations of motion for the resolved field.

Continuity Equation:

$$\frac{\partial\, \overline{U_\iota}}{\partial x_i} = 0 \tag{5.25}$$

Momentum Equations:

$$\frac{\partial \overline{U}_j}{\partial t} + \frac{\partial\, \overline{U_\iota U_J}}{\partial x_i} = \nu \frac{\partial^2\, \overline{U}_j}{\partial x_i \partial x_i} - \frac{1}{\rho}\frac{\partial \bar{p}}{\partial x_i} + \frac{1}{\rho}\frac{\partial \tau_{ij}}{\partial x_i} \tag{5.26}$$

τ_{ij} is modeled with Wall-Adapting Local-Eddy Viscosity (WALE) Subgrid Scale model (Nicoud and Ducros, 1999). The model has advantage of lower sensitivity to the model coefficient while the Smagorinsky SGS model is more sensitive. This advantage is reported in the user manual (STAR-CCM+, 2014). WALE is selected based on this fact to prevent bias for turbulence model sensitivity analysis.

CHAPTER VI

RESULTS

The post-process analysis has been done by processing of more than 80.000 CSV formatted files by writing a MATLAB code. As a long time transient analysis, the excessive storage is required. However storage of all simulation file with 1 second interval requires 7200 simulation files for all simulations requiring about 400 Terabytes hard-drive space, which is enormous for even research level studies. In addition to that, writing of the simulation file to the hard-drive causes significant delay. As a solution, the monitor points are created to extract only chosen parameter at the defined points as CSV formatted output files. The selected monitor points for present study can be seen in Chapter II of this thesis.

VI.1 $\mathbf{k-\omega}$ SST Results

In this part of Chapter VI, the results of the simulation by using the $k - \omega$ SST turbulent model will be discussed including a grid sensitivity analysis.

VI.1.1 Mole Fraction Results

First step is the comparison of the helium concentrations from both numerical and experimental studies at different locations and at different time steps. Since, the current study focus on the erosion of the stratified layer, the concentration of the gas mixture along the jet axis must be investigated during transient. Figures 23-32 show the time dependent mole fraction of the helium in the stratified layer to evaluate the $k-\omega$ SST turbulent model and the effect of the grid resolution to evaluate the stratification.

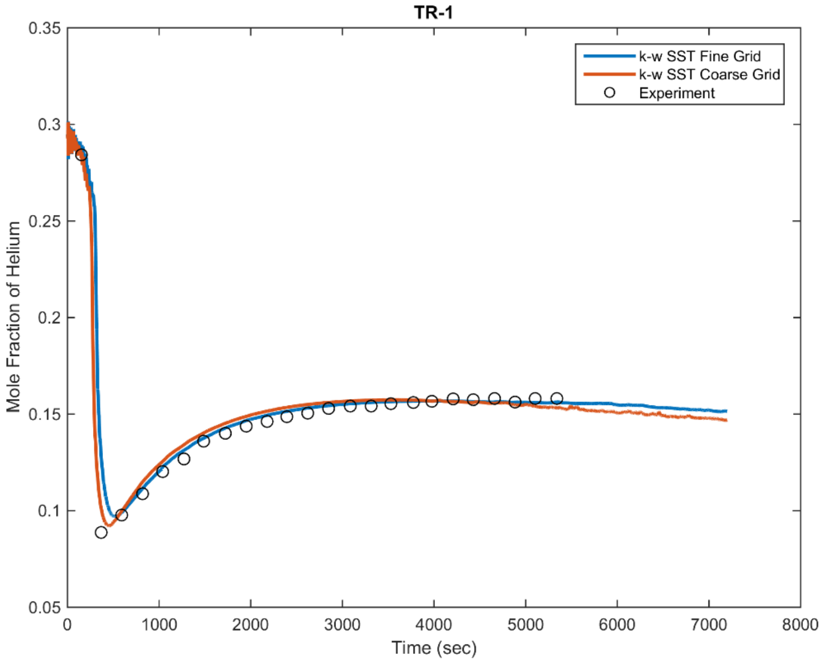

Figure 23: Mole fraction of helium vs. time (s) for mesh sensitivity at point TR-1

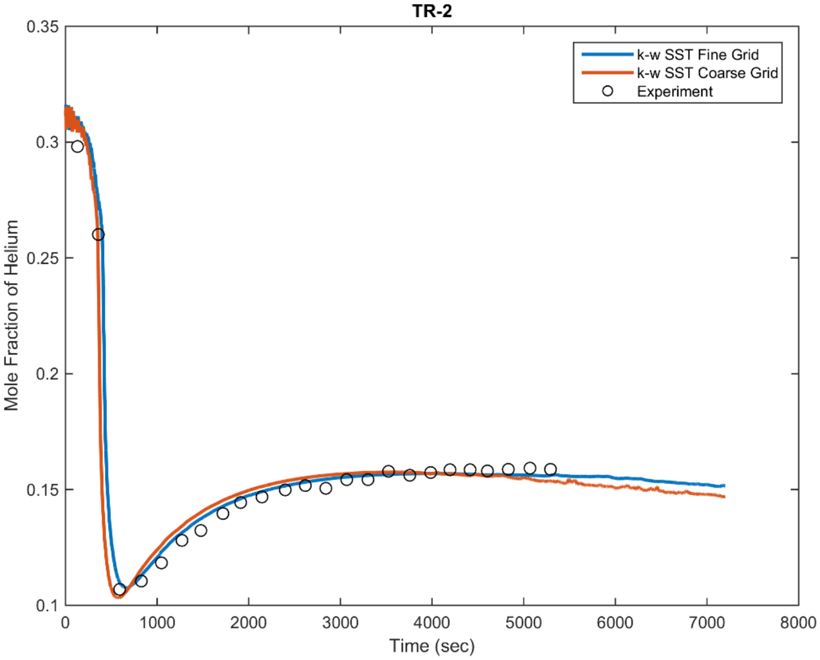

Figure 24: Mole fraction of helium vs. time (s) for mesh sensitivity at point TR-2

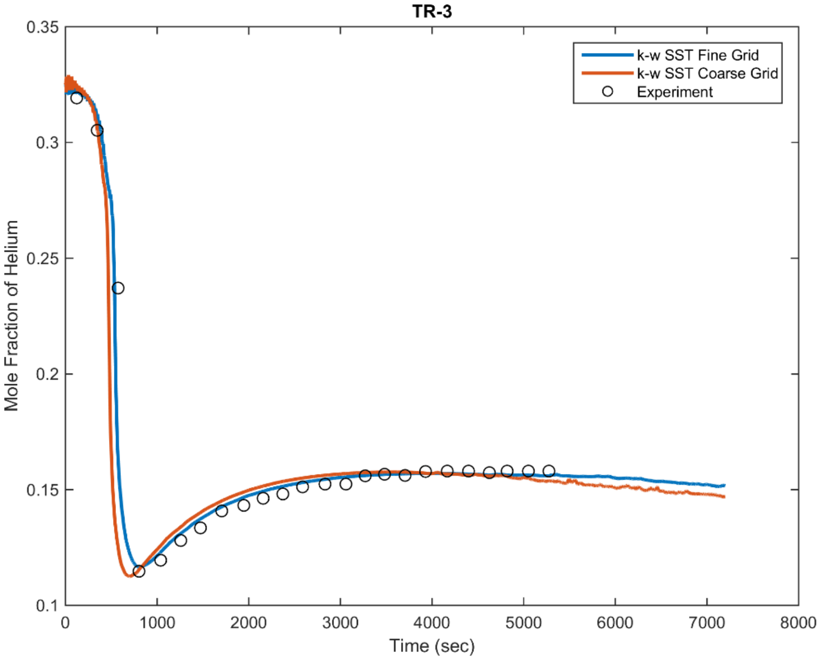

Figure 25: Mole fraction of helium vs. time (s) for mesh sensitivity at point TR-3

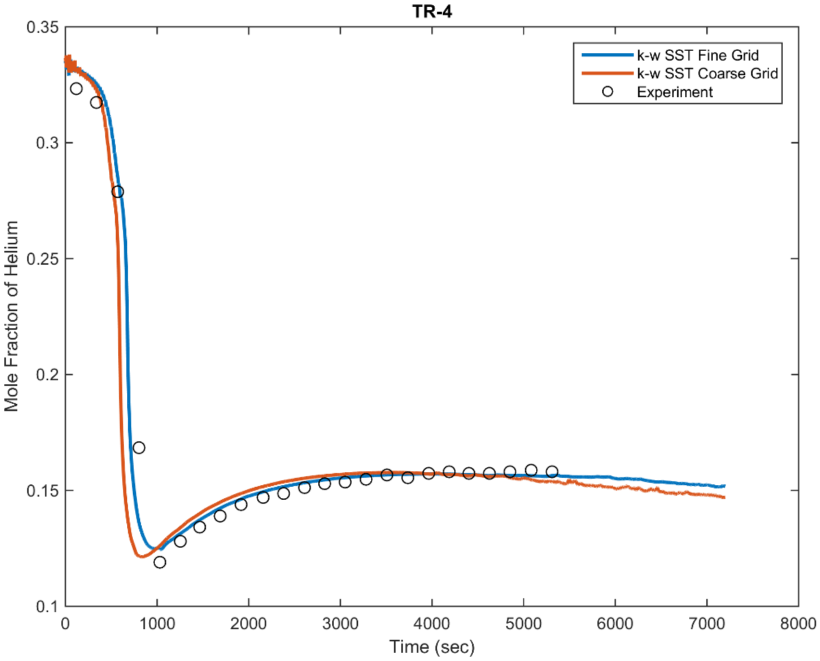

Figure 26: Mole fraction of helium vs. time (s) for mesh sensitivity at point TR-4

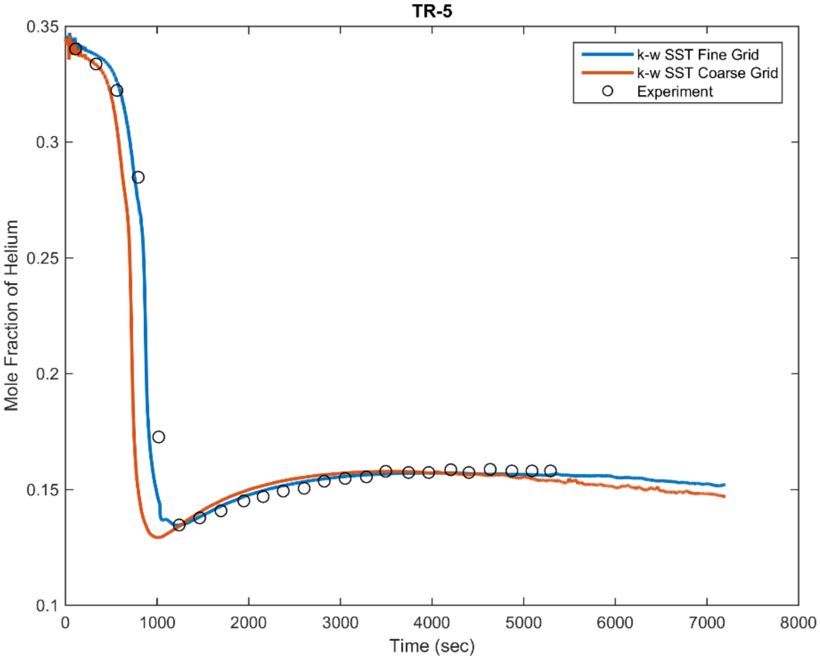

Figure 27: Mole fraction of helium vs. time (s) for mesh sensitivity at point TR-5

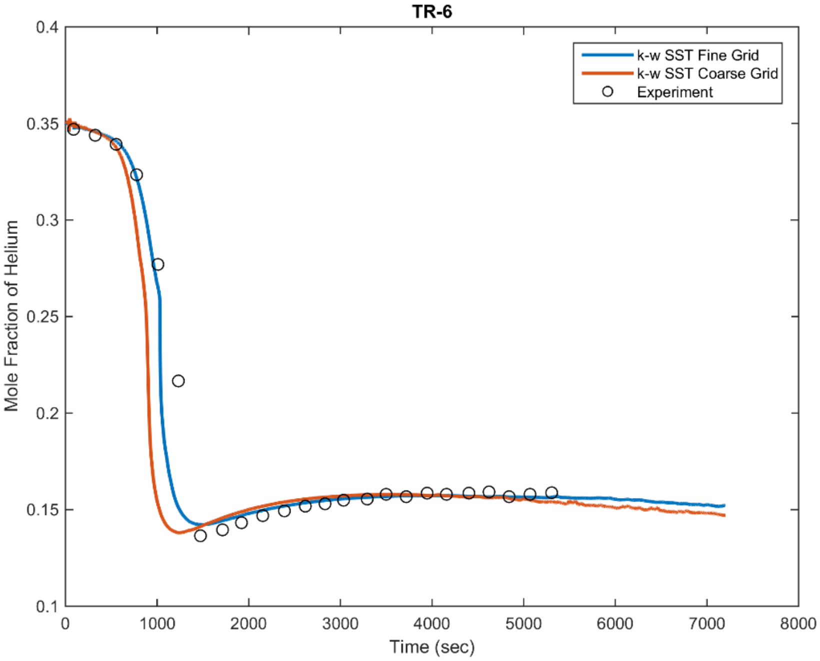

Figure 28: Mole fraction of helium vs. time (s) for mesh sensitivity at point TR-6

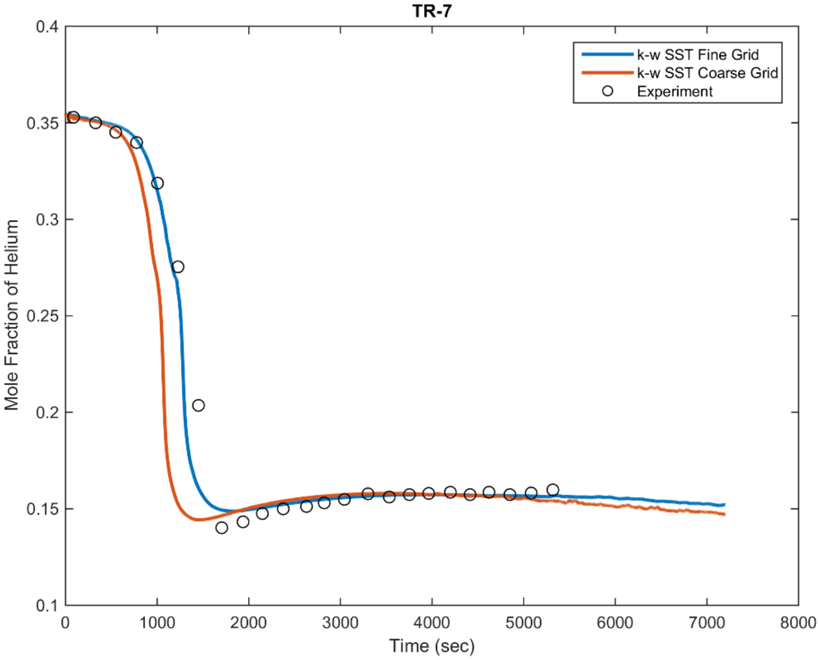

Figure 29: Mole fraction of helium vs. time (s) for mesh sensitivity at point TR-7

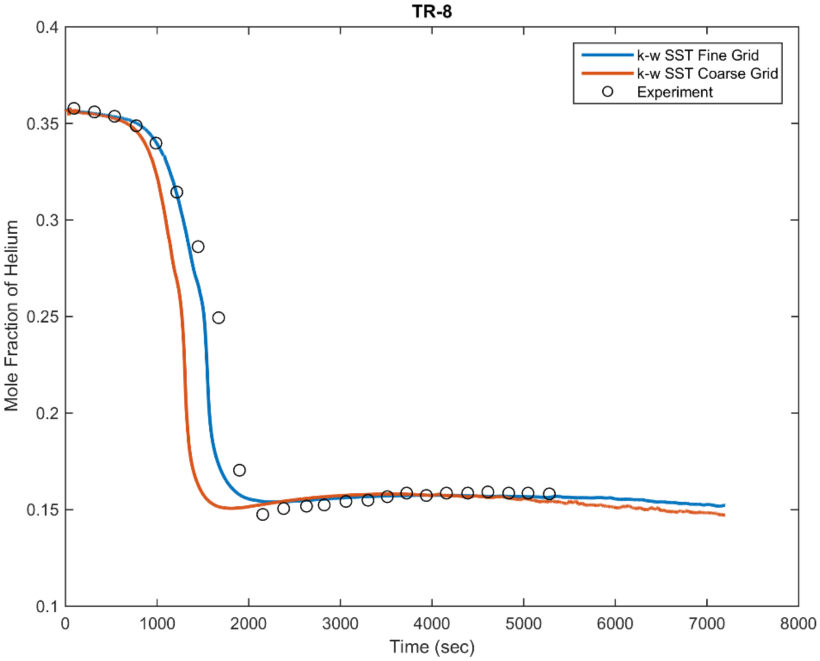

Figure 30: Mole fraction of helium vs. time (s) for mesh sensitivity at point TR-8

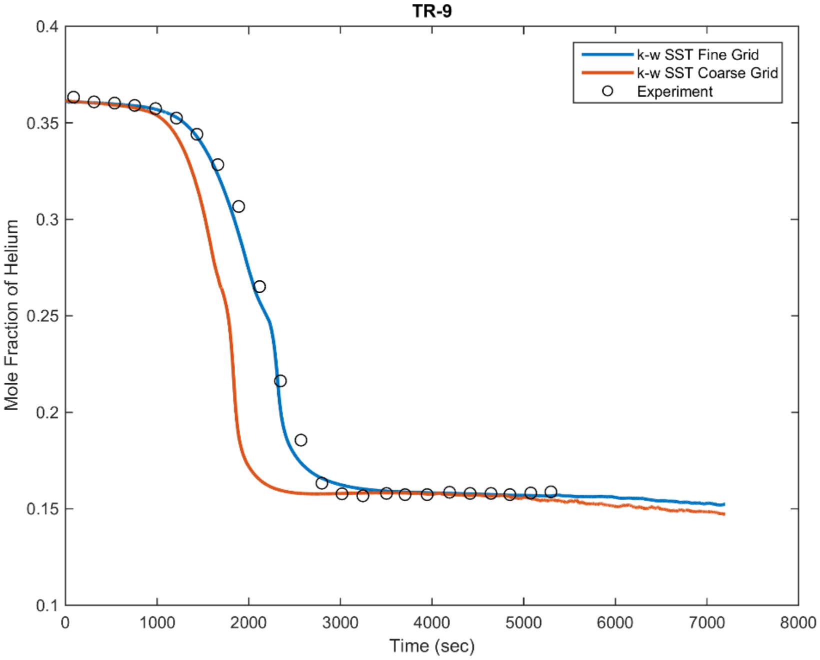

Figure 31: Mole fraction of helium vs. time (s) for mesh sensitivity at point TR-9

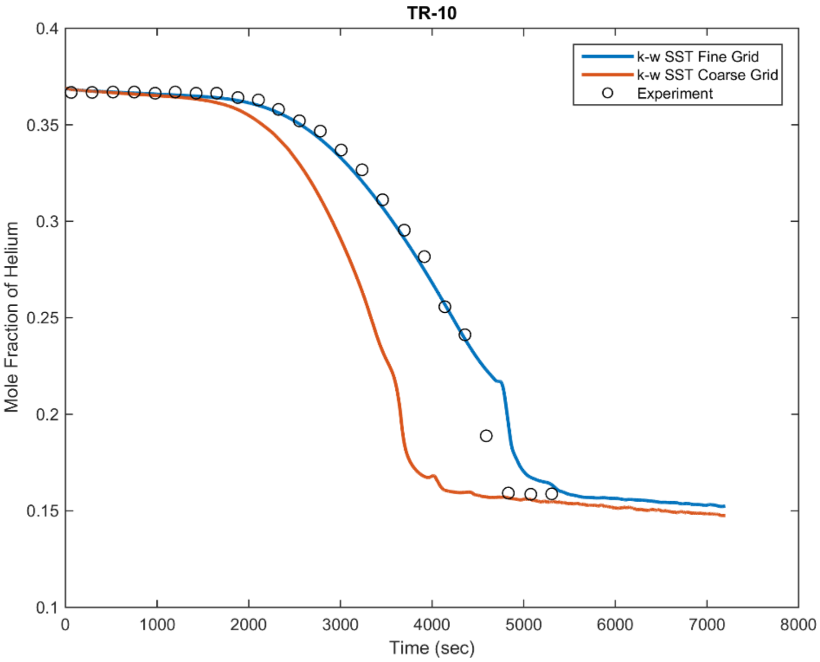

Figure 32: Mole fraction of helium vs. time (s) for mesh sensitivity at point TR-10

The grid sensitivity study show that the grid resolution has more significant affect for the region that has stronger density gradient. The erosion at the lower part of the stratified layer are closer for both coarse and fine grid as shown at points TR-1 , TR-2 and TR-3. However, the mole fraction of the helium for the different grid resolution shows higher variation at the upper region of the stratified layer due to the higher density gradient. For instance TR-7, TR- 8 and TR-9 points proved that. The higher density gradient at the upper region causes higher fluctuation on the velocity due to body force term, which has a multiplication of the density difference between cell value and the reference density value. The mesh refinement in the mixing region was applied uniformly. The sensitivity results indicated that the axial variation of the refinement level helps to obtain higher accuracy results with less computational cost. The base size of the cells has to decrease with the increasing density gradient.

In addition to the stratified layer, the mole concentration were measured at different locations in the PANDA vessel to evaluate the global mixing of the gas components as show in Figures 33-38. Specifically, Figure 36, Figure 37 and Figure 38 presents the mixing results far from the jet injection axis near to the vessel wall. The mixing at those points are driven by the reversed flow after jet hit the stratified layer. Therefore, the difference between coarse and fine mesh results are not significant in the first 4000 seconds of the simulation, after this point the results are slightly different due to faster diffusion of the coarse mesh at the higher gradient region. This can be observed at the outlet of the vessel as given in Figure 38. Overall, the results for global mixing and erosion of the stratified layer concluded that the fine grid can be used for the rest of the study. The mixing and the erosion of the gas components are well predicted except at the point MS-9 as shown in Figure 35. The possible reason is the wall treatment at the region above MS-9. In this region wall has stronger effect on the flow than rest of the domain. The finer resolution of the near-wall region at the top of the vessel might solve this slower diffusion.

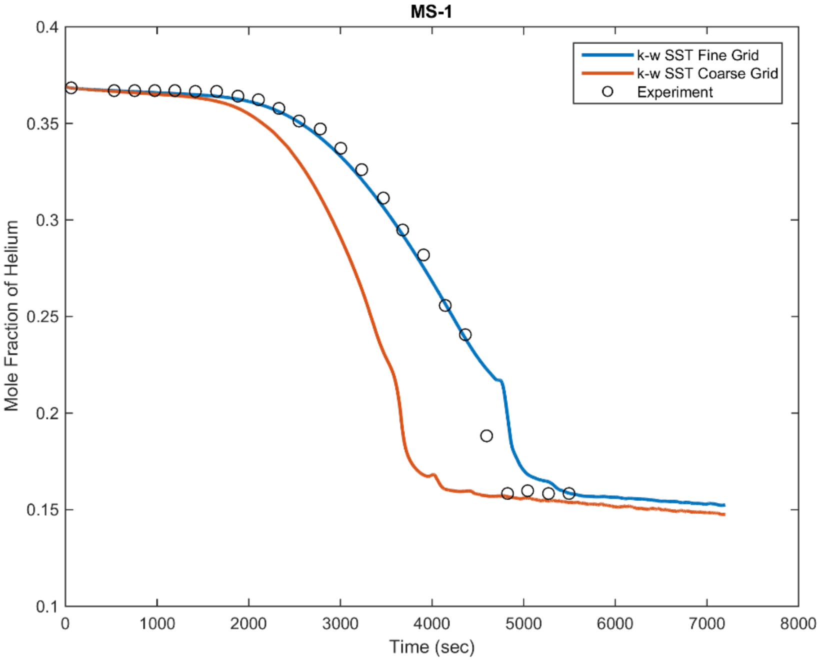

Figure 33: Mole fraction of helium vs. time (s) for mesh sensitivity at point MS-1

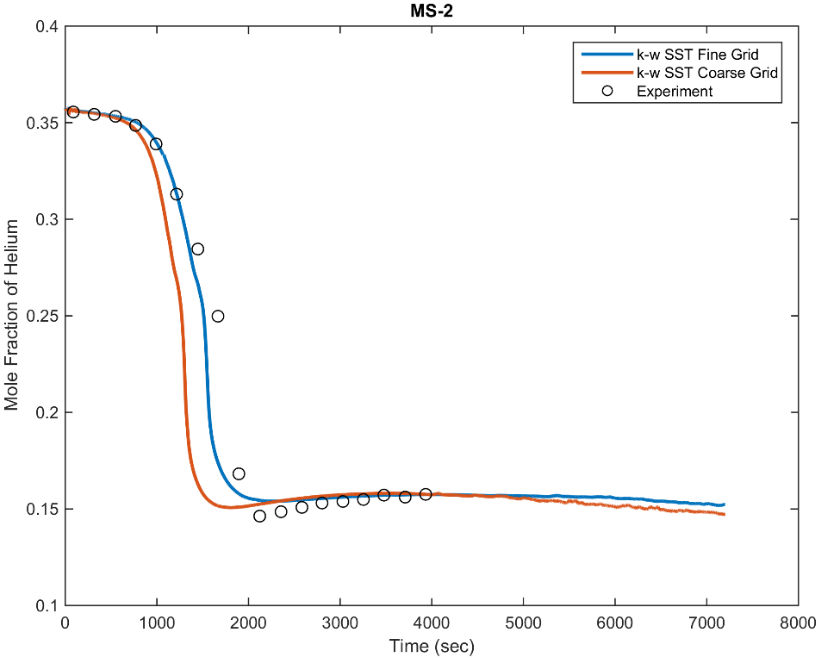

Figure 34: Mole fraction of helium vs. time (s) for mesh sensitivity at point MS-2

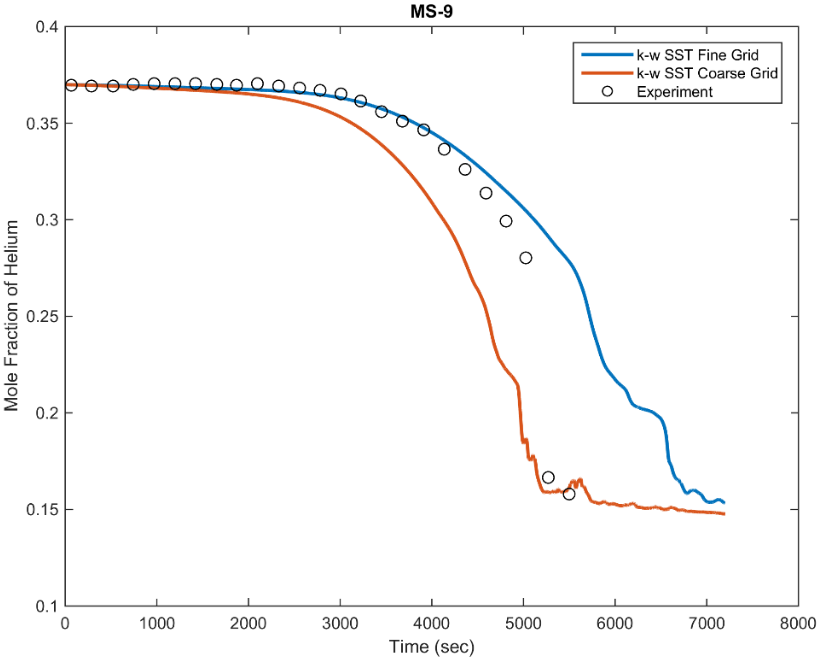

Figure 35: Mole fraction of helium vs. time (s) for mesh sensitivity at point MS-9

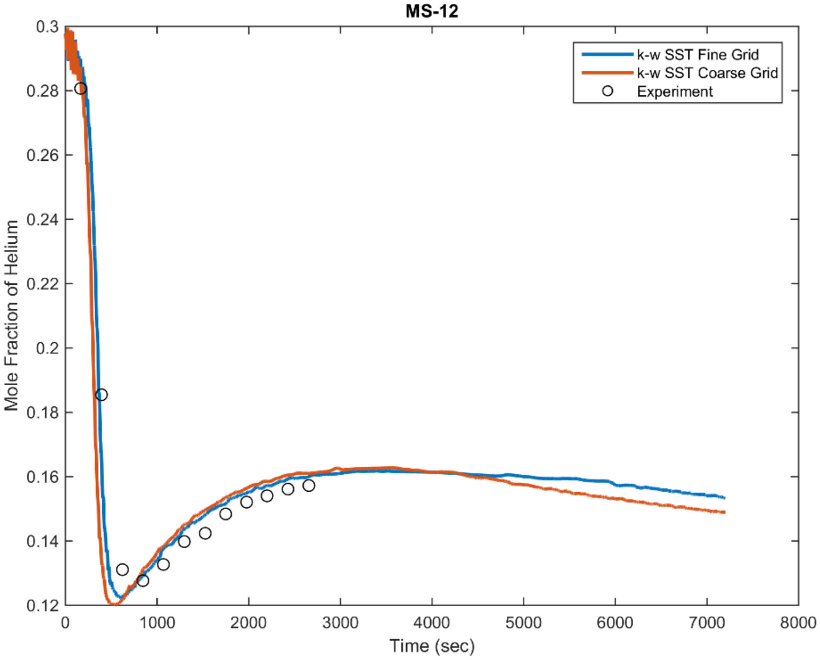

Figure 36: Mole fraction of helium vs. time (s) for mesh sensitivity at point MS-12

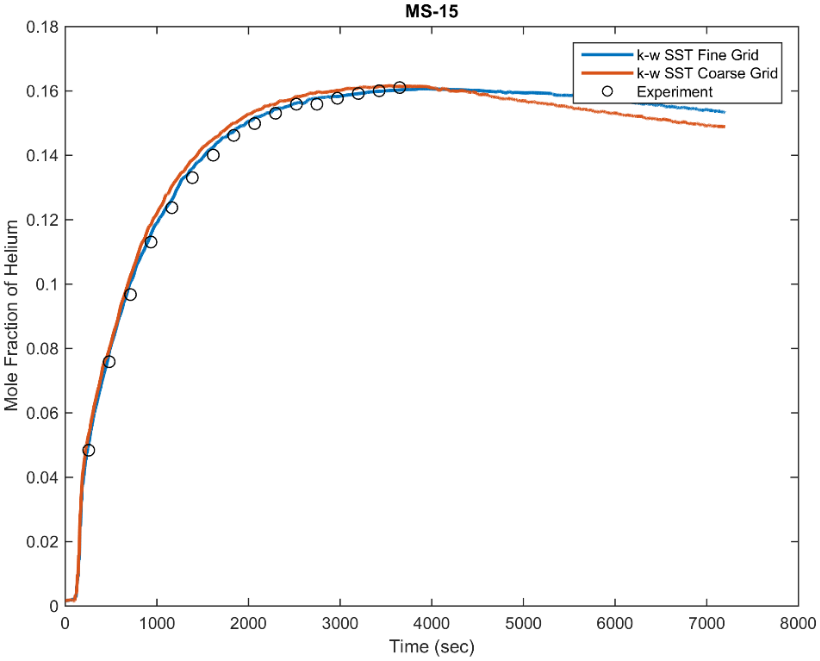

Figure 37: Mole fraction of helium vs. time (s) for mesh sensitivity at point MS-15

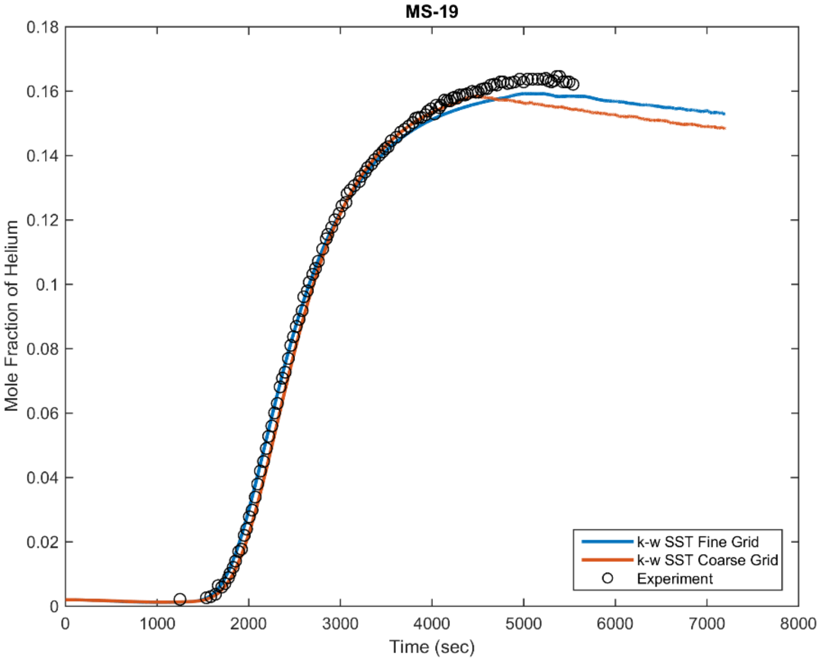

Figure 38: Mole fraction of helium vs. time (s) for mesh sensitivity at point MS-19

VI.1.2 Velocity and Turbulent Kinetic Energy Results

The velocity and turbulent kinetic energy data are averaged over a time period of 204.6 s by using PIV data. The CFD simulation results are averaged over an equal time period. The solution time will refer to the time in the middle of this averaging period. Solution time for HVY-3, HVY-5, VVY-1 and TKE-2 are 1213, 1795, 111, 1213 seconds respectively as shown in Figures 39-42.

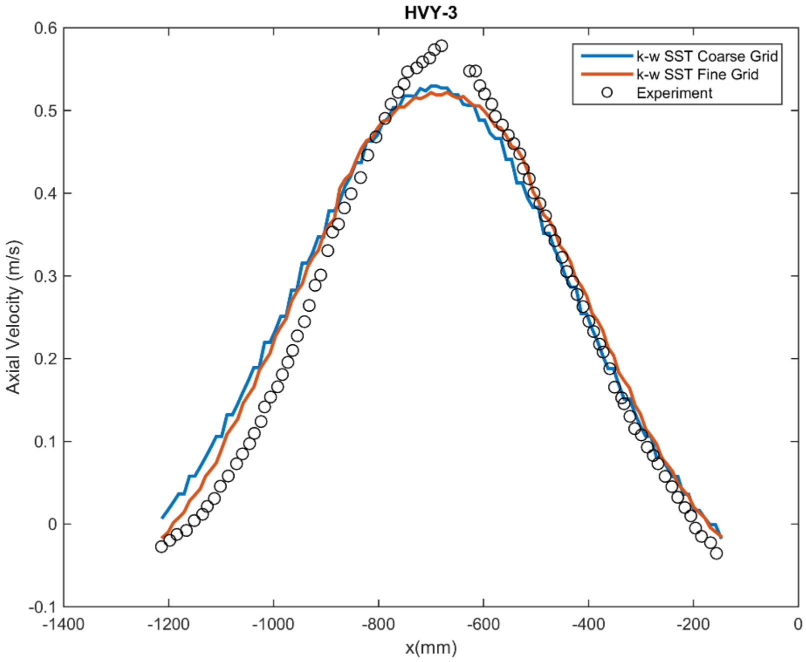

Figure 39: Averaged axial velocity profile for mesh sensitivity at 1213 s.

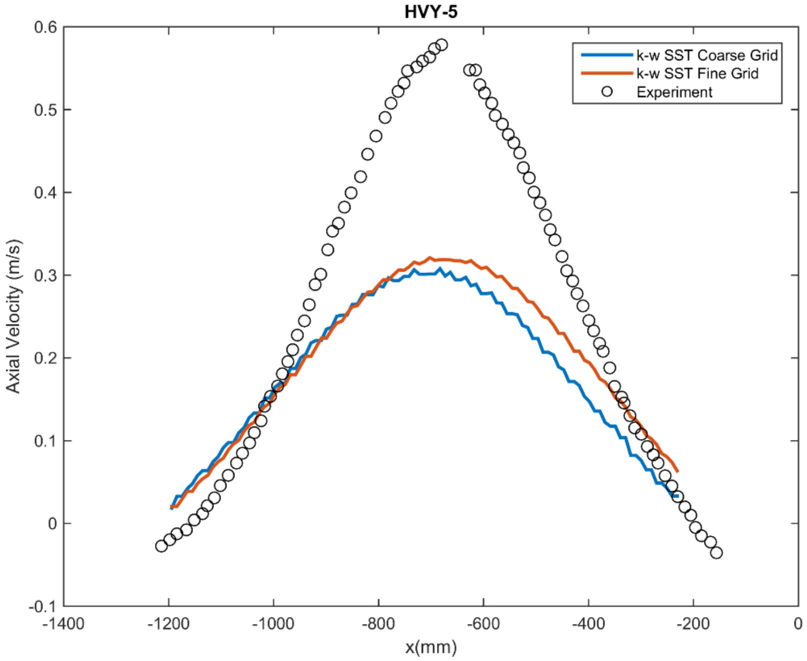

Figure 40: Averaged axial velocity profile for mesh sensitivity at 1795 s.

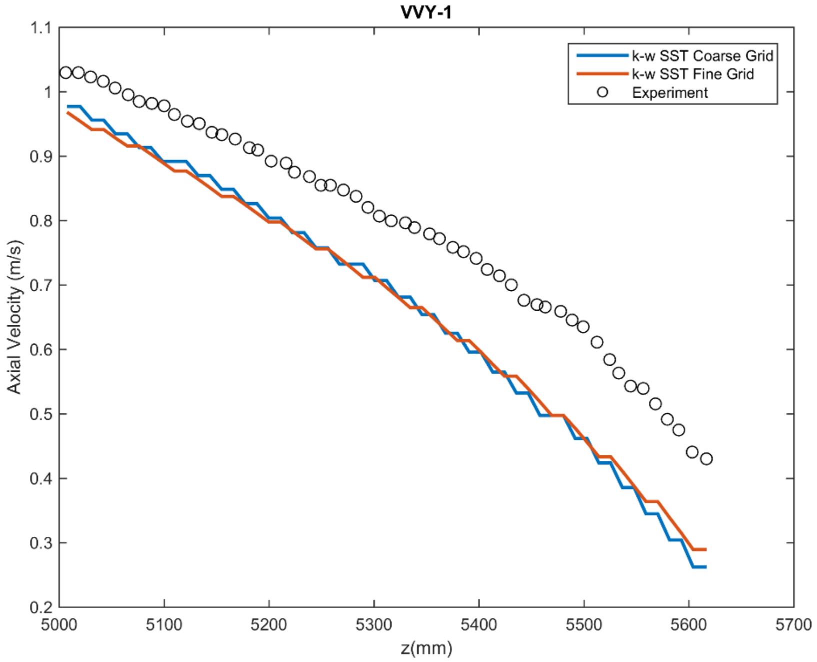

Figure 41: Averaged axial velocity profile for mesh sensitivity at 111 s.

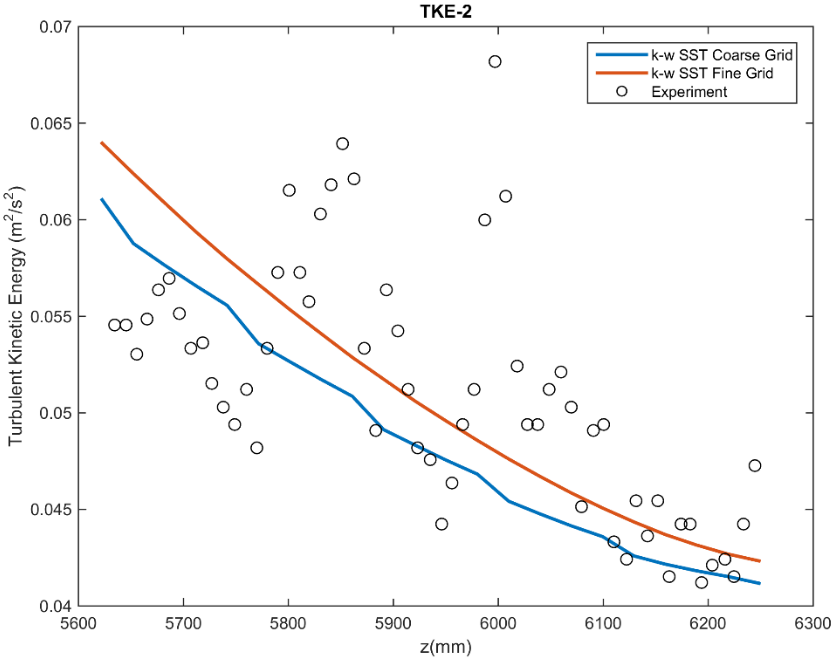

Figure 42: Averaged turbulent kinetic energy on a horizontal line (TKE-2) at 1213 s.

The results show that at the bottom part of the stratified layer is good agreement with the experimental data. But the velocity at the upper part of the layer is underestimated. While the diffusion of the gas components are well predicted, the velocities are underestimated. This can be explained by the diffusion mechanism. The diffusion of the gas components is compensated by the turbulent diffusion at the upper region of the stratified layer, while the lower part of the layer has a better balance between turbulent diffusion and laminar diffusion. This can be confirmed by the vertical profile of the axial velocity as shown in Figure 41.

VI.1.3 Temperature Results

The specification of the experiment reported that the all external surfaces have been insulated perfectly and the heat loss was examined by an independent experiment. The steam (145 ^{0}C) was injected to the vessel and the cool-down was measured for two days. The report indicated that heat loss for actual experiment is too small. However, the temperature results proved that the heat losses cannot be neglected as shown in Figure 43 and Figure 44. At the beginning of the experiment, the temperature was predicted with good agreement, after a thousand seconds, the temperature was over predicted due to neglected heat transfer from the vessel surface.

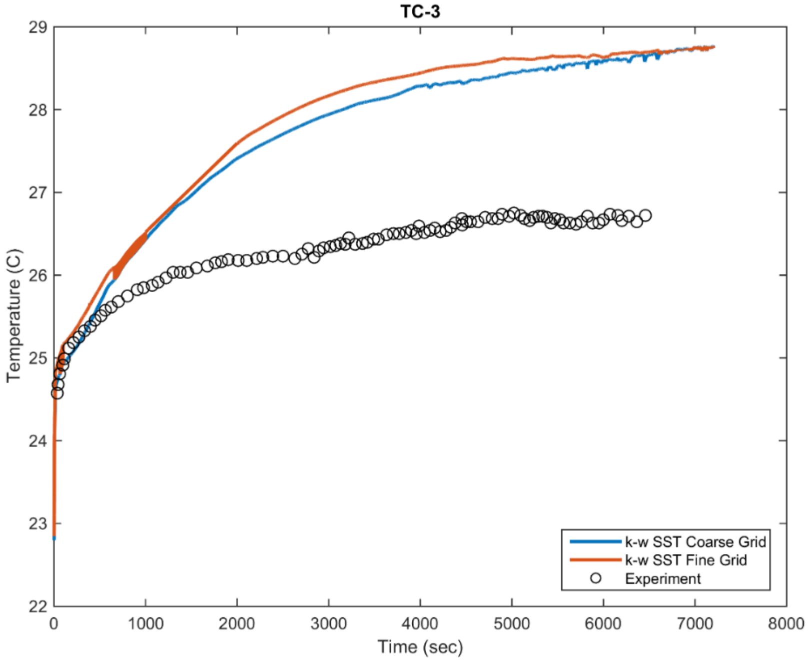

Figure 43: Temperature (^{0}C) vs. time (s) for mesh sensitivity at point TC-3

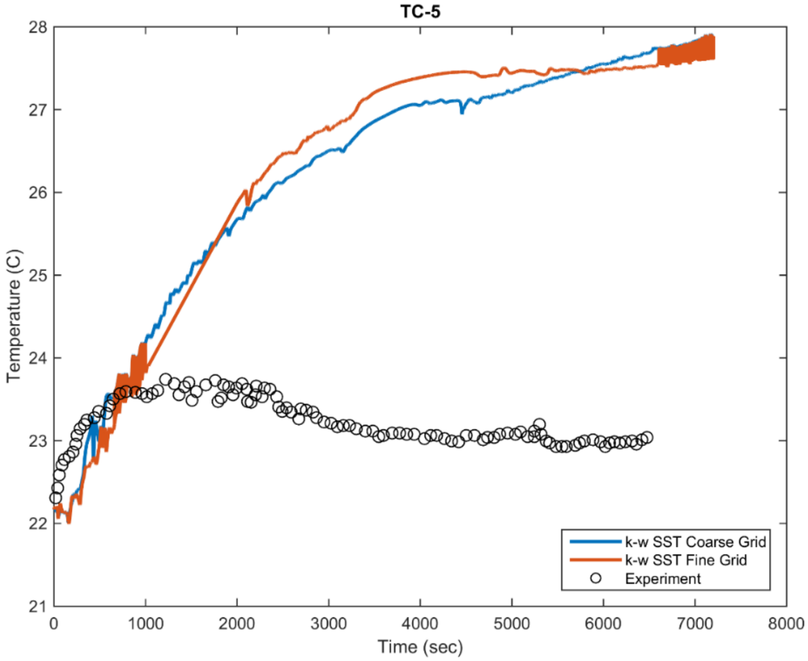

Figure 44: Temperature (^{0}C) vs. time (s) for mesh sensitivity at point TC-5

VI.2 Realizable $\mathbf{k} - \epsilon$ Results

The results of the simulation results by using Realizable $k - \epsilon$ turbulence model will be discussed in this part by comparing the numerical and experimental results. In this part only fine grid is used. It is expected that the Realizable $k - \epsilon$ turbulence model with two-layer approach predicts similar mixing results with $k - \omega$ SST turbulence model. The reason is that the SST model is using the $k - \epsilon$ model in the center of the flow domain, while it is using standard $k - \omega$ near wall region.

VI.2.1 Mole Fraction Results

The following Figures 45-54 show that the mole fraction of the helium in the stratified layer to evaluate the Realizable $k-\epsilon$ turbulence model including comparison with $k-\omega$ SST fine grid results. The both models result in identical result at the lower portion of the stratified layer, while $k-\omega$ SST performed better at the higher density gradient region of the stratified layer.

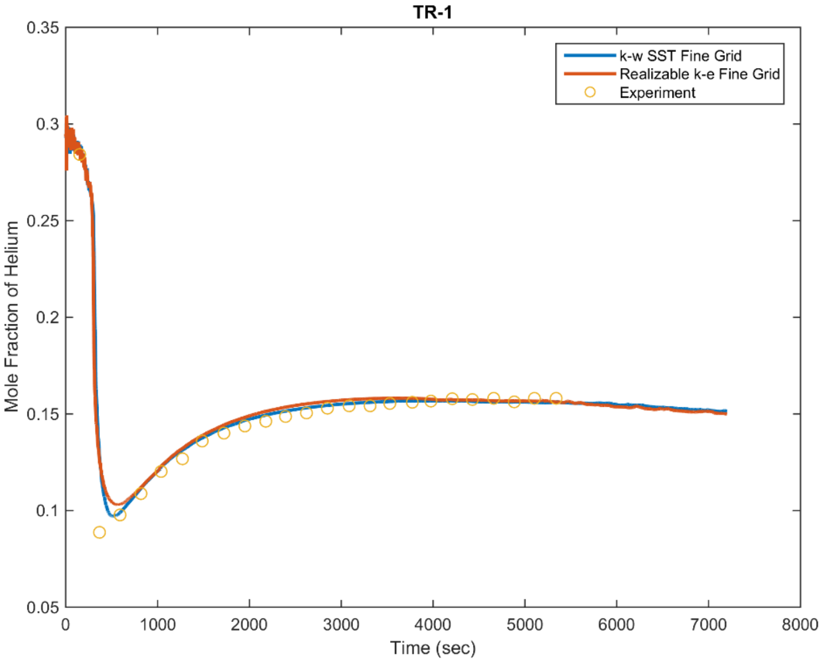

Figure 45: Mole fraction of helium vs. time (s) for Realizable $\boldsymbol{k-\epsilon}$ model at TR-1

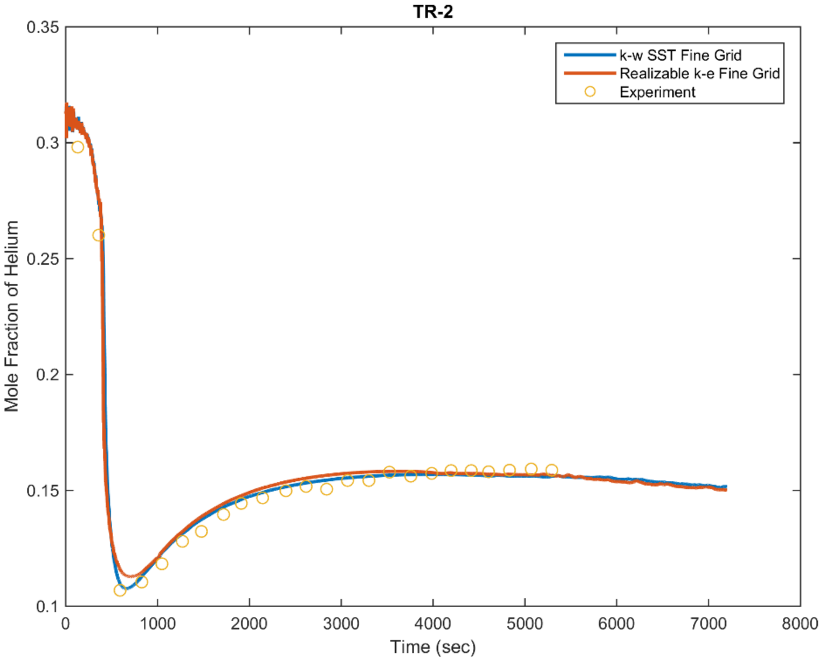

Figure 46: Mole fraction of helium vs. time (s) for Realizable $\boldsymbol{k}-\boldsymbol{\epsilon}$ model at TR-2

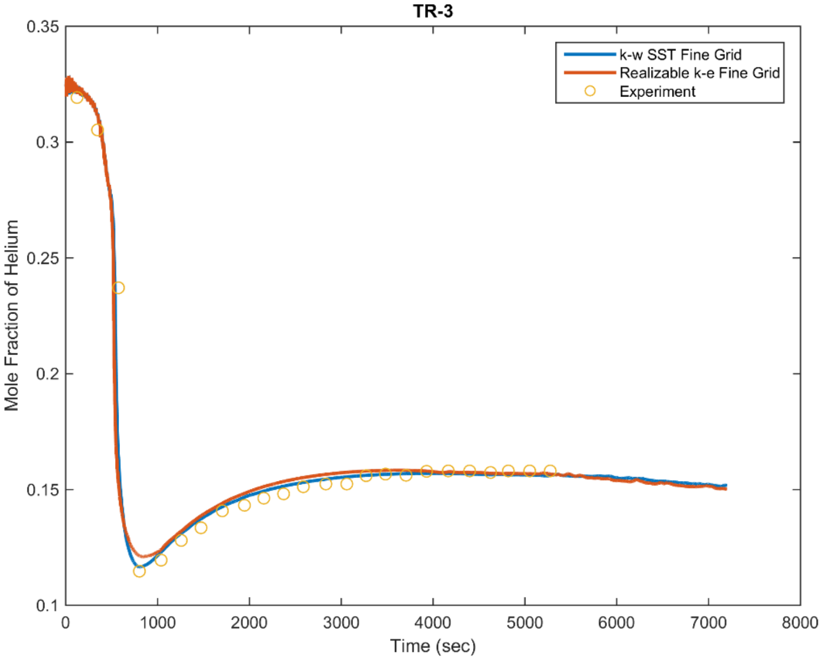

Figure 47: Mole fraction of helium vs. time (s) for Realizable $\boldsymbol{k}-\boldsymbol{\epsilon}$ model at TR-3

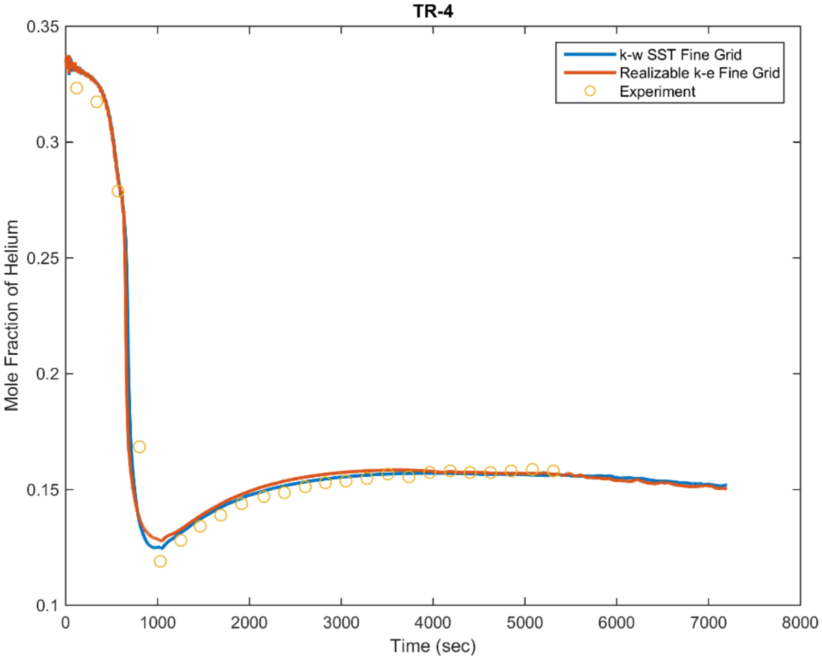

Figure 48: Mole fraction of helium vs. time (s) for Realizable $\boldsymbol{k-\epsilon}$ model at TR-4

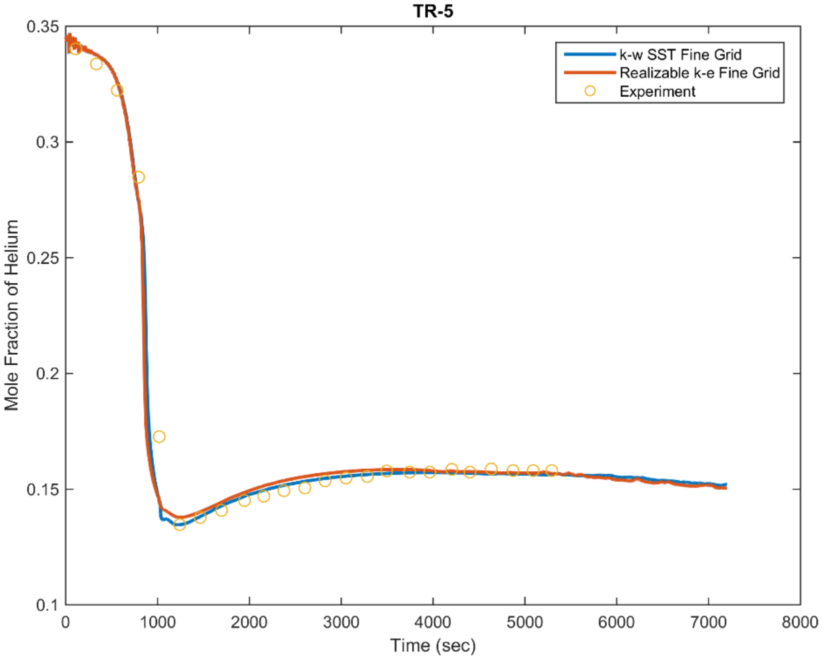

Figure 49: Mole fraction of helium vs. time (s) for Realizable $\boldsymbol{k-\epsilon}$ model at TR-5

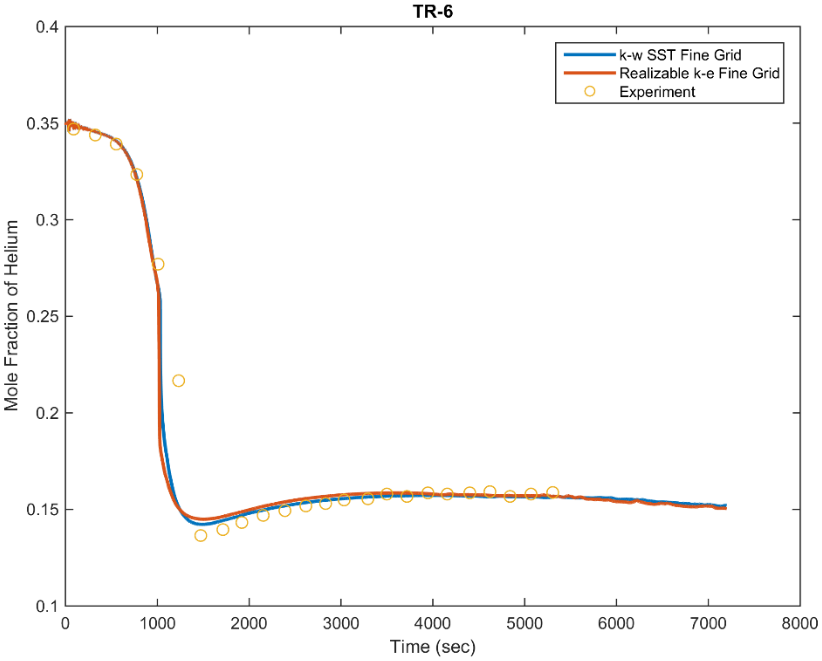

Figure 50: Mole fraction of helium vs. time (s) for Realizable $\boldsymbol{k-\epsilon}$ model at TR-6

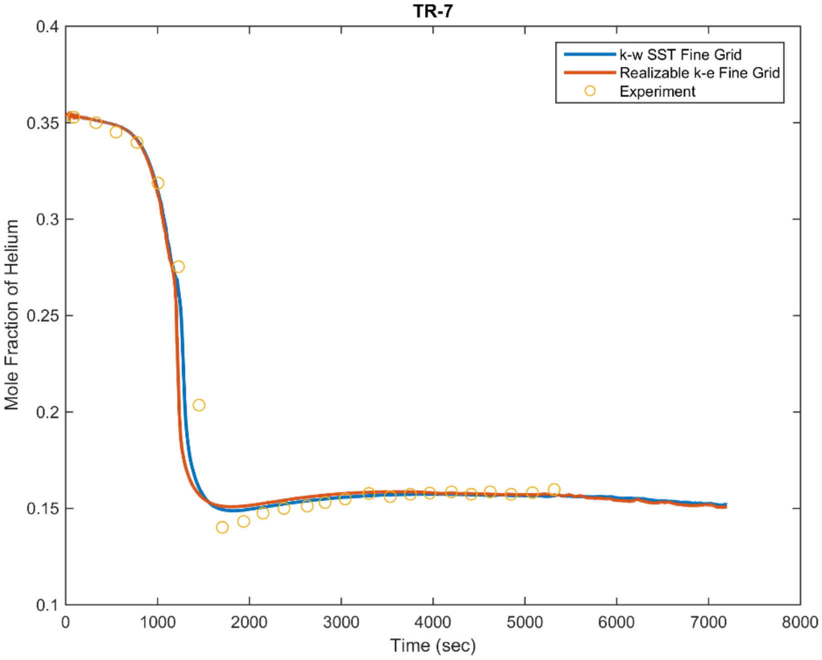

Figure 51: Mole fraction of helium vs. time (s) for Realizable $\boldsymbol{k-\epsilon}$ model at TR-7

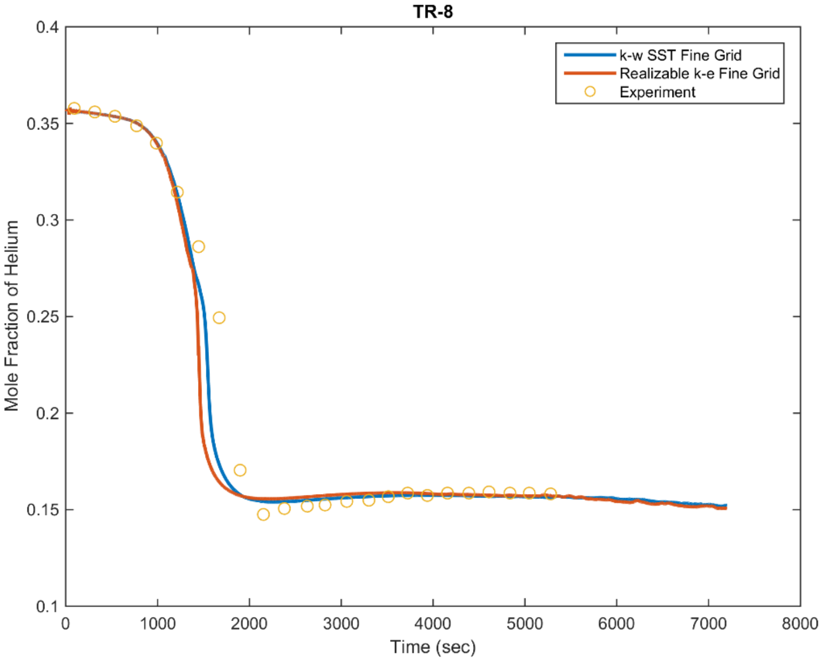

Figure 52: Mole fraction of helium vs. time (s) for Realizable $\boldsymbol{k-\epsilon}$ model at TR-8

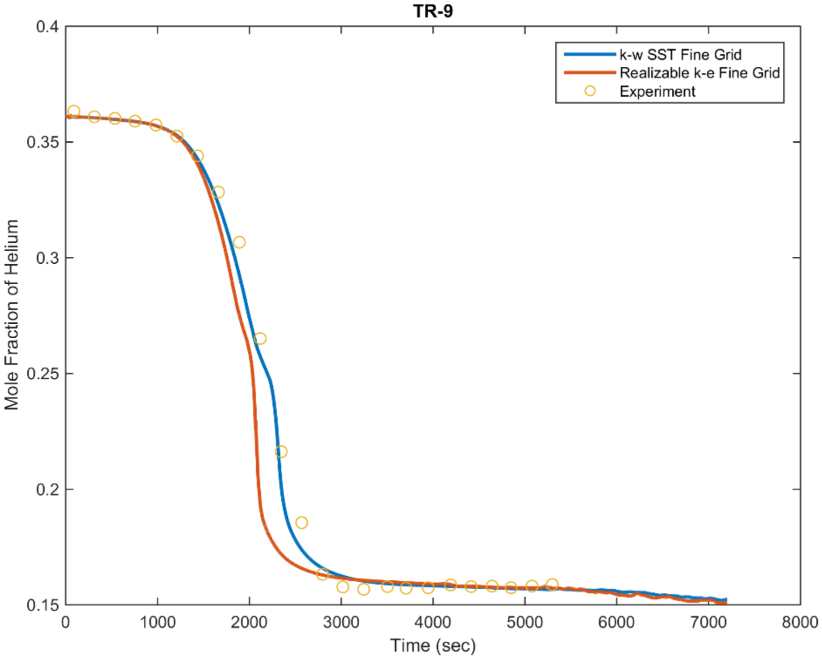

Figure 53: Mole fraction of helium vs. time (s) for Realizable $\boldsymbol{k-\epsilon}$ model at TR-9

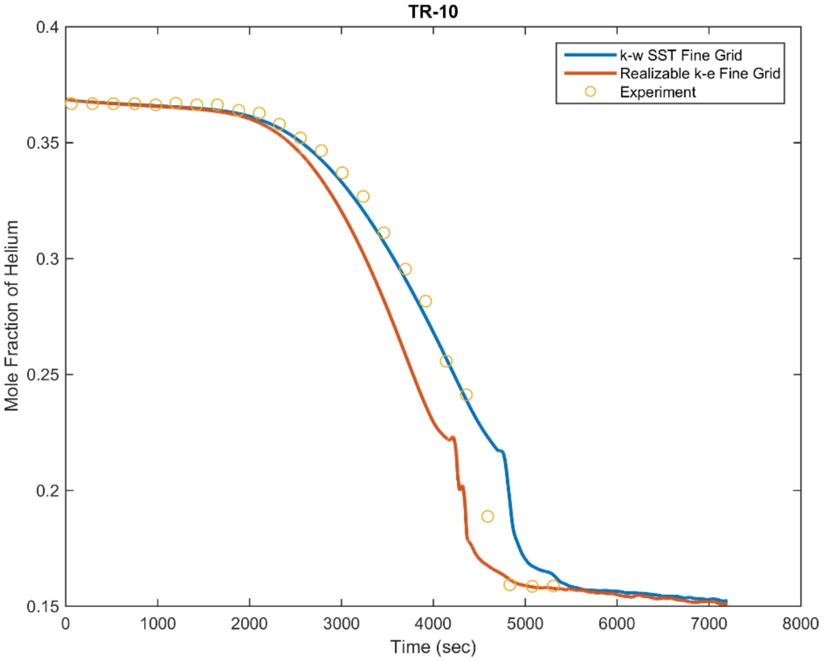

Figure 54: Mole fraction of helium vs. time (s) for Realizable $\boldsymbol{k-\epsilon}$ model at TR-10

Overall the erosion process is predicted with higher accuracy by $k-\omega$ SST model. However, at the top manhole region of the vessel in narrower than the rest of the flow domain. Consequently, the wall effect at this region is stronger and two layer h Realizable $k-\epsilon$ model with buoyancy model in the near wall layer is predicting better only at this point than SST model as shown in Figure 55. The rest of the point predicted similar results as shown in Figures 55-58.

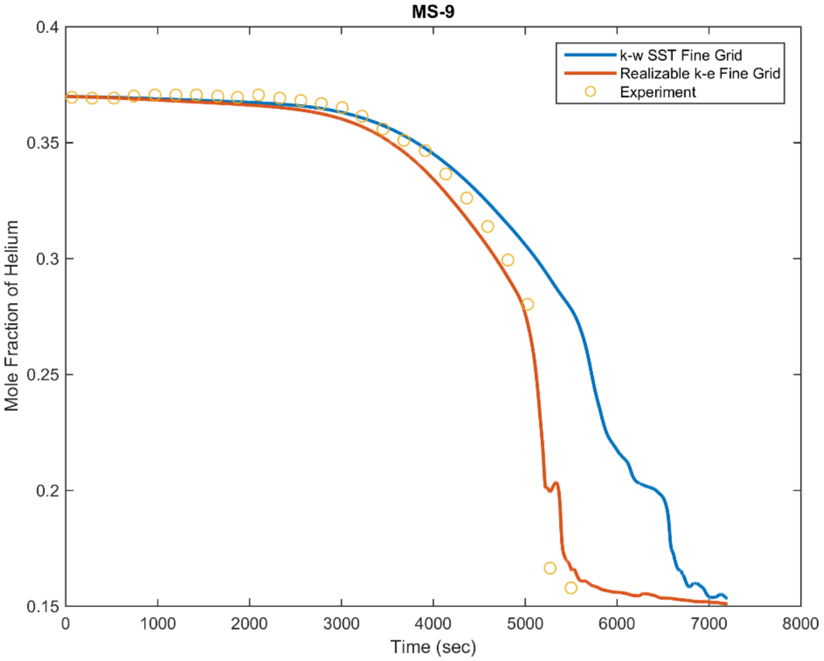

Figure 55: Mole fraction of helium vs. time (s) for Realizable $\boldsymbol{k-\epsilon}$ model at MS-9

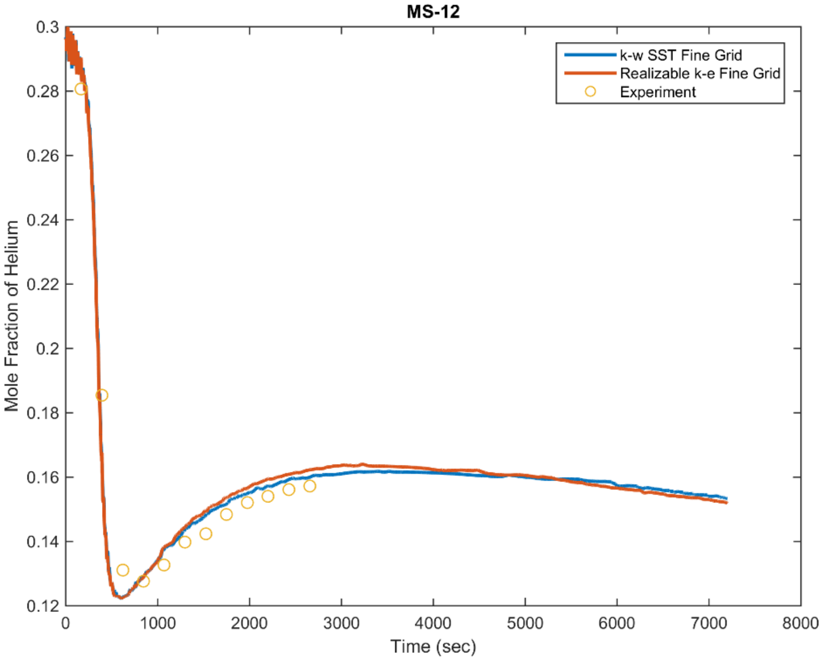

Figure 56: Mole fraction of helium vs. time (s) for Realizable $\boldsymbol{k-\epsilon}$ model at MS-12

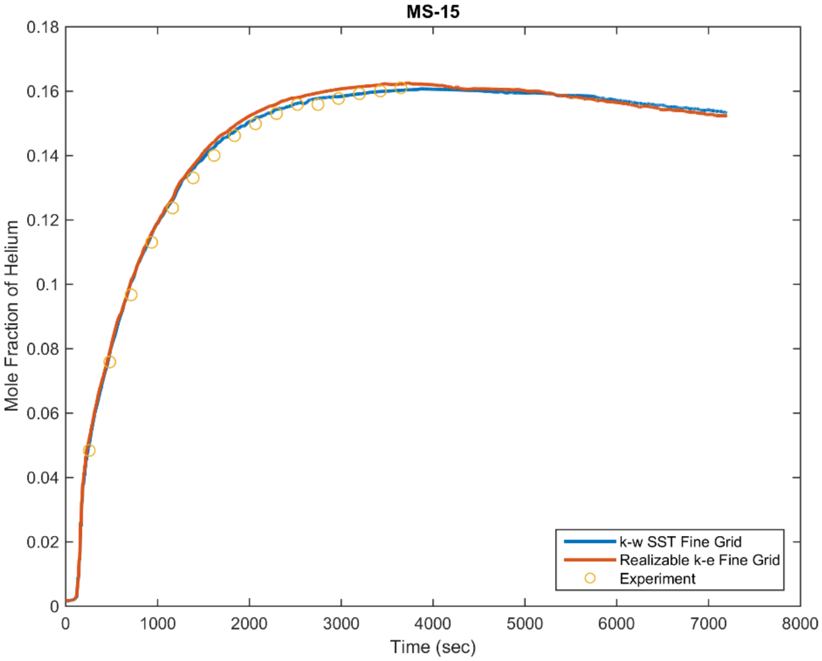

Figure 57: Mole fraction of helium vs. time (s) for Realizable $\boldsymbol{k-\epsilon}$ model at MS-15

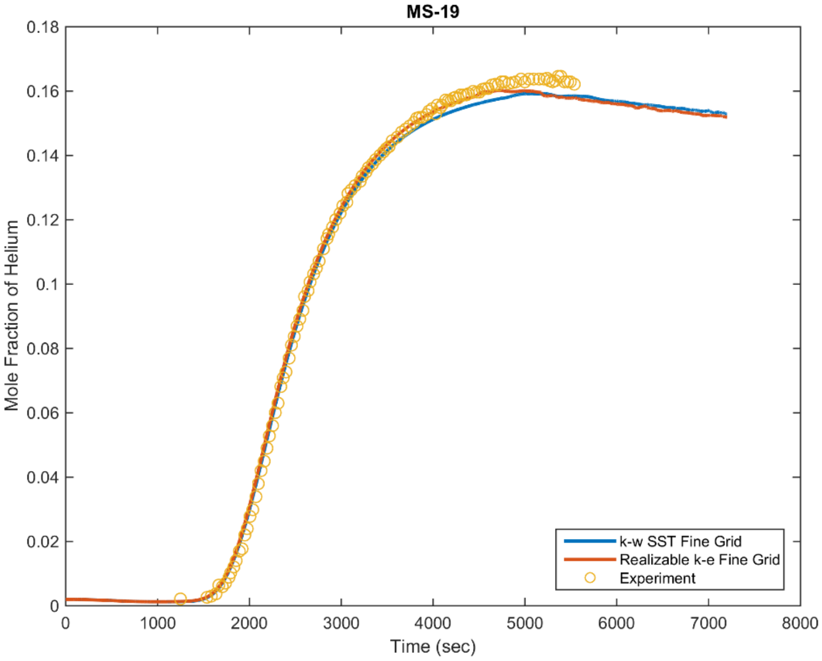

Figure 58: Mole fraction of helium vs. time (s) for Realizable $\boldsymbol{k-\epsilon}$ model at MS-19

VI.2.2 Velocity and Turbulent Kinetic Energy Results

The velocity and turbulent kinetic energy data are averaged over a time period of 204.6 s. The solution time will refer to the time in the middle of this averaging period. Solution time for HVY-3, HVY-5, VVY-1 and TKE-2 are 1213, 1795, 111, 1213 seconds respectively. As shown in Figures 59-61, the time averaged axial velocities are slightly under-predicted for both models. The averaged axial velocity on the horizontal line (HVY-3) is in better agreement with the experimental data than HVY-5. The location of the HVY-5 is higher than HVY-3 and 582 seconds late. While the velocities are under predicted, the mixing of the as components are predicted with good agreement. This case show that the components of the multi-species equation should be investigated due to less convection diffusion and more turbulent diffusion. In TKE-2 turbulent kinetic energy distribution shows high variation between two models as shown in Figure 62. It is underestimated by Realizable $k-\epsilon$ and. The better prediction of turbulent kinetic energy for the SST k-ω resulted in also better prediction of the erosion of the stratified layer.

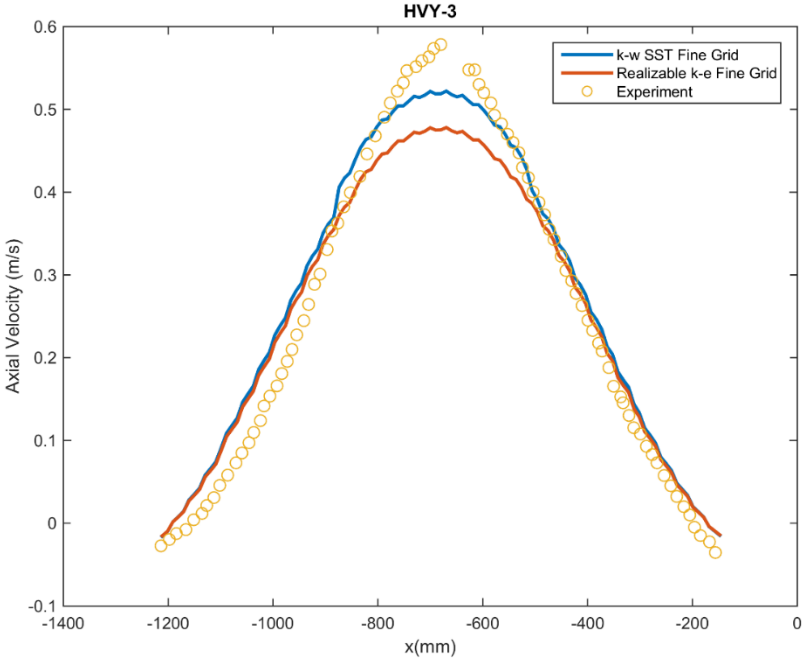

Figure 59: Averaged axial velocity profile for Realizable $\boldsymbol{k-\epsilon}$ model at 1213 s.

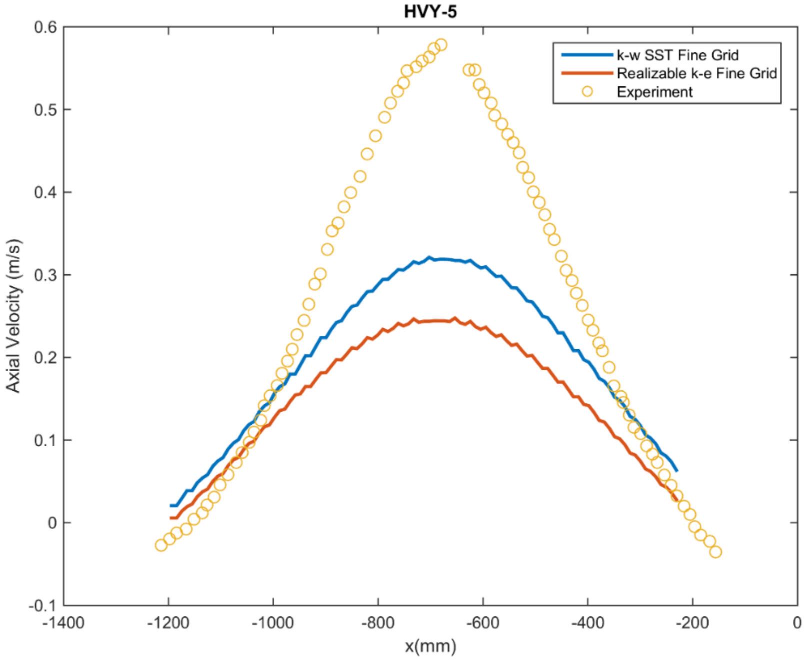

Figure 60: Averaged axial velocity profile for Realizable $\boldsymbol{k-\epsilon}$ model at 1795 s.

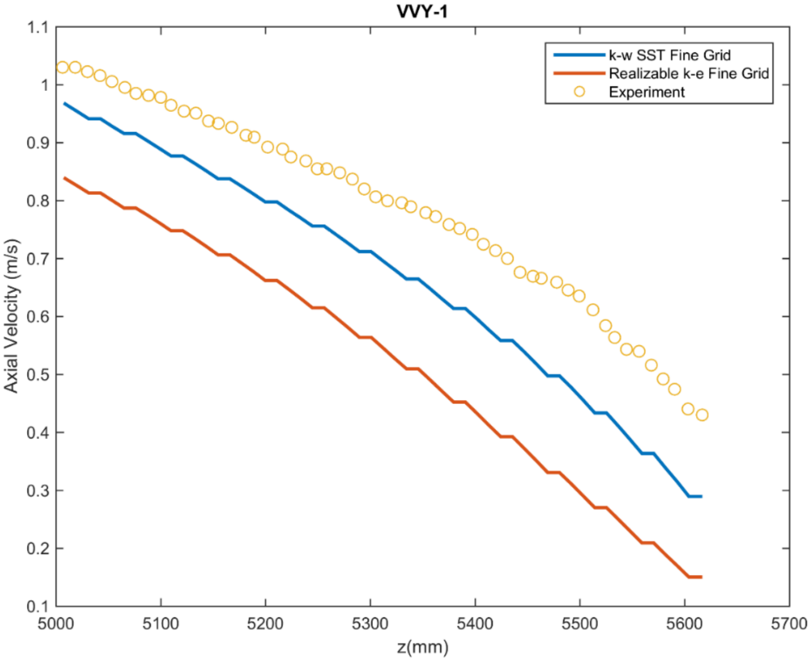

Figure 61**:** Averaged axial velocity profile for Realizable $\boldsymbol{k-\epsilon}$ model at 111 s.

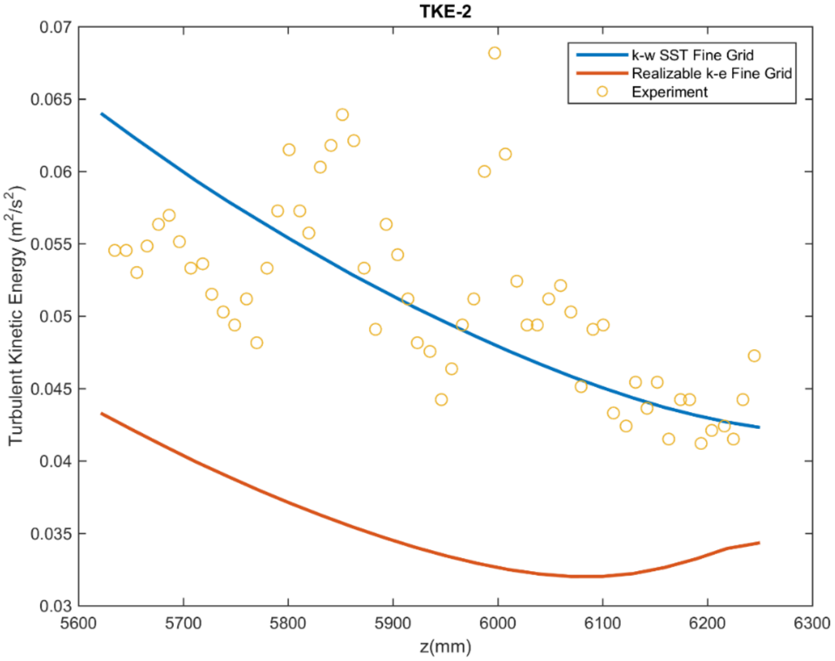

Figure 62: Turbulent kinetic energy profile for Realizable $\boldsymbol{k-\epsilon}$ model at 1213 s.

VI.2.3 Temperature Results

The temperatures are over predicted due to neglecting heat transfer from the vessel wall and temperature at two different locations for both models are consistent with each other as shown in Figure 63 and Figure 64.

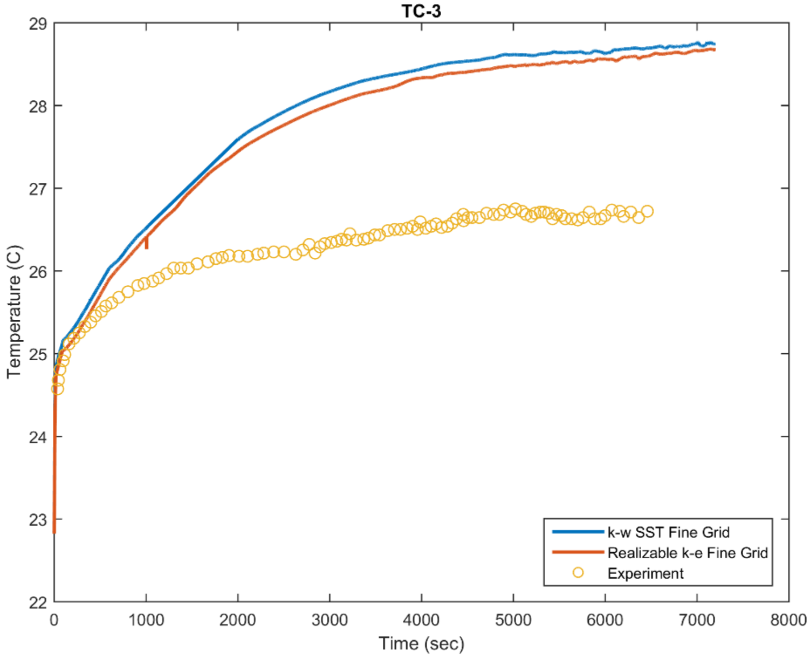

Figure 63: Temperature (^{0}C) vs. time (s) for Realizable $\boldsymbol{k-\epsilon}$ model at point TC-3

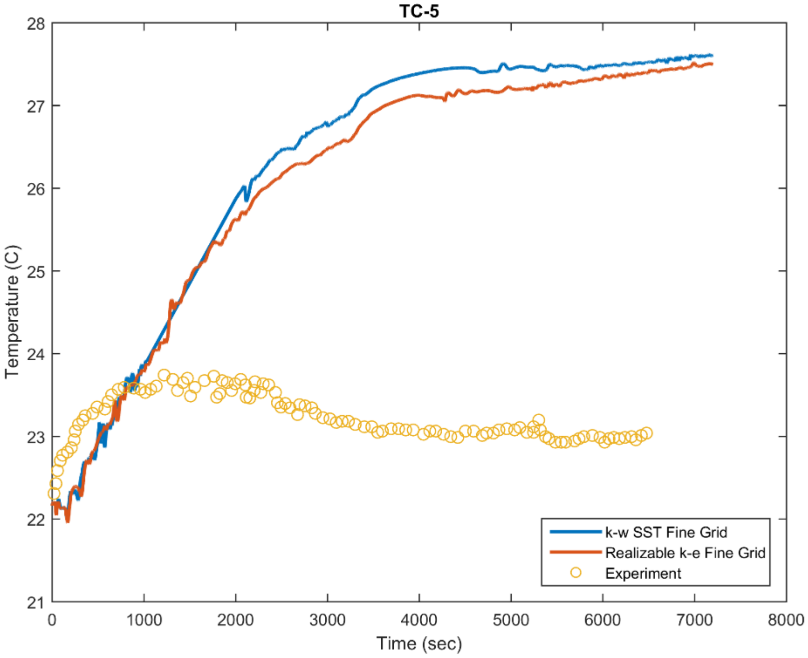

Figure 64**:** Temperature (^{0}C) vs. time (s) for Realizable $\boldsymbol{k-\epsilon}$ model at point TC-5

VI.3 Reynolds Stress Model Results

In this section all results of the RANS models including eddy viscosity and Reynolds Stress model with fine grid are presented and discussed.

VI.3.1 Mole Fraction Results

The Reynolds Stress Model (RSM) is developed to account anisotropy for the Reynolds stress tensor (RST). In general two equation models do not account for anisotropy due to isotropic eddy viscosity assumption in the model. However, the RSM has a numerical stability problem due to the stiffness of the RST equations. In the RSM simulation, the interactions of the incoming jet and the stratified layer caused stability problems due to density gradient, specifically, at the time of the incoming jet reached at the upper level of the stratified layer. It can be seen in Figures 65-74 (after 4000 seconds). After 4000 seconds, the sharp density gradient in axial direction, and zero density gradient in radial direction causes more stability problem due to the stronger anisotropy of the RST components.

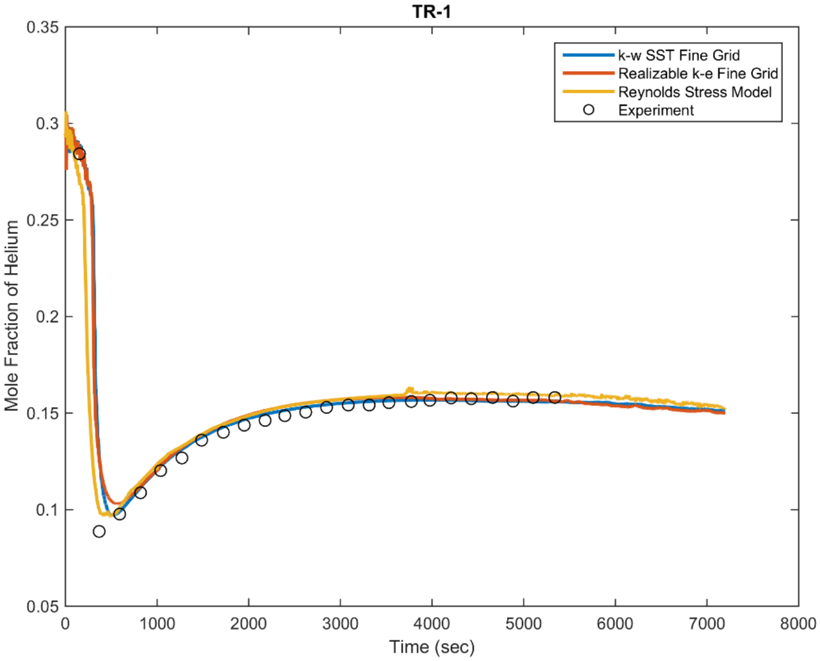

Figure 65: Mole fraction of helium vs. time (s) for RSM at TR-1

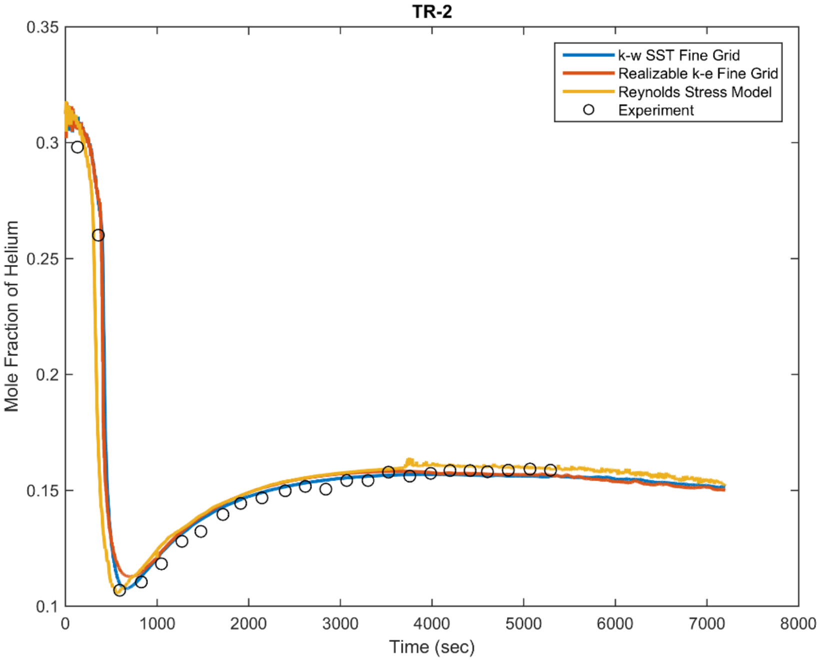

Figure 66: Mole fraction of helium vs. time (s) for RSM at TR-2

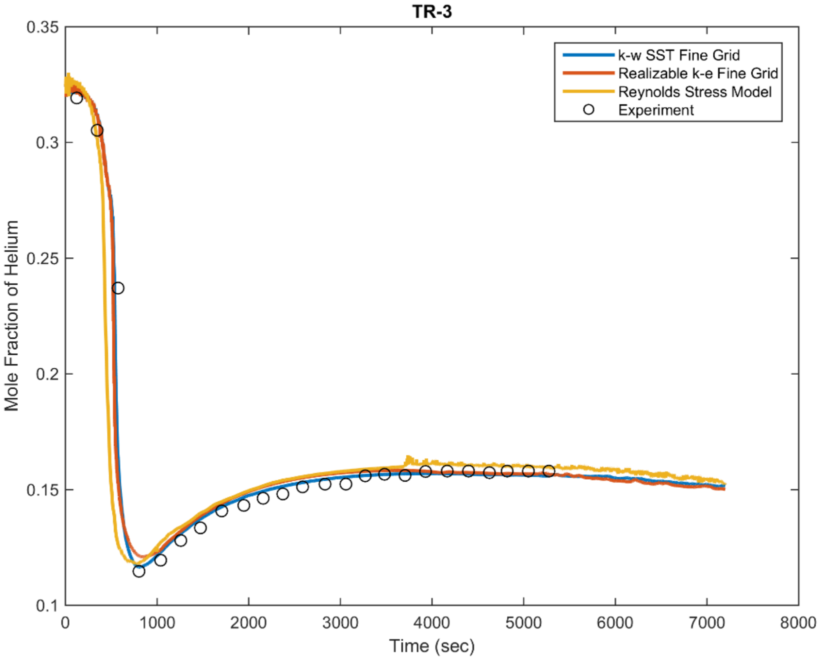

Figure 67: Mole fraction of helium vs. time (s) for RSM at TR-3

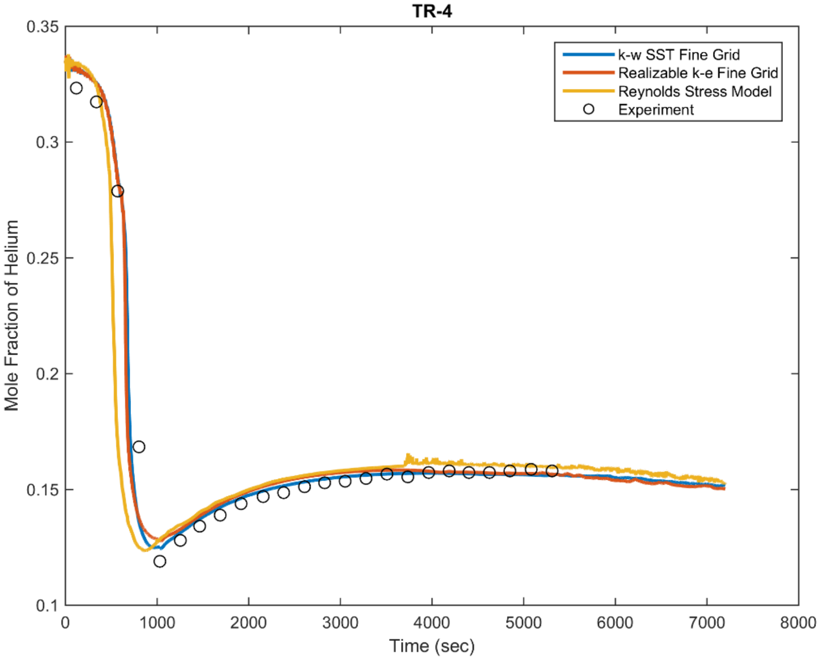

Figure 68: Mole fraction of helium vs. time (s) for RSM at TR-4

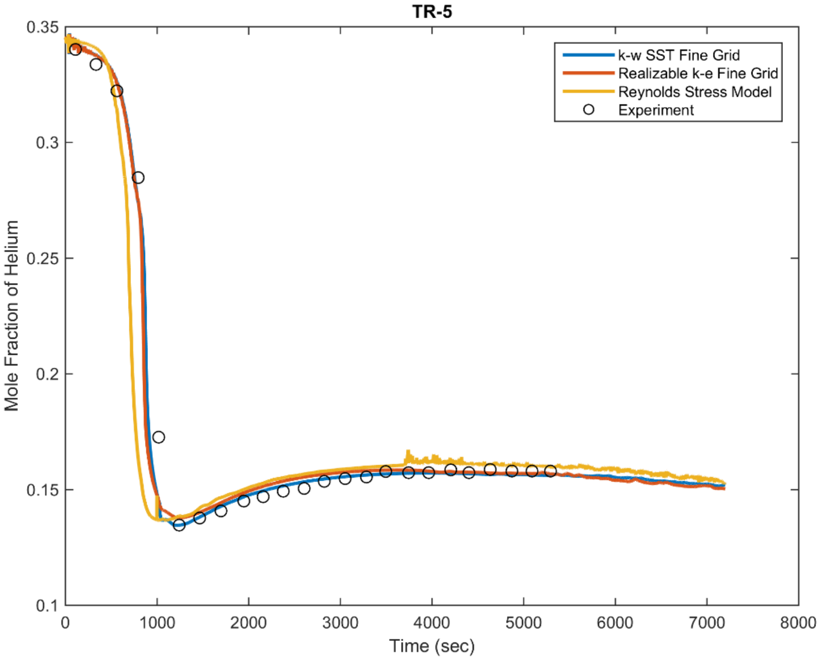

Figure 69: Mole fraction of helium vs. time (s) for RSM at TR-5

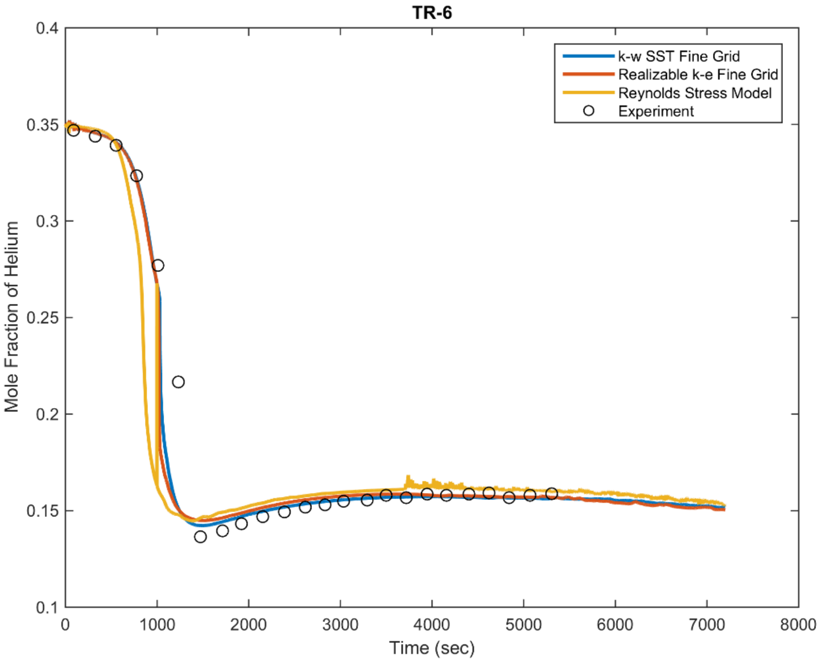

Figure 70: Mole fraction of helium vs. time (s) for RSM at TR-6

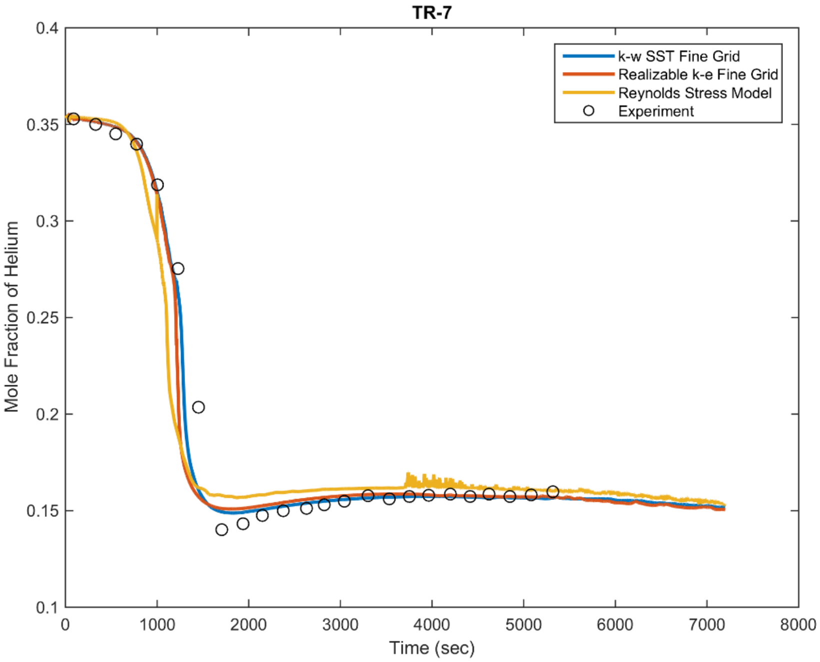

Figure 71: Mole fraction of helium vs. time (s) for RSM at TR-7

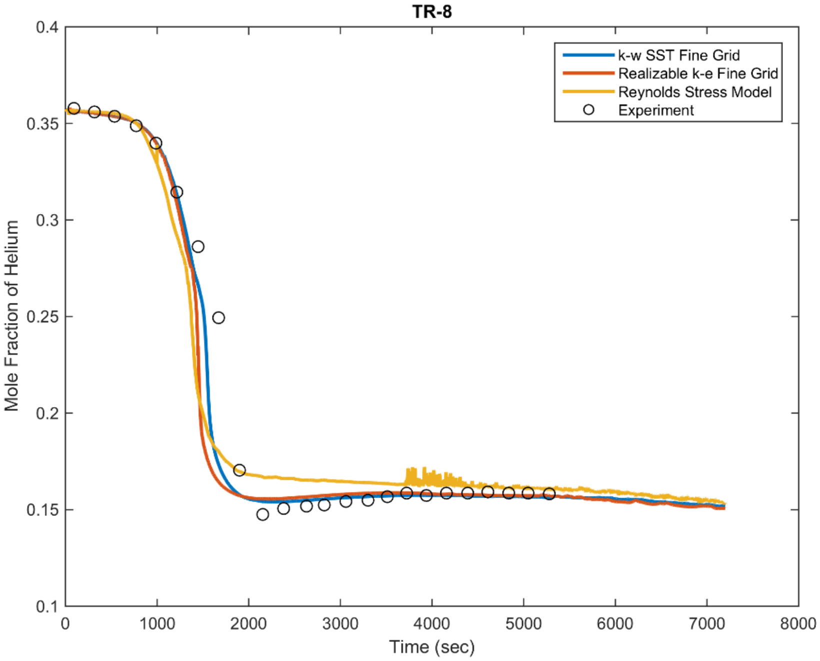

Figure 72: Mole fraction of helium vs. time (s) for RSM at TR-8

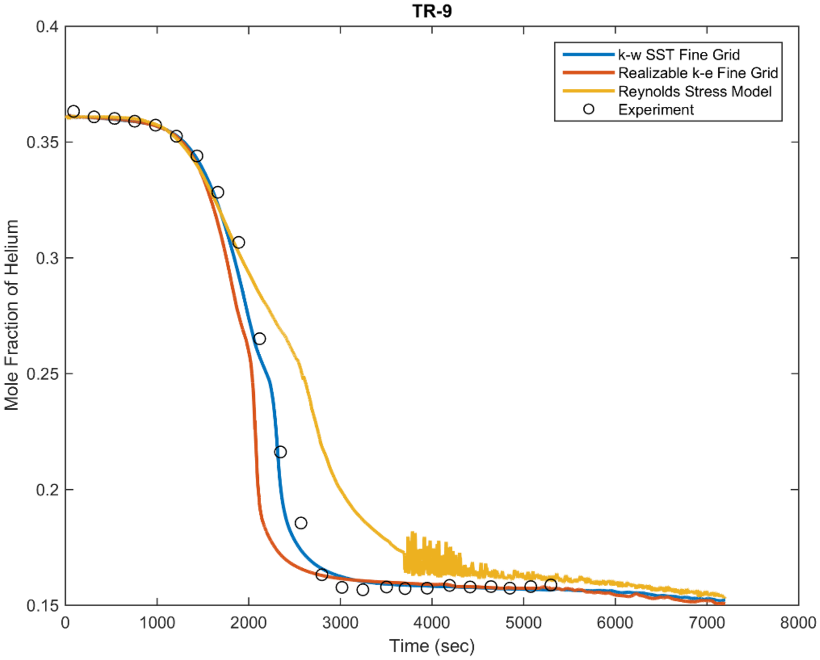

Figure 73: Mole fraction of helium vs. time (s) for RSM at TR-9

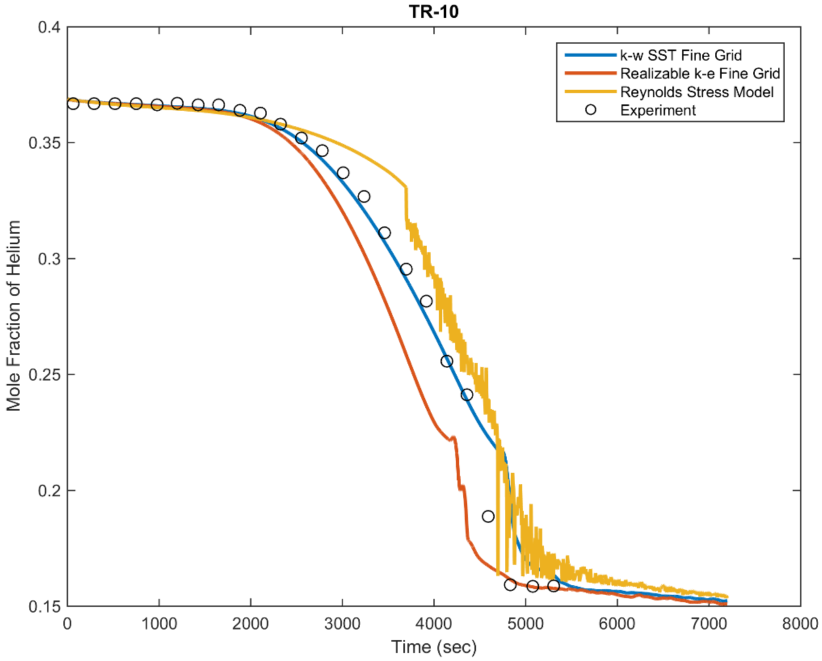

Figure 74: Mole fraction of helium vs. time (s) for RSM at TR-10

After 4000 seconds the simulation for RSM crashed and restarted several times. Even extra cost of the solving extra five transport equations for RSM to consider anisotropy, the general erosion prediction is not better than isotropic eddy viscosity based RANS models as shown in Figures 75-80.

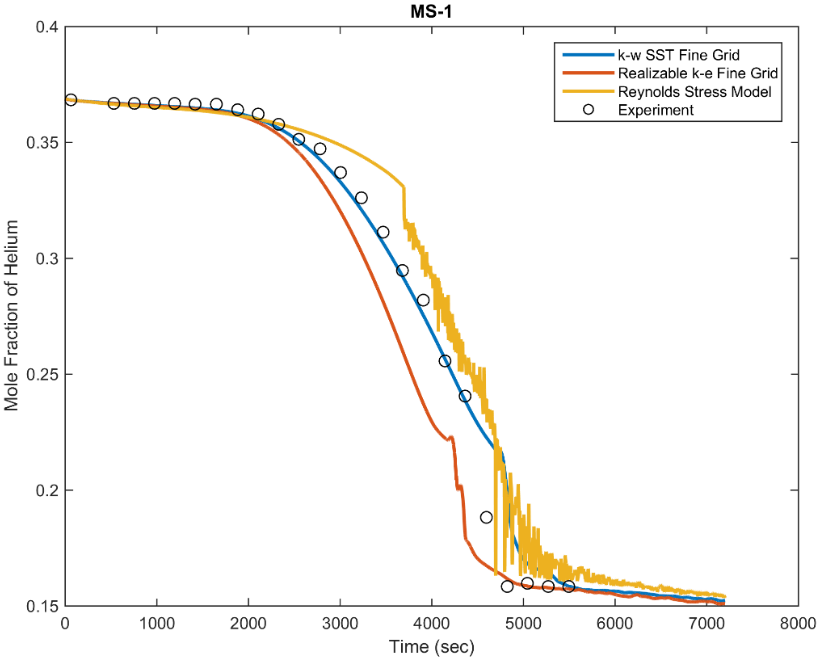

Figure 75: Mole fraction of helium vs. time (s) for RSM at MS-1

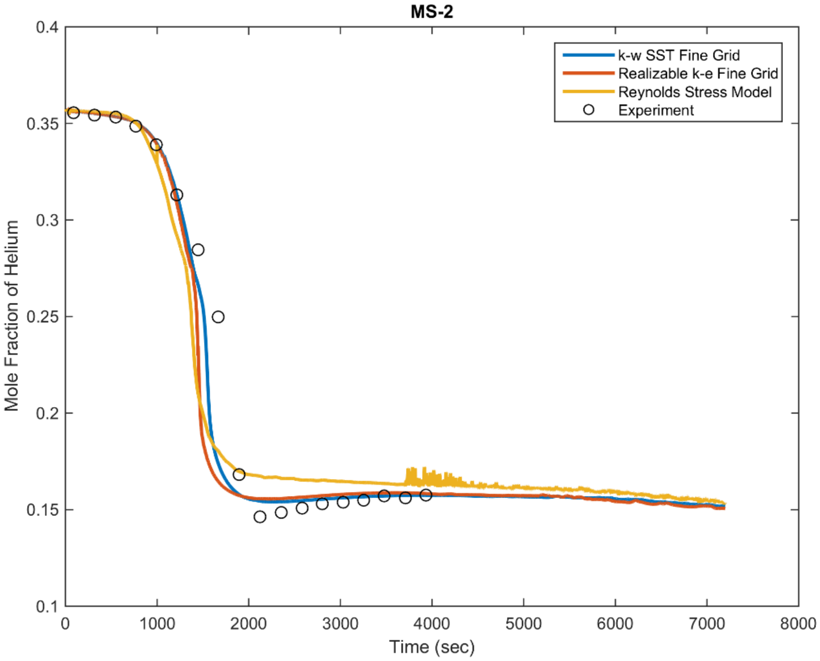

Figure 76: Mole fraction of helium vs. time (s) for RSM at MS-2

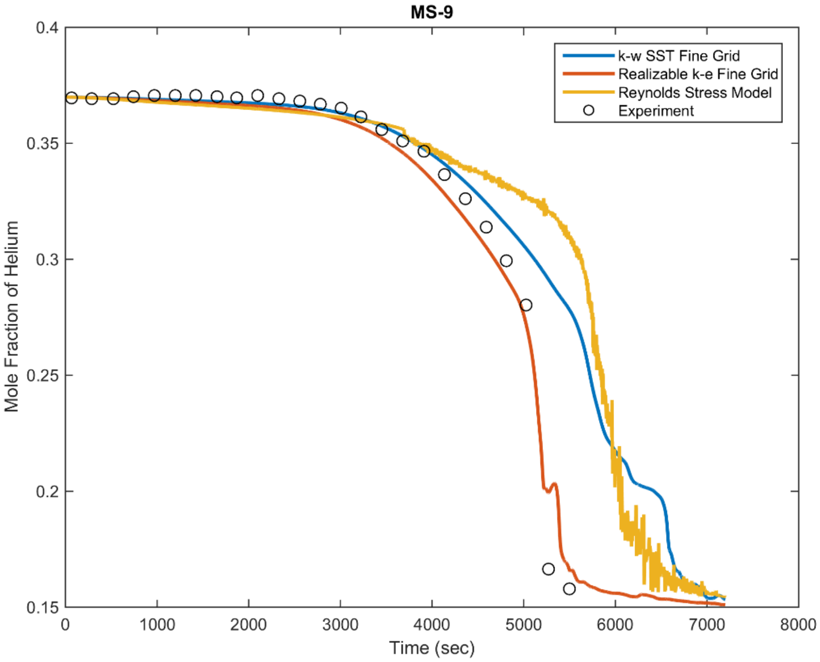

Figure 77**:** Mole fraction of helium vs. time (s) for RSM at MS-9

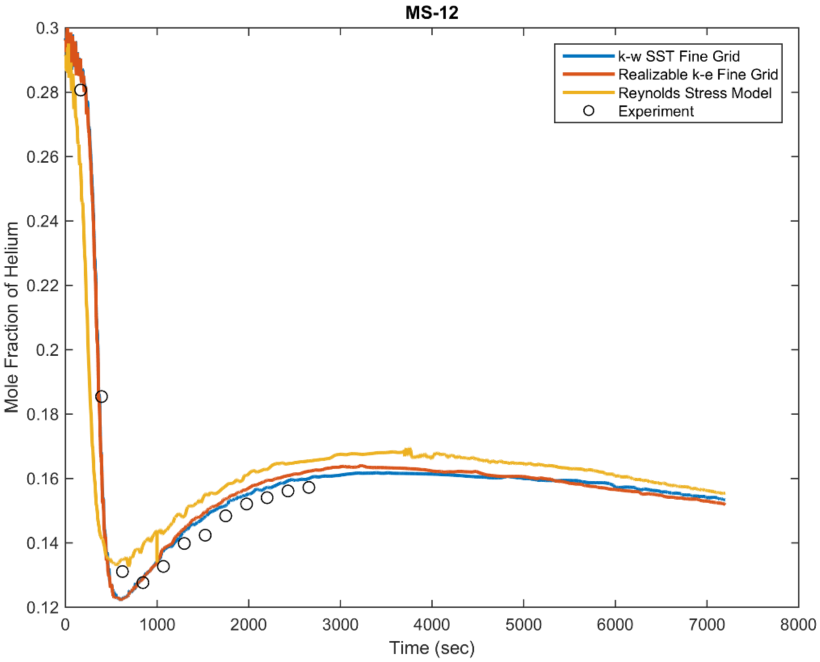

Figure 78: Mole fraction of helium vs. time (s) for RSM at MS-12

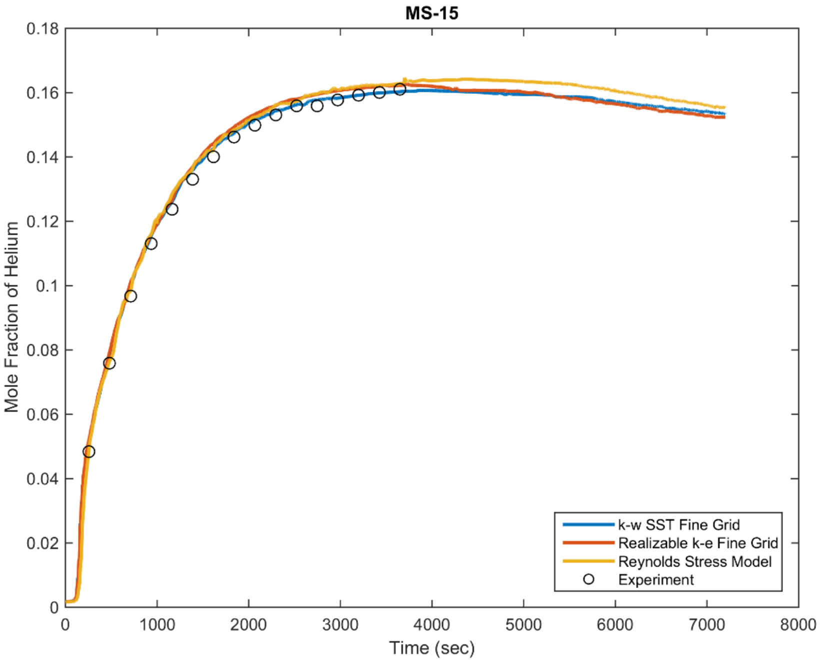

Figure 79: Mole fraction of helium vs. time (s) for RSM at MS-15

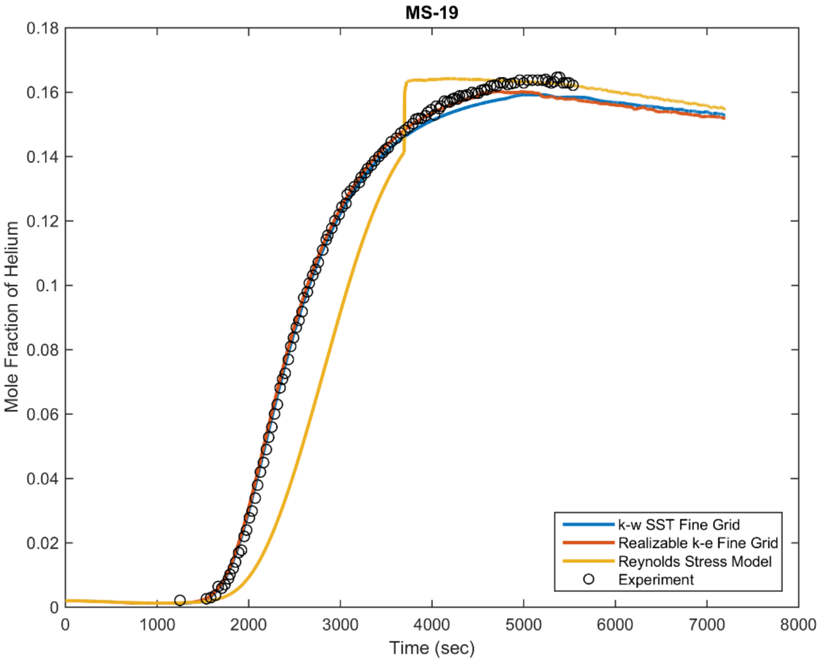

Figure 80: Mole fraction of helium vs. time (s) for RSM at MS-19

Overall, the RANS simulations showed good agreement with the experimental data for the erosion of the stratified layer and global mixing of the air-helium mixture, specifically, the modified k-ω SST showed good performance to predict the erosion process. The Realizable k-ϵ predicted better than k-ω SST only at the point MS-9. Above this point, the mixing is affected by the wall and the possible reason is the implementation of the all y^+ wall model. The uncertainty of the mole fraction measurement is 0.5%.

VI.3.2 Velocity and Turbulent Kinetic Energy Results

The velocity and turbulent kinetic energy data are averaged over a time period of 204.6 s. The solution time will refer to the time in the middle of this averaging period. Solution time for HVY-3, HVY-5, VVY-1 and TKE-2 are 1213, 1795, 111, 1213 seconds respectively. As shown in Figures 81-83, the time averaged axial velocities are slightly under-predicted for all RANS models except the RSM. The velocities are generally overestimated for the RSM model. On the other hand, the shape of the velocity profile for the RSM model is not matched with the experimental data while the shape of the other models matched with experimental data. The averaged axial velocity on the horizontal line (HVY-3) is in better agreement with the experimental data than HVY-5. The location of the HVY-5 is higher than HVY-3 and 582 seconds late. The potential reason of the underestimation of the averaged velocity may be related with underestimation of the approaching velocity of the incoming jet and overestimation of the turbulent viscosity. Because at this time the mixing process of the gas components are predicted with good agreement. This phenomena show that the components of the multi-species equation should be investigated due to less convection diffusion and more turbulent diffusion. In TKE-2 turbulent kinetic energy distribution shows high variation for different models as shown in Figure 84. It is overestimated by RSM and underestimated by the Realizable k-ϵ. The better prediction of turbulent kinetic energy for the SST k-ω resulted in also better prediction of the erosion of the stratified layer.

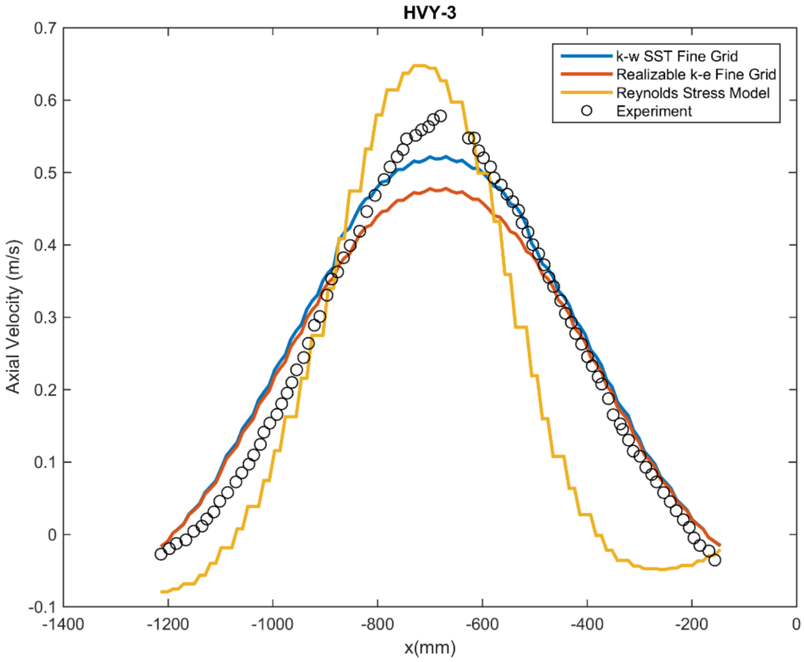

Figure 81: Averaged axial velocity profile for RSM at 1213 s.

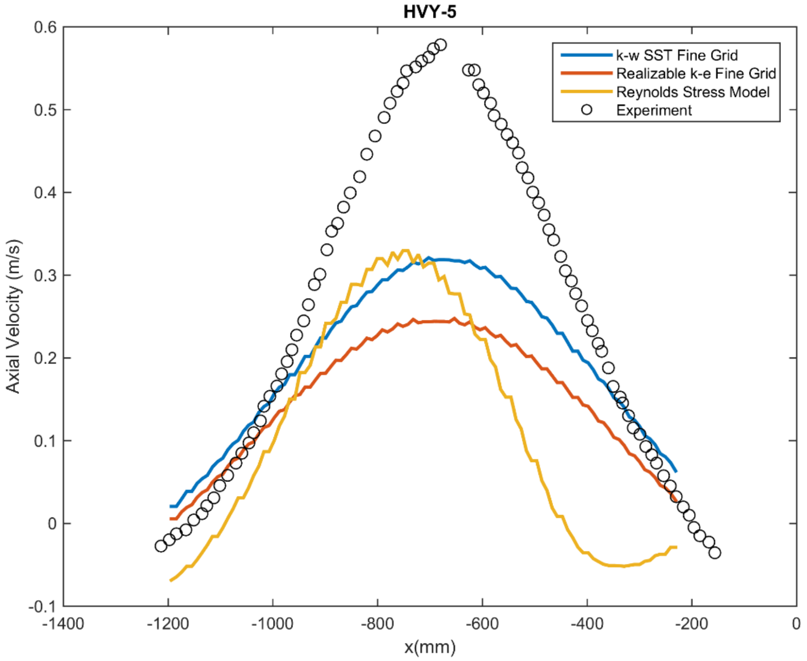

Figure 82: Averaged axial velocity profile for RSM at 1795 s.

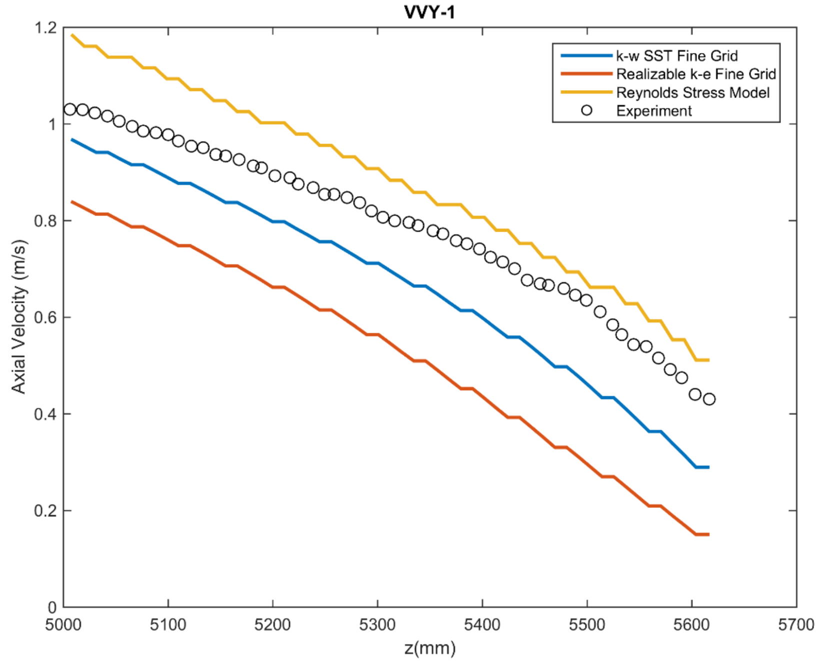

Figure 83: Averaged axial velocity profile for RSM at 111 s.

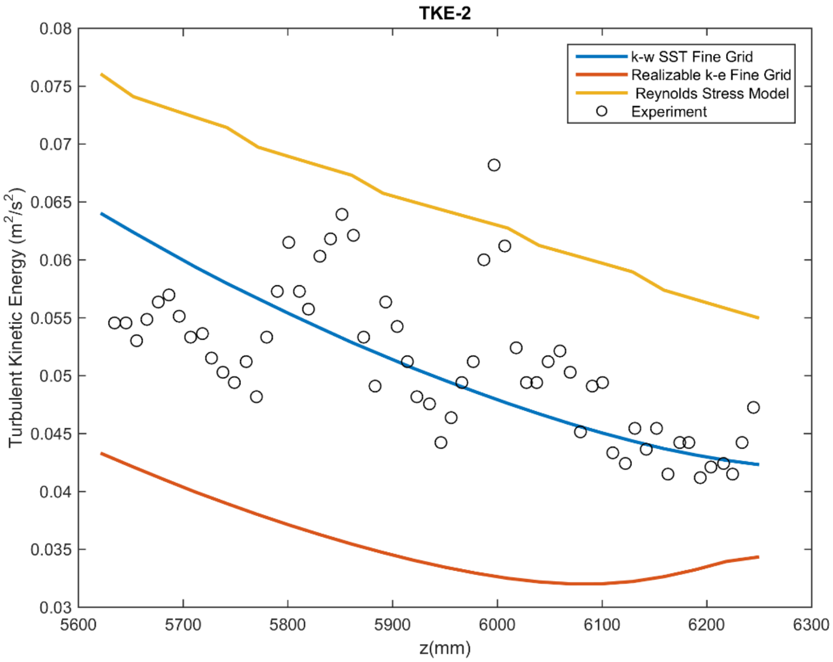

Figure 84: Averaged turbulent kinetic energy profile for RSM at 1213 s.

VI.3.3 Temperature Results

Even though the test specifications indicated that heat loss for actual experiment is too small, the temperatures for all turbulent models are overestimated as shown in Figure 85 and Figure 86. At the beginning of the experiment, the temperature was predicted with good agreement, after a thousand seconds, the temperature was over predicted due to neglected heat transfer from the vessel surface. Additionally, the temperature at point TC-5, which is located off-jet axis, shows excessive heating for RSM model.

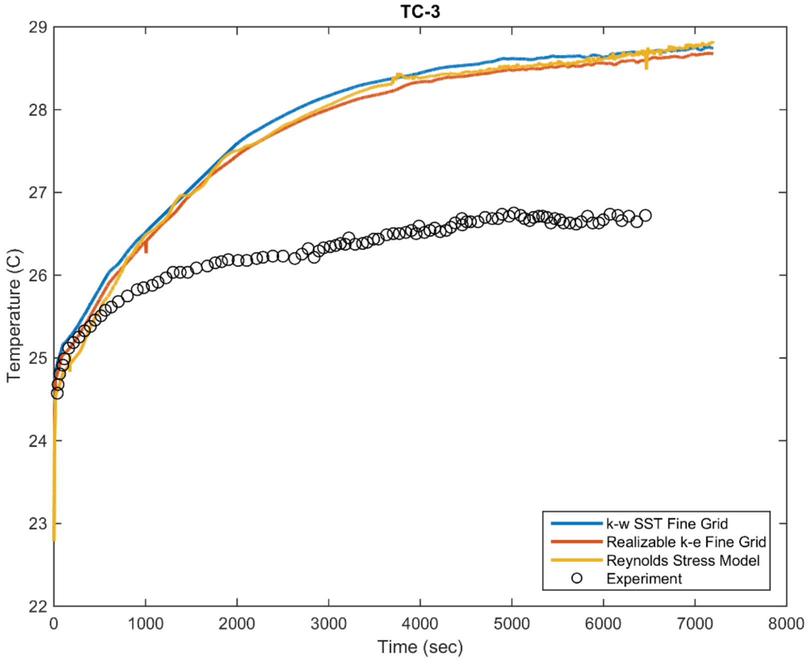

Figure 85: Temperature (^{0}C) vs. time (s) for RSM at point TC-3

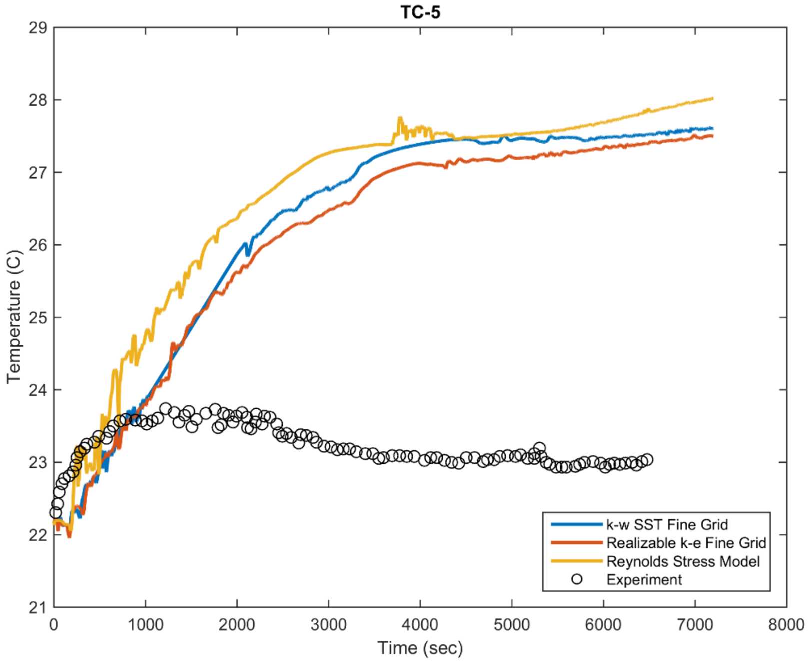

Figure 86: Temperature (^{0}C) vs. time (s) for RSM at point TC-5

VI.4 Large Eddy Simulation Results

In Figure 87-92 the comparison of the LES and k-ω SST simulation are shown for the mole fraction of helium at the stratified layer along the jet axis and time-averaged axial velocity on a horizontal (HVY-3) and vertical line(VVY-1) in Figure 93 and Figure 94, respectively. The Large Eddy simulation is normally expected to yield results that agree more closely with experimental data due to its higher fidelity. It is resolving larger scales while modeling smaller scales.

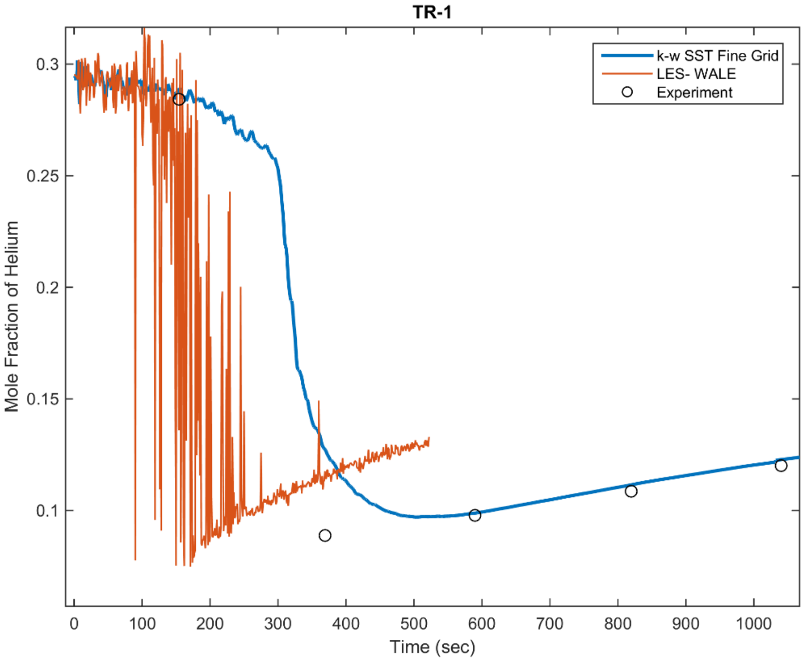

Figure 87**:** Mole fraction of helium vs. time (s) for LES at point TR-1

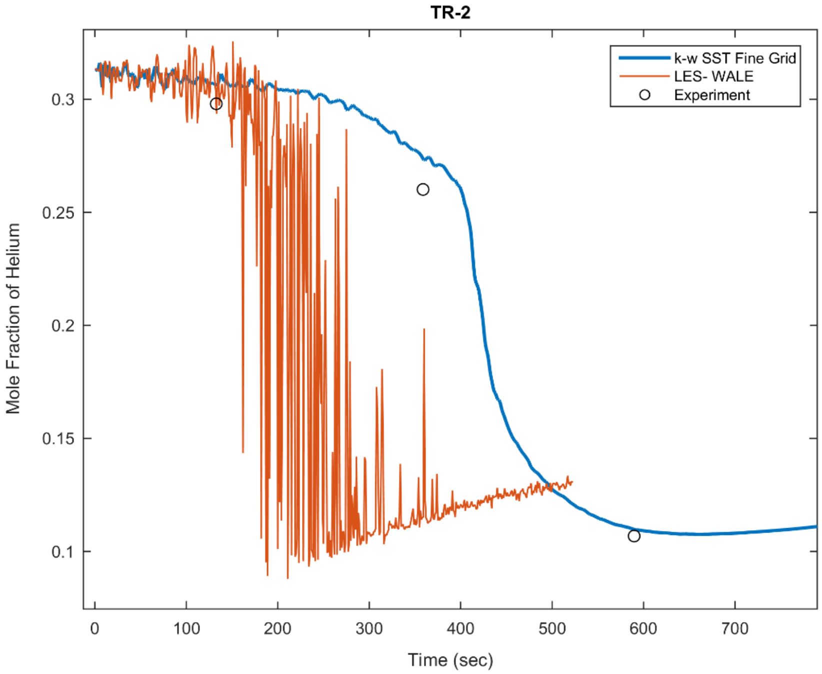

Figure 88: Mole fraction of helium vs. time (s) for LES at point TR-2

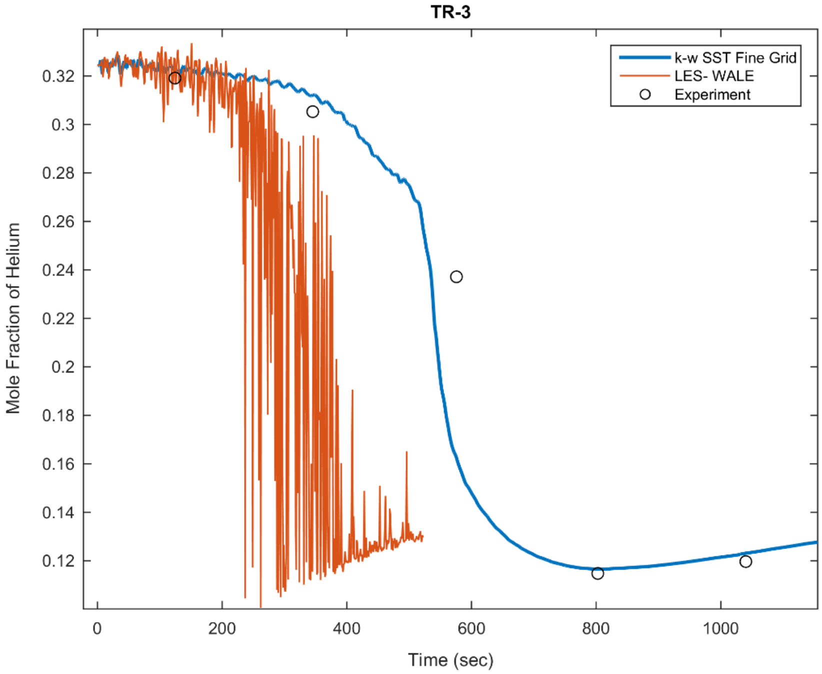

Figure 89: Mole fraction of helium vs. time (s) for LES at point TR-3

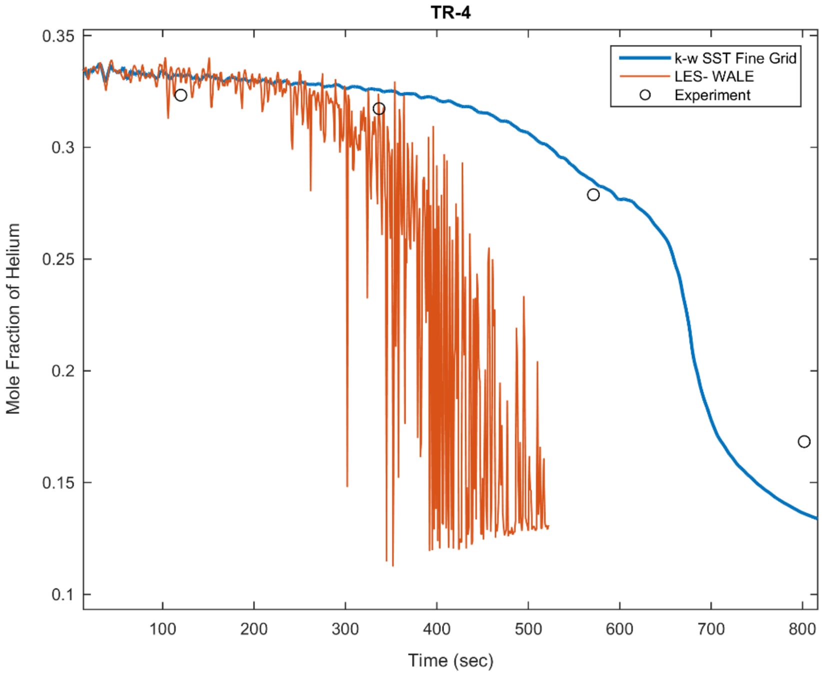

Figure 90: Mole fraction of helium vs. time (s) for LES at point TR-4

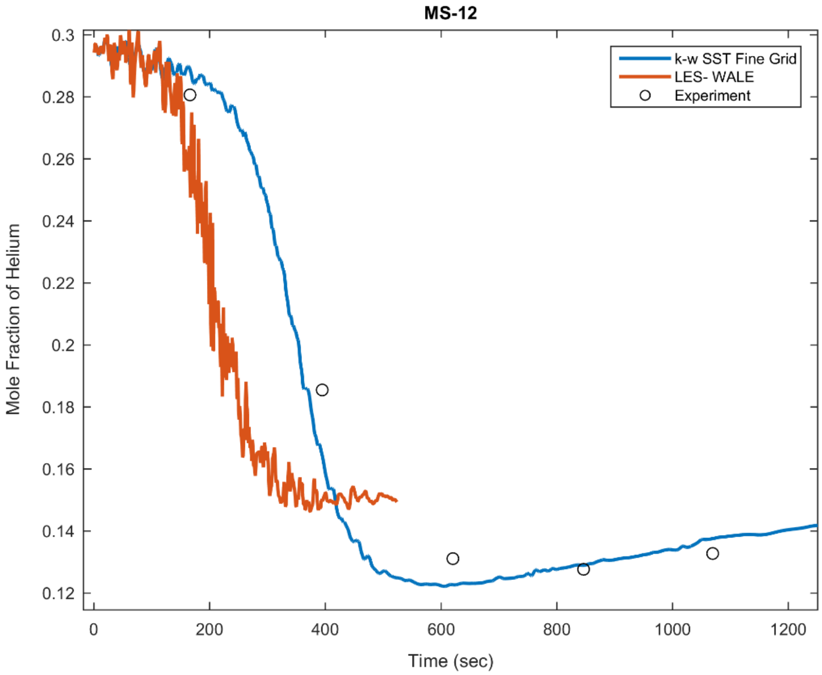

Figure 91: Mole fraction of helium vs. time (s) for LES at point MS-12

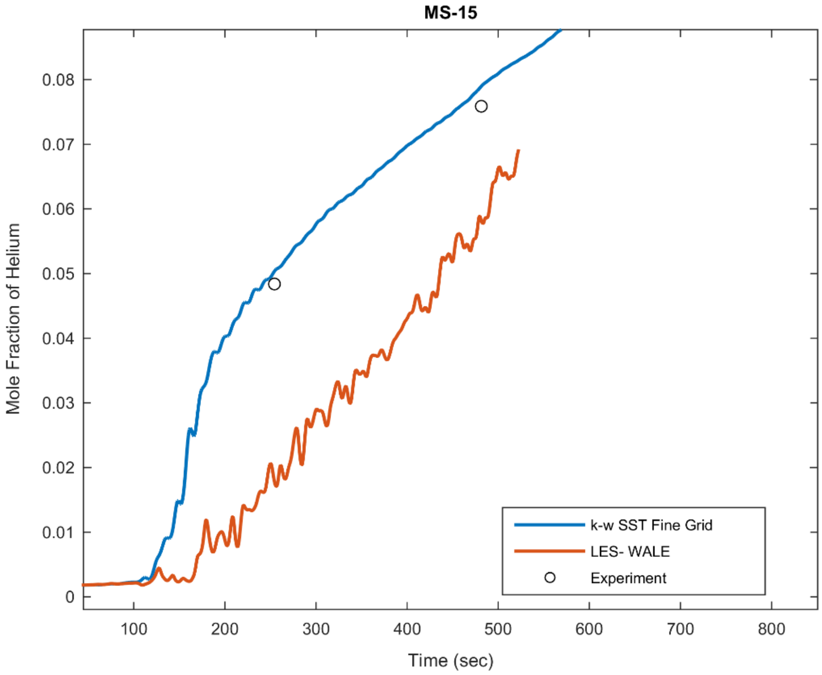

Figure 92: Mole fraction of helium vs. time (s) for LES at point MS-15

However, in the present study, the LES simulation resulted in faster erosion of the stratified layer. The reason of the faster erosion is because of the higher expansion velocity of the jet. The velocity of the jet in the centerline is higher than both experimental and numerical data from RANS simulations. Even a fully-developed boundary condition is applied at the inlet boundary, it is still overestimated. This problem could be overcome without modeling injection pipe but due to time restriction it is not simulated for present study. As a result of that, the rate of the erosion of the stratified layer is weakly depend on the average of the axial velocity at the exit of the injection pipe. But it is strongly depend on the jet centerline velocity at the exit. This is also confirmed with k-ω SST simulations during this study.

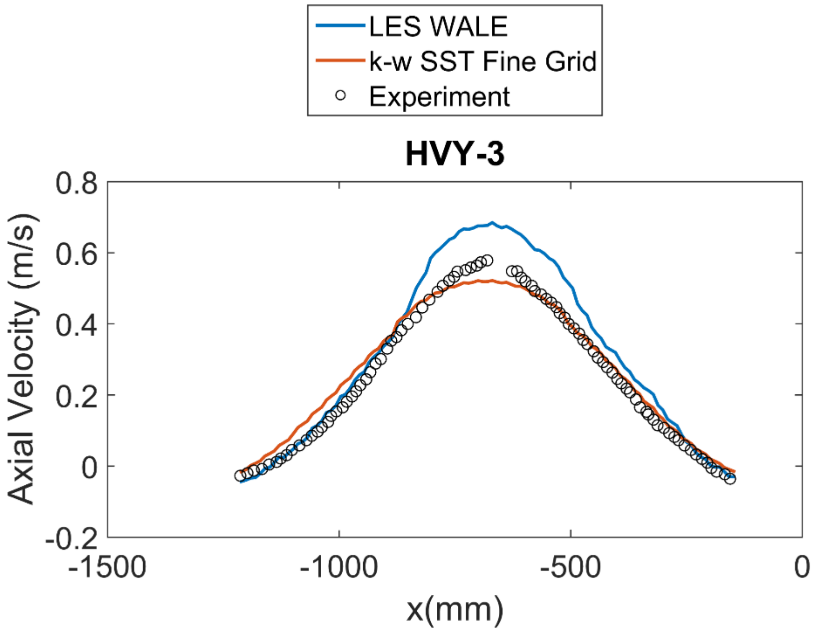

Figure 93: Averaged axial velocity profile for LES at 1213 s.

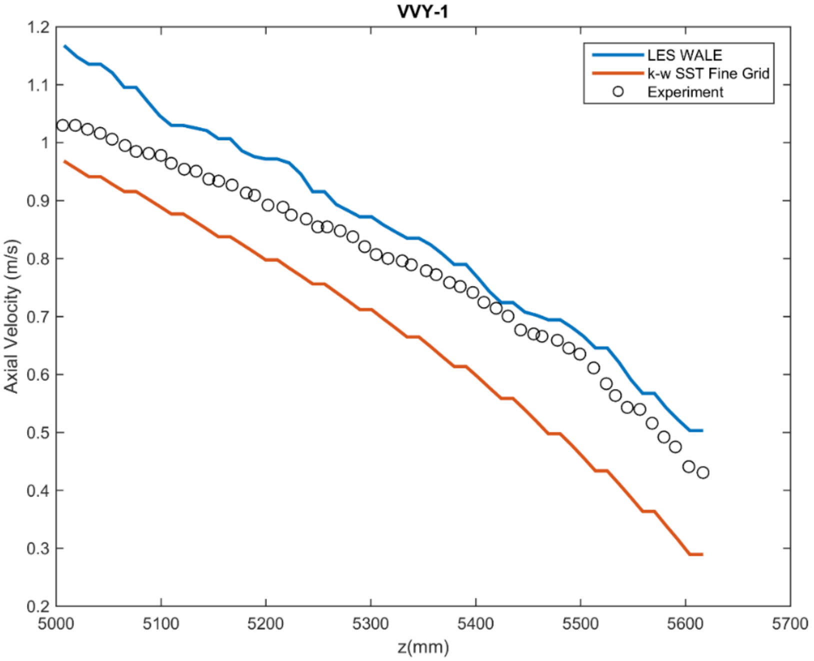

Figure 94: Averaged axial velocity profile for LES at 111 s.

As a result of the higher jet centerline velocity, higher averaged velocities are obtained and higher convection results in faster erosion and the mixing of the air-helium gas mixtures.

VI.5 Turbulent Schmidt Number Sensitivity Results

The turbulent Schmidt number is the dimensionless number that defines the ratio between the rates of turbulent transport of momentum and the turbulent transport of mass. It appears in the buoyancy term in the turbulent kinetic energy and in the species transport equation. When the flow is in the turbulent region, the mass transport is driven by the convective, molecular and turbulent diffusion. In the present study, the mass transport is dominated by the turbulent diffusion. Turbulent diffusion term in the species equation has the turbulent Schmidt number (ScT) in its denominator. This number is used as 0.9 as default for STAR-CCM+ 9.04 for all analysis in this thesis. However, the other well-known CFD codes are used the different variations of it such as 0.7. In this part of thesis, the turbulent Schmidt number sensitivity analysis is conducted. Due to the computational cost, only coarse mesh is used with $\mathrm{k}-\omega$ SST turbulence model.

The results show that the variation of the turbulent Schmidt number has strong effect at the beginning of the interaction of the jet with the layer. As show in Figure 95, Figure 96, Figure 97 and Figure 98, when the jet penetrates the layer about 1000 seconds, the turbulent kinetic energy is at highest level due to the scattering of the incoming jet. As a result of the higher turbulent kinetic energy, the turbulent diffusion is stronger at this time period. However, in the long term mixing, the effect is less significant. When the experimental data is considered with 1% uncertainty in the measurement of the mole concentration, one can conclude the use of 0.9 for turbulent Schmidt number results in higher accuracy.

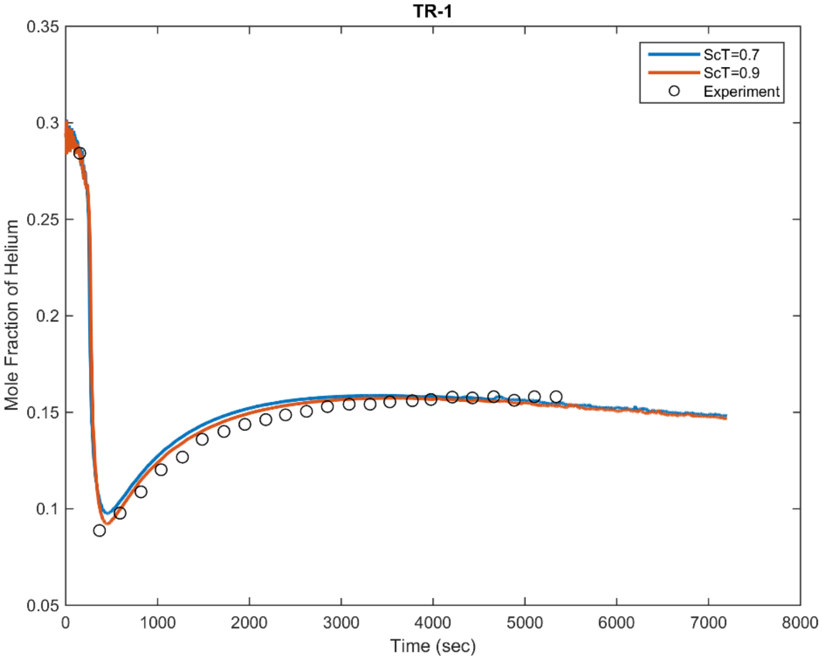

Figure 95: Mole fraction of helium vs. time at point TR-1 for ScT 0.7 and ScT 0.9

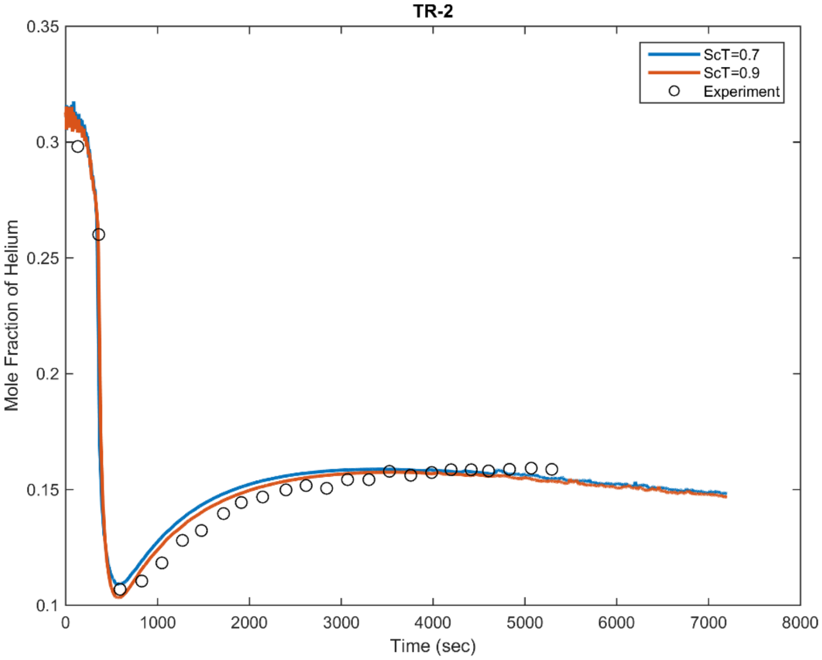

Figure 96: Mole fraction of helium vs. time at point TR-2 for ScT 0.7 and ScT 0.9

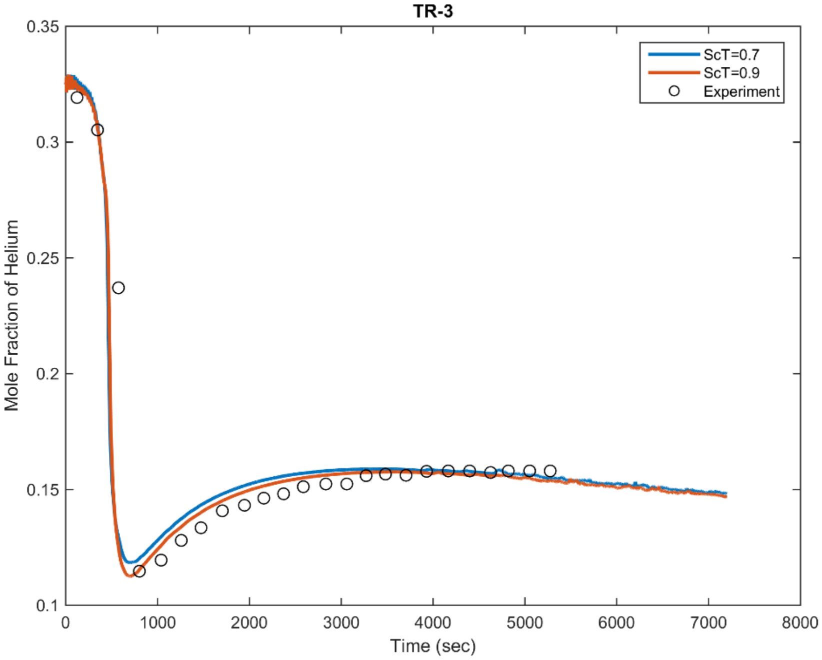

Figure 97**:** Mole fraction of helium vs. time at point TR-3 for ScT 0.7 and ScT 0.9

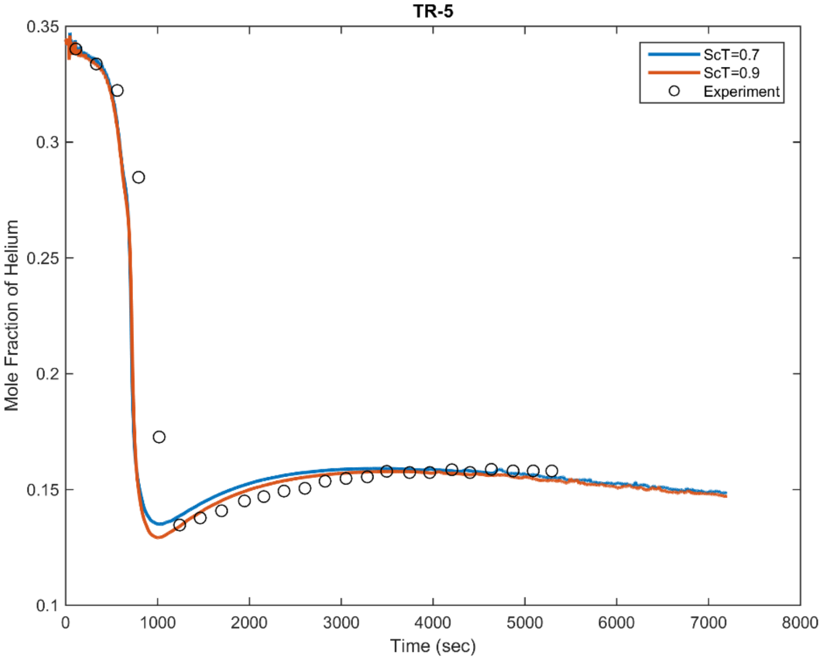

Figure 98: Mole fraction of helium vs. time at point TR-5 for ScT 0.7 and ScT 0.9

VI.6 Qualitative Analysis of Turbulent Models

As shown in Figure 99 and Figure 100, the mixing and erosion characteristic for all RANS models are similar to each other, while the LES results is not. The reason of this difference is based on the jet expansion velocity. Over prediction of the jet expansion velocity caused the faster erosion and of the stratified layer. One can also note that the higher jet centerline velocity decrease the reversed flow due to buoyancy force from the stratified layer. It is well known that LES is strongly sensitive to the inlet boundary condition. The overestimation of the expansion velocity should be investigated in more detail. One of the potential reason is the numerical diffusion due to flow from small pipe into the much greater flow domain.

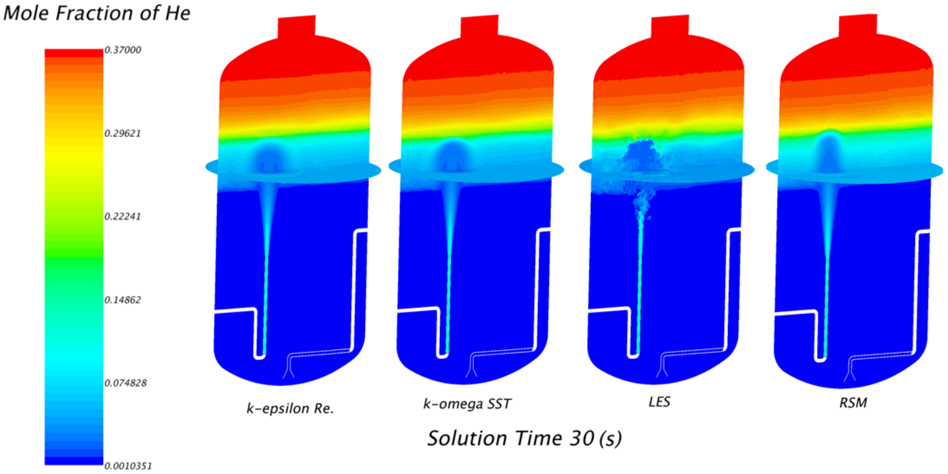

Figure 99: Qualitative comparison of the turbulent models at t=30 s.

One other interesting finding of the qualitative comparison is the narrow jet width for RSM as shown in Figure 99. This case is observed in averaged axial velocities along the horizontal line. Even the erosion rate predictions are similar to the other RANS models, the RSM model prediction for the shape of the injecting jet.

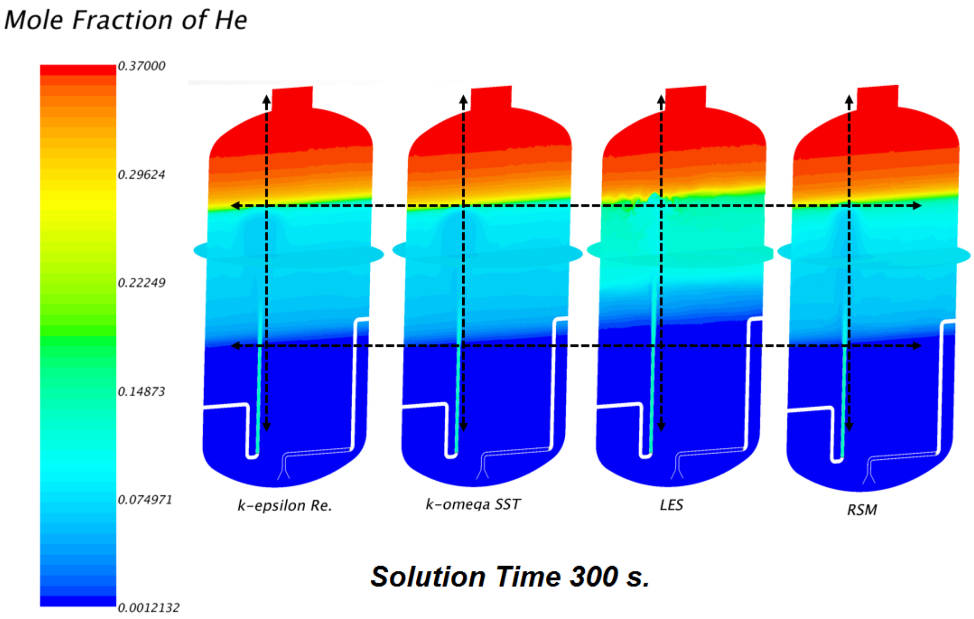

Figure 100: Qualitative comparison of the turbulent models at t=300 s.

Figure 100 also shows that the two-equation models showed similar erosion and mixing prediction with RSM even with their isotropic eddy-viscosity assumption. At the same time, the computational cost of the two equations models is less than RSM. However, the RSM models may perform better than two-equation model for stronger anisotropic flow. It needs further investigation.

CHAPTER VII

CONCLUSION

The LES simulation was conducted by using the fine grid, which was used also for the RANS simulations. The preliminary LES results indicated that the modeling of the injection pipe must be carried out carefully due to jet velocity at the exit of the injection pipe. The exit velocity was computed by LES simulation about 7.5% higher than $k - \omega$ SST simulation with the identical grid. The RANS simulations indicated the same problem for different turbulent models with smaller variations than LES model.

$k{-}\omega$ SST with the buoyancy term showed good agreement with experimental data for the erosion of the layer and global mixing, which are the main purpose of the validation. The grid refinement is very crucial in the interaction region of the jet and stratified layer. Realizable $k{-}\epsilon$ showed similar results with the $k{-}\omega$ SST for the erosion of the layer and global mixing. In general, the SST performed better due to advantage of the blending of the two different models.

The results of the RANS simulation showed that the centerline velocity of the jet at the exit of the pipe significantly affected the rate of erosion of the stratified layer. A 5% increase of the jet centerline velocity resulted in the erosion of the middle region of the stratified layer to be about 1000 seconds earlier. The PANDA test specification also contains the PIV data at the exit of the injection pipe. The boundary conditions were modified to match with the experimental PIV data. The difference of the jet expansion velocity may be caused by the different implementation of the near-wall treatments.

A sensitivity study was conducted to investigate the effect of the near wall modeling on the velocity. The velocity results at the outlet of the pipe were compared against the experimental data. The velocities at the outlet of the pipe were higher than experimental measurements for both turbulent models. Since the outlet velocity has great effect on the evolving of the erosion process, the injecting pipe modeling for the safety analyses must be carefully conducted.

$k-\omega$ SST model is used to investigate the effect of the variation of the turbulent Schmidt number. The results show that the variation of the turbulent Schmidt number has strong effect at the beginning of the interaction of the jet with the stratified layer and negligible effect in the long term mixing.

While, the RSM considered the anisotropic Reynolds Stresses, the isotropic eddy-viscosity based models showed better agreement with the experimental data and with less computational cost. Despite the very high computational cost of the LES, it resulted in earlier erosion of the stratified layer. The reason of earlier erosion is the over-estimation of the jet centerline velocity. Overall, $k-\omega$ SST showed good agreement with the experimental data except for temperature due to adiabatic assumption. The $k-\omega$ SST model can be used for full-containment safety analysis with a reasonable computational cost.

REFERENCES

Andreani, M., Badillo, A., Kapulla, R., 2014. Synthesis of results of the OECD-PSI blind benchmark exercise on erosion of a stratified layer by a buoyant jet in a large volume., OECD/NEA Workshop on CFD code Application to Nuclear Reactor Safety (CFD4NRS-5). ETHZ, Zurich, Switzerland.

Andreani, M., Haller, K., Heitsch, M., Hemstrom, B., Karppinen, I., Macek, J., Schmid, J., Paillere, H., Toth, I., 2008. A benchmark exercise on the use of CFD codes for containment issues using best practice guidelines: A computational challenge. Nuclear Engineering and Design 238, 502-513.

Andreani, M., Paladino, D., George, T., 2010. Simulation of basic gas mixing tests with condensation in the PANDA facility using the GOTHIC code. Nuclear Engineering and Design 240, 1528-1547.

Heitsch, M., Huhtanen, R., Techy, Z., Fry, C., Kostka, P., Niemi, J., Schramm, B., 2010. CFD evaluation of hydrogen risk mitigation measures in a VVER-440/213 containment. Nuclear Engineering and Design 240, 385-396.

Henrie, J.O., Postma, A.K., 1982. Analysis of the Three Mile Island (TMI-2) hydrogen burn, Second International Topical Meeting on Nuclear Reactor Thermal Hydraulics; Santa Barbara, CA (USA), p. 37.

Jirka, G.H., 2004. Integral model for turbulent buoyant jets in unbounded stratified flows. Part I: Single round jet. Environ Fluid Mech 4, 1-56.

Landahl, M., Mollo-Christensen, E., 1992. Turbulence and random processes in fluid mechanics, 2nd ed. Cambridge University Press, Cambridge ; New York.

Launder, B.E., Reece, G.J., Rodi, W., 1975. Progress in the Development of a Reynolds-Stress Turbulent Closure. J Fluid Mech 68, 537-566.

Liang, Z., Sonnenkalb, M., Bentaib, A., Sangiorgi, M., 2014. Status Report on Hydrogen Management and Related Computer Codes, France, p. 208.

Menter, F.R., 1994. Two-equation eddy-viscosity turbulence modeling for engineering applications. AIAA 32, 1598-1605.

Nicoud, F., Ducros, F., 1999. Subgrid-scale stress modelling based on the square of the velocity gradient tensor. Flow Turbul Combust 62, 183-200.

OECD-NEA, 2013. OECD-NEA-PSI CFD benchmark specification. National Environment Agency.

Rodi, W., 1991. Experience with Two-Layer Models Combining the k-e Model with a One-Equation Model Near the Wall, 29th Aerospace Sciences Meeting, Reno, NV, p. 41.

STAR-CCM+, 2014. STAR-CCM+ User Guide. version 9.04.

Studer, E., Brinster, J., Tkatschenko, I., Mignot, G., Paladino, D., Andreani, M., 2012. Interaction of a light gas stratified layer with an air jet coming from below: Large scale experiments and scaling issues. Nuclear Engineering and Design 253, 406-412.

Visser, D.C., Houkema, M., Siccama, N.B., Komen, E.M.J., 2012. Validation of a FLUENT CFD model for hydrogen distribution in a containment. Nuclear Engineering and Design 245, 161-171.

Wilcox, D.C., 1998. Turbulence Modeling for CFD, 2nd ed. DCW Industries, Inc.